Gernot Gruber, Dipl.-Ing. BSc

Performance and Reliability Limiting Point Defects in SiC Power Devices

DISSERTATION

zur Erlangung des akademischen Grades

Doktor der technischen Wissenschaften

eingereicht an der

Technischen Universität Graz

Betreuer

Peter Hadley, Univ.-Prof.

Institut für Festkörperphysik

Mitbetreuer: Markus Koch, Ass.Prof. Dipl.-Ing. Dr.techn.
Institut für Experimentalphysik

Graz, Dezember 2016

EIDESSTATTLICHE ERKLÄRUNG

Ich erkläre an Eides statt, dass ich die vorliegende Arbeit selbstständig verfasst, andere als die angegebenen Quellen/Hilfsmittel nicht benutzt, und die den benutzten Quellen wörtlich und inhaltlich entnommenen Stellen als solche kenntlich gemacht habe. Das in TUGRAZonline hochgeladene Textdokument ist mit der vorliegenden Dissertation identisch.

______________________ ________________________________

Datum Unterschrift

Abstract

Wide-bandgap semiconductors have a great potential for power electronics applications. One of the most technologically mature wide-bandgap semiconductors is silicon carbide (SiC) with various types of devices being commercially available. However, some SiC devices have so far not been able to reach their theoretically predicted potential and problems with their performance and reliability persist even in the best devices. In the case of SiC metal-oxide-semiconductor field effect transistors (MOSFETs) the channel mobility is at least one order of magnitude lower than the theoretical value. Furthermore, reliability issues like threshold voltage instabilities occur. Point defects in SiC devices play a key role in the degradation and underperformance of SiC MOSFETs and are in the current focus of research.

This thesis studies point defects in SiC devices by means of electrically detected magnetic resonance (EDMR). This method is based on electron paramagnetic resonance (EPR) and allows for the study of the structure of paramagnetic point defects that interact with conduction electrons in a semiconductor device. EDMR is a very sensitive technique and can be applied to fully manufactured devices and is thus applicable for the study of devices fabricated by state-of-the art processing. In this thesis defects in SiC *pn*-junctions and in SiC MOSFETs were extensively studied with EDMR and compared to theoretical defect models.

The dominant recombination center in N-implanted SiC *pn*-junctions was identified as the substitutional N coupled to a Si vacancy (N_CV_{Si}) defect. This defect may be an explanation for the saturation of the doping concentration at high N implantation doses. Furthermore, the dominant recombination center at the SiC-SiO_2 interface in various SiC MOSFETs was assigned to C dangling bond (P_{bC}) centers. While those defects are probably not causing the degradation of the channel mobility, their observed EDMR spectrum is well known and has often been reported in comparable studies. However, previous literature has made an assignment to the Si vacancy (V_{Si}) defect, which fails to explain the observed hyperfine (HF) features in the EDMR spectrum. It is one major achievement of this thesis to demonstrate that the P_{bC} defect is a more suitable model for this well-known EDMR spectrum.

In order to clarify predictions from different studies in the literature, some of which are contradicting each other, the SiC-SiO_2 interface was also studied with transmission electron spectroscopy (TEM) and electron energy loss spectroscopy (EELS). Two identically processed devices subsequently received different passivation treatments in oxygen gas (O_2) or nitric oxide (NO). The anneals resulted in dramatically different electrical parameters. The devices were extensively compared in terms of their interface structure by means of TEM and EELS. The only major difference found was an increased N content in the device that received an anneal in NO atmosphere, suggesting that passivation of point defects by N atoms is the key process for the enhancement of the device performance.

Kurzfassung

Halbleiter mit breitem Bandabstand besitzen ein großes Potential für Anwendungen in der Leistungselektronik. Eines der am ausgereiftesten Materialien ist Siliziumkarbid (SiC), welches in Form verschiedener Bauelemente am Markt erhältlich ist. Allerdings konnten manche SiC Bauelemente bisher noch nicht ihr theoretisch vorhergesagtes Potential ausschöpfen und auch bei den besten Bauelementen bestehen nach wie vor Probleme mit der Leistung und der Zuverlässigkeit. Bei SiC Metall-Oxid-Halbleiter-Feldeffekttransistoren (MOSFETs) liegt die Mobilität im Kanal zumindest eine Größenordnung unter dem theoretischen Wert. Zusätzlich treten Probleme mit der Zuverlässgkeit, wie zum Beispiel Instabilitäten der Schwellspannung, auf. Punktdefekte in SiC Bauelementen spielen eine Schlüsselrolle bei der Verschlechterung und verminderten Leistung von SiC MOSFETs und sind im Fokus der derzeitigen Forschung.

Diese Arbeit untersucht Punktdefekte in SiC Bauelementen mittels der elektrisch detektierten Magnetresonanz (EDMR). Diese Methode basiert auf der Elektronenspinresonanz (EPR) und ermöglicht die Untersuchung der Struktur paramagnetischer Punktdefekte welche in einem Halbleiterbauelement mit den Leitungselektronen wechselwirken. EDMR ist eine sehr empfindliche Methode, anwendbar auf voll prozessierten Bauelementen und kann für die Untersuchung solcher, mit Methoden am neuesten Stand der Technik gefertigten, herangezogen werden. Diese Arbeit behandelt umfangreiche EDMR Messungen und den Vergleich derer mit theoretischen Modellen von Punktdefekten in SiC *pn*-Übergängen und SiC MOSFETs.

Das dominante Rekombinationszentrum in N implantierten SiC *pn*-Übergängen wurde als der N_CV_{Si} Defekt, bestehend aus einem substitutionellen N-Atom gekoppelt an eine Si-Leerstelle, identifiziert. Dieser Defekt ist eine mögliche Erklärung für die Sättigung der Dotierkonzentration bei hohen N-Implantationsdosen. Im Weiteren wurde das dominante Rekombinationszentrum an der SiC-SiO_2 Grenzschicht in verschiedenen SiC MOSFETs offenen C-Bindungen an der Oberfläche (P_{bC} Defekte) zugeordnet. Während diese Defekte vermutlich nicht der Grund für die verschlechterte Mobilität sind, so ist ihr EDMR Spektrum wohl bekannt und oft in vergleichbaren Studien beobachtet worden. Jedoch wurde das EDMR Spektrum in der bisherigen Literatur der Si-Leerstelle (V_{Si}) zugeordnet, welche die beobachtete Hyperfeinstruktur unzureichend erklärt. Eines der Hauptergebnisse dieser Arbeit ist die Demonstration, dass der P_{bC} Defekt ein passenderes Modell für dieses wohlbekannte EDMR Spektrum ist.

Um teilweise widersprüchliche Vorhersagen aus früheren Studien in der Literatur abzuklären, wurde die SiC-SiO_2 Grenzschicht auch mittels Transmissionselektronenmikroskopie (TEM) und Elektronenenergieverlustspektroskopie (EELS) untersucht. Zwei ident prozessierte Bauelemente wurden in unterschiedlicher Atmosphäre passiviert: in Sauerstoffgas (O_2) bzw. Stickstoffmonoxid (NO). Der Temperprozess resultierte in stark unterschiedlichen elektrischen Eigenschaften. Die Struktur der Grenzschicht der beiden Bauelemente wurde mittels TEM und EELS ausführlich verglichen. Der einzige wesentliche Unterschied war eine erhöhte N-Konzentration in dem in NO getemperten Bauelement. Dies deutet darauf hin, dass der Hauptprozess für die verbesserte Leistung des Bauelements die Passivierung von Punktdefekten durch N-Atome ist.

Acknowledgments

Scientific research is rarely done alone. I was fortunate to have worked in a team that encouraged and supported me. In this acknowledgment, I would like to thank the people who helped me and describe their contributions. I do this because I do not want to give the impression that I claim the work of others as my own and because I am truly grateful for their assistance.

The initial idea for performing EDMR measurements on SiC devices came from Michael Nelhiebel of KAI GmbH and Thomas Aichinger of Infineon Technologies Austria. Thomas was doing a postdoc at the Pennsylvania State University where he performed EDMR measurements and Michael is an expert on all kinds of materials characterization methods. They determined that there was equipment for EPR experiments at the Institute of Experimental Physics at the Graz University of Technology (TU Graz) and this equipment could probably be modified for EDMR measurements. They discussed this idea with the director of KAI GmbH Josef Fugger who agreed to fund the project. At the TU Graz, Peter Hadley and Markus Koch became involved. Peter is the head of the Institute of Solid State Physics and studies semiconductor devices. Markus is an assistant professor in the Institute of Experimental Physics and taught the EPR laboratory course. In 2011, I was offered a master's position to modify the EPR setup in order to perform EDMR measurements at the TU Graz and to reproduce the results of Thomas. From KAI GmbH I was supervised by Michael and Gregor Pobegen who was at that time doing a PhD focusing on electrical characterization of MOSFETs. At the TU Graz I was supervised by Peter and Markus. At this point I also want to acknowledge Wolfgang E. Ernst and Günther Grampp who enabled this project by providing equipment and expertise, as well as Werner Luttenberger from the workshop of the Institute of Experimental Physics for building customized parts of the experimental setup. As described in my master's thesis [1], the project succeeded in reproducing the results of Thomas.

Following the master's project I was offered a PhD position in order to continue the EDMR measurements on SiC devices under the supervision of Thomas who by that time finished his postdoc and has started in the SiC MOSFET technology development department of Infineon Technologies Austria. Further, I was supervised by Peter and Markus. During the project Gregor completed his PhD and started setting up a device characterization lab at KAI GmbH. It this time he became my main supervisor instead of Thomas. My PhD project aimed to conduct EDMR experiments on state-of-the art SiC devices and to expand the current understanding of the point defects observed in the experiments.

The PhD project resulted in several publications and ongoing research projects. In the following I want to give an overview of the main publications related to this thesis and the respective contributions of the individual authors.

The first paper that I wrote during my PhD was:

G. Gruber, P. Hadley, M. Koch, D. Peters, and T. Aichinger, "**Interface defects in SiC power MOSFETs - An electrically detected magnetic resonance study based on spin dependent recombination.**" In: AIP Conference Proceedings 1583 (2014), p. 165 [2].

The concept for this paper originated from Thomas who suggested that it would be interesting to investigate SiC MOSFETs with EDMR. The MOSFETs were designed and manufactured by Dethard Peters. I conducted the experiments and had regular meetings to discuss the results with Thomas and Gregor who also gave me guidance in performing and improving the measurements. I had separate meetings to discuss the results with Peter. Markus assisted with the ongoing improvement of the measurement setup and in developing a measurement routine. I wrote the initial draft of the manuscript and Peter suggested revisions. When the two of us were satisfied with the manuscript, we sent it to the other authors for proofreading. I also presented this study in a poster presentation at the International Conference of Defects in Semiconductors 2013 in Bologna, Italy. The results are partly discussed in chapter 7.

The second paper that resulted from this project was:

G. Gruber, P. Hadley, M. Koch, and T. Aichinger "**Electrically detected magnetic resonance study of defects created by hot carrier stress at the SiC/SiO_2 interface of a SiC *n*-channel metal-oxide-semiconductor field-effect transistor.**" In: *Applied Physics Letters* 105 (2014), p. 043506 [3].

The concept for this paper originated from Thomas and me following a study published by Gregor who demonstrated strong degradation effects in SiC devices subject to hot carrier stress [4]. The samples studied in this paper were designed and manufactured by Thomas. I conducted the stressing of the devices, the electrical characterization, and the EDMR measurements. Further upgrades of the measurement setup for higher magnetic field modulation and wider magnetic field scans and a higher precision of the magnetic field measurement were performed with the help of Markus. The results were interpreted with the help of Thomas and Peter. The manuscript draft was written by me and edited by Thomas and Peter and ultimately proofread by Markus. This study is the main subject of chapter 8.

The third paper I wrote was:

G. Gruber, T. Aichinger, G. Pobegen, D. Peters, M. Koch, and P. Hadley "**Influence of oxide processing on the defects at the SiC-SiO_2 interface measured by electrically detected magnetic resonance.**" In: *Materials Science Forum* 858 (2016), p. 643 [5].

The concept of this paper initiated from Thomas and was one of the central topics of this thesis. This paper contained a series of measurements on devices designed and manufactured by Thomas and Dethard. The electrical measurements were performed partly by me and partly by Gregor. I also performed the EDMR measurements. Markus helped me with upgrading the experimental setup with a new microwave source and the accompanying adaptions of the measurement routines. I discussed the measured data regularly with Thomas and Gregor, as well as Peter. The manuscript was written by me and edited by Gregor and Peter. Final proofreading was performed by Thomas and Markus. I also presented this study in a poster presentation at the International Conference on Silicon Carbide and Related Materials 2015 in Giardini-Naxos, Italy. The results are part of chapter 7.

Since the interpretation of the observed defects was always a challenging task, Michael and Thomas came up with the idea of a cooperation with the group of Alex Shluger at the University College London (UCL London) who is an expert on theoretical calculations on defects in semiconductors. In 2013 Jon Cottom started a PhD thesis on density functional theory (DFT) simulations on SiC under the supervision of Alex. The aim of this project was to simulate defect models of candidate defects suggested from the EDMR experiments and comparing calculated structural parameters with the experimental data. The cooperation resulted in the joint publication:

J. Cottom, G. Gruber, P. Hadley, M. Koch, G. Pobegen, T. Aichinger, and A. Shluger "**Recombination centers in 4H-SiC investigated by electrically detected magnetic resonance and *ab initio* modeling.**" In: *Journal of Applied Physics* 119 (2016), p. 181507 [6].

The concept of this paper originated from Thomas and his work performed on N-implanted SiC *pn*-junctions [7]. Until this paper the observed EDMR spectrum was tentatively assigned to N complexes without a clear understanding of the structure of those complexes. The experimental curves were recorded by me and basically reproduced the results of Thomas mentioned above. Jon conducted extensive theoretical simulations of candidate defects under the guidance of Alex, narrowing down the possible candidates to only a few. In order to enable an accurate comparison between the theoretical and the experimental data I developed a tool that generates simulated defect spectra from the calculated structural parameters with the help of Peter and Markus. The possibility for an accurate comparison and the discussion between Jon, Thomas, Gregor, Alex, and me led to further more detailed simulations by Jon, which resulted in a very good match between theory and experiment. The experimental parts of the paper and the part describing the program that compares the experimental data with the theoretical data was written by me. The introduction, discussion and conclusion sections were co-written by me and Jon. All remaining parts were written by Jon. The paper was edited and proofread by all remaining authors. The paper is discussed in chapter 6.

During the time of my PhD Michael suggested to perform TEM measurements on the studied SiC-SiO_2 at the Austrian Centre for Electron Microscopy and Nanoanalysis (FELMI-ZFE) in Graz. I was chosen to assist in carrying out the measurements since I was located very close to this institution and the topic was related to my PhD thesis. Werner Grogger who is the head of the TEM group at FELMI-ZFE and Evelin Fisslthaler as well as Gregor and Thomas took part in defining the tasks to be investigated. Martina Dienstleder prepared the studied samples and Christian Gspan performed the TEM investigations with my attendance. The TEM investigations became part of a research project with the Austrian Research Promotion Agency (FFG, Project No. 850220) which is still ongoing. The experiments conducted during my involvement in the project are discussed in chapter 9.

In addition to the people mentioned above, I thank my parents for their never ending support and generosity throughout my life and especially during my university years. Without them this work would not have been possible.

Moreover, I want to thank all my fellow students and colleagues at the TU Graz, KAI GmbH, and Infineon Technologies for fruitful discussions and their assistance in various measurements. I am especially thankful to Martin Faccinelli, Stefan Kirnstötter, Gerald Rescher, Alberto Salinaro, Robert Meszaros, and Julia Hassler.

Last, I want to thank all my friends and family members for their moral support and reminding me that there are many other important things in life than those taking place in a science lab.

This work was jointly funded by the Austrian Research Promotion Agency (FFG, Project No. 846579) and the Carinthian Economic Promotion Agency Fund (KWF, contract KWF-1521/26876/38867). The TEM measurements were funded by the Austrian Research Promotion Agency (FFG, Project No. 850220).

Contents

Abstract vi

Kurzfassung viii

Acknowledgments xiii

I Fundamentals 1

1 Silicon carbide (SiC) 3
- 1.1 Crystal structure . . . 3
- 1.2 Physical properties . . . 5
- 1.3 Bulk growth . . . 6
- 1.4 Homoepitaxy . . . 7
- 1.5 Doping . . . 9
  - 1.5.1 n-type doping . . . 10
  - 1.5.2 p-type doping . . . 10
- 1.6 The SiC-SiO_2 interface . . . 10
  - 1.6.1 MOSFETs . . . 11
  - 1.6.2 Oxidation . . . 13
  - 1.6.3 Characterization of the D_{it} at the SiC-SiO_2 interface . . . 14
  - 1.6.4 Interface structure . . . 16
  - 1.6.5 Post-oxidation annealing . . . 17
- 1.7 Point defects in SiC . . . 18
  - 1.7.1 Intrinsic bulk defects . . . 18
  - 1.7.2 Nitrogen related bulk defects . . . 20
  - 1.7.3 Interface Defects . . . 21
- 1.8 Summary . . . 22

2 Electrically detected magnetic resonance (EDMR) 23
- 2.1 Spins in a magnetic field . . . 23
  - 2.1.1 Electron Zeeman interaction . . . 24
  - 2.1.2 Hyperfine (HF) interaction . . . 25
  - 2.1.3 Electron-electron interaction . . . 25
- 2.2 Electron paramagnetic resonance (EPR) . . . 26
- 2.3 Spin dependent recombination (SDR) . . . 28

II Methodology **31**

3 Electrical characterization **33**
3.1 Transfer characteristics . . . 33
3.2 Charge pumping . . . 34

4 EDMR **35**
4.1 Experimental setup . . . 35
4.2 Description of an EDMR measurement . . . 37
4.3 The gated diode SDR technique . . . 37
4.4 The bipolar amplification effect (BAE) technique . . . 38
4.5 Determining the principal *g*-factors . . . 39
4.6 Simulations of EDMR spectra . . . 39
4.6.1 What makes up a HF spectrum? . . . 39
4.6.2 Generating simulated spectra . . . 41

5 Transmission electron microscopy (TEM) **43**
5.1 Instrumentation . . . 44
5.1.1 Bright field (BF) . . . 44
5.1.2 Annular dark field (ADF) . . . 44
5.1.3 High-angle annular dark field (HAADF) . . . 44
5.1.4 Electron energy loss spectroscopy (EELS) . . . 45
5.2 Determining the interface thickness . . . 46

III Results **49**

6 Identification of the $N_C V_{Si}$ center in N-implanted 4H-SiC *pn*-junctions **51**
6.1 Defects in SiC caused by N implantation . . . 52
6.2 Experimental results . . . 53
6.3 Theoretical modeling . . . 54
6.4 Comparison between experiment and theory . . . 56
6.5 Summary . . . 59

7 Defects at the SiC-SiO_2 interface of 4H-SiC MOSFETs and the influence of oxide processing **61**
7.1 Sample description . . . 62
7.2 Electrical characterization . . . 62
7.3 EDMR results . . . 64
7.3.1 Relative signals . . . 64
7.3.2 Angular dependence of the *g*-factor . . . 65
7.3.3 HF structure . . . 66
7.4 Investigation and simulation of the dominant defect . . . 68
7.5 Investigation of the 57 G doublet present in the N_2O-annealed devices . . . 73
7.5.1 Dependence on the microwave power . . . 73
7.5.2 Dependence on the gate voltage . . . 74
7.5.3 Dependence on the temperature . . . 75
7.5.4 Simulations . . . 76
7.5.5 Tilt series . . . 77
7.5.6 Discussion . . . 79

7.6 Summary 80

8 Defects at the SiC-SiO_2 interface of NO-annealed 4H-SiC MOSFETs and the influence of hot carrier stress 81

8.1 Hot carrier stress (HCS) 82
8.2 Experimental details 83
8.3 Results 83
8.4 Discussion 85
8.5 Summary 88

9 TEM investigations of the 4H-SiC-SiO_2 interface 89

9.1 Experimental details 90
9.2 Interface morphology 91
9.3 EELS characterization of the interface 93
9.4 Discussion 96
9.5 Summary 98

10 Conclusions and outlook 99

A Calculated hyperfine parameters for different N-containing defects in 4H-SiC 101

B A program for generating EDMR spectra from calculated HF data 103

C Problems with determining the SiC-SiO_2 interface thickness from the Si-$L_{2,3}$ EELS edge 109

D Temperature dependent resistance of a poly-heater 111

References 113

List of Figures 129

List of Tables 133

Acronyms 135

Symbols 139

Equipment 143

Part I

Fundamentals

Chapter 1

Silicon carbide (SiC)

Silicon carbide (SiC) is a wide-bandgap semiconductor material that was discovered almost 200 years ago. It has faced many challenges in terms of manufacturing until today. SiC has superior material properties for certain applications than more conventional materials like Si or gallium arsenide (GaAs). The small intrinsic carrier concentration due to the wide bandgap (e.g. 3.3 eV in 4H-SiC) paired with the high thermal conductivity makes it suitable for high temperature applications. The high breakdown field allows for blocking voltages exceeding 1200 V with low on-resistance, which makes SiC an ideal material for power devices. The large bulk mobility allows for high switching speeds and therefore high frequency applications. Additionally, SiC can withstand harsh environments, as it has a high thermal stability, chemical inertness and radiation resistance.

High quality bulk crystal growth was first introduced by J.A. Lely in 1955 [8]. Seeded sublimation growth which paved the way for production of SiC wafers was achieved in 1978 by Y.M. Tairov and V.F. Tsvetkov [9]. High-quality heteroepitaxy growth was first demonstrated on off-axis samples by N. Kuroda et al. in 1987 [10]. Further major improvements of processing (e.g. D. Nakamura et al. [11]) helped in dramatically improving SiC manufacturing in terms of quality, wafer size, and productivity. Despite these improvements SiC is still lacking behind Si technology [12, 13]. However, while SiC devices have not yet reached their full potential, many different types of devices have been realized and are commercially available [14, 15, 16]. In the following the current status of SiC technology development is reviewed with a focus on metal-oxide-semiconductor field effect transistors (MOSFETs) and electrically active point defects.

1.1 Crystal structure

SiC is composed of two atoms species, Si and C. Both elements are present in equal concentrations with generally every Si atom being strongly covalently bonded to four C nearest neighbors and vice versa. However, SiC can exist in many different crystal structures, all with different electrical properties. More than 250 of these so-called polymorphs are known [17]. The majority of these, are closely related and only differ from each other with respect to the stacking of hexagonal planes along the crystalline *c*-axis, i.e. the [0001] direction. Note that for further discussion all crystalline directions and planes are described using the Bravais-Miller indices [hkil] for directions and (hkil) for planes [18]. More than 170 of these so-called polytypes have been identified [19]. They are in principle composed of Si-C bilayers with a close-packed

hexagonal structure. There are generally three positions, A, B, and C, for a layer to be placed in a hexagonal close-packed stack of layers, as shown in Figure 1.1. The next layer is always in a different position than the one below. The sequence of these positions in the stacking and its periodicity defines each polytype. The most simple ones are shown in Figure 1.2. The most simple structure is the 2H polytype which is composed of bilayers stacked in an AB sequence. All atoms are located in hexagonal (h) sites and the structure is commonly known as wurtzite. Another very simple polytype is 3C which is only composed of cubic (k) sites and a stacking sequence of ABC. This structure is also known as zincblende. 4H (ABCB) and 6H (ABCACB) are composed of both quasi-cubic and quasi-hexagonal sites and are the polytypes with currently the most applications in commercial devices. Table 1.1 summarizes some of the main differences of the mentioned crystal structures. This table only compares crystallographic parameters, the bandgap energy, and the carrier mobilities at room temperature in order to demonstrate how different the electrical properties of these polytypes are. Note that for 2H-SiC no experimental data for the mobilities exist, while theoretical simulations suggest comparable or even higher mobilities than for the other polytypes shown [20, 21]. Figure 1.3 compares the band structure of different polytpyes. A more detailed comparison and discussion about polytypes can be found in the references [22, 23]. For this thesis only 4H-SiC was examined which is why all further discussions focus on this polytype. It is also the polytype which is most suitable for fabrication of high power, high frequency and high-temperature devices [24]. Consequently, material and device processing is most mature for this polytype, as it has received a lot of attention from the industry.

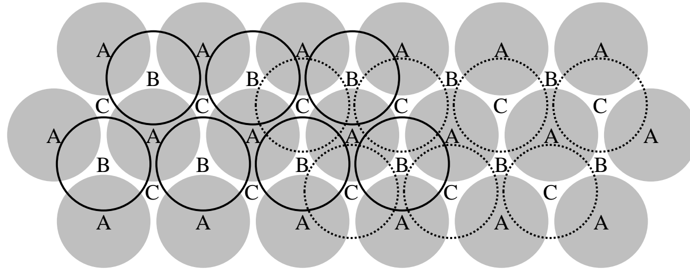

Figure 1.1: A close-packed hexagonal bilayer in position A (gray circles) viewed from the [0001] direction. The next bilayer can be placed on position B (solid circles) or C (dotted circles).

Table 1.1: Properties of the most simple SiC polytypes [22, 23].

Property	2H-SiC	4H-SiC	6H-SiC	3C-SiC
Stacking sequence	AB	ABCB	ABCACB	ABC
Lattice constant c (Å)	5.05	10.08	15.12	n.a.
Lattice constant a (Å)	3.08	3.08	3.08	4.36
Symmetry	C_{6v}	C_{6v}	C_{6v}	T_d
Bandgap energy (eV)	3.33	3.26	3.02	2.39
Electron mobility $\perp c$ ($cm^2V^{-1}s^{-1}$)	-	1020	450	1000
Electron mobility $\parallel c$ ($cm^2V^{-1}s^{-1}$)	-	1200	100	1000
Hole mobility ($cm^2V^{-1}s^{-1}$)	-	120	100	100

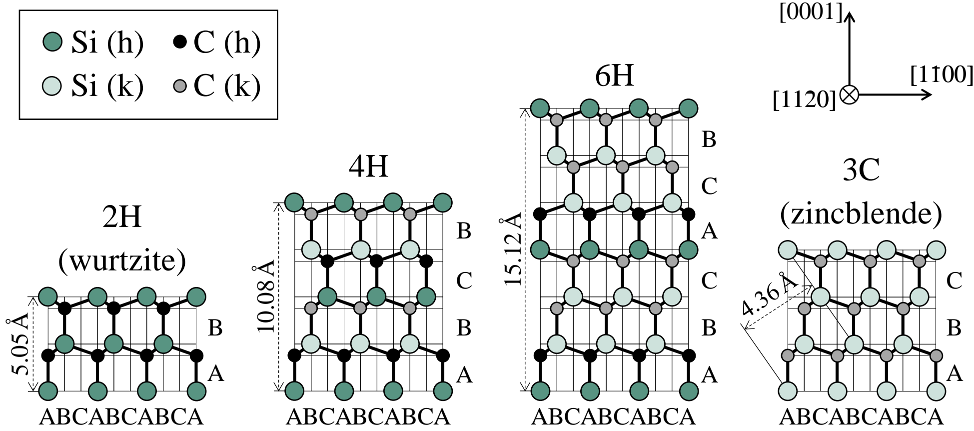

Figure 1.2: Stacking sequences and inequivalent lattice sites (h and k) of some of the most simple SiC polytypes viewed from the [11$\bar{2}$0] direction.

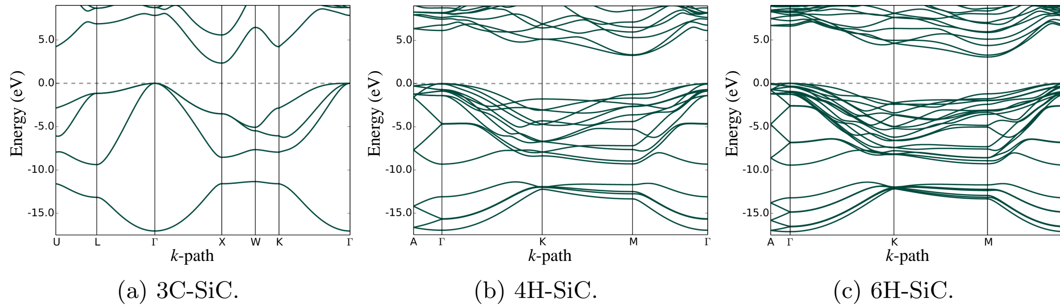

(a) 3C-SiC. (b) 4H-SiC. (c) 6H-SiC.

Figure 1.3: Band structures of different SiC polytypes calculated by HSE06 [25], courtesy of O.T. Hofmann [26].

1.2 Physical properties

Due its material properties that are superior to other semiconductors 4H-SiC is the polytype with the most attention for device applications. Table 1.2 shows a comparison of 4H-SiC with other semiconducting materials. It is evident that the properties of SiC are much more suitable for high temperature, high frequency and high power applications than Si and GaAs.

The wide bandgap results in an intrinsic carrier concentration many orders smaller than Si and GaAs which allows for a device being able to operate at higher temperatures. SiC devices have been demonstrated to be operational at temperatures as high as 600 °C [27, 28]. The breakdown field is approximately an order of magnitude higher than for Si and GaAs. Consequently, a much thinner layer of 4H-SiC can withstand a given voltage and in analogy an equivalent layer can withstand much higher voltages. SiC devices can withstand voltages well above 10 kV, e.g. an insulated-gate bipolar transistor (IGBT) blocking 22.6 kV has been fabricated [29]. The thermal conductivity is higher than for any metal, which allows for 4H-SiC to dissipate heat quickly. The saturated electron drift velocity is more than twice as high as for Si and GaAs allowing for high frequency operation of devices. 4H-SiC metal-semiconductor field effect transistors (MESFETs) can reach an oscillation frequency higher than 40 GHz [30].

While diamond and gallium nitride (GaN) have comparable or even better properties it must be noted that SiC processing technology is far more evolved to this date. This is partly due to the fact that compared to other wide-bandgap semiconductors SiC has one major benefit: it possesses a native oxide, silicon dioxide (SiO_2), which is the same as for Si and principally allows for processing using the same manufacturing lines. Therefore, many semiconductor manufacturers active in the Si market have been developing SiC technology, which is the reason for it being the most technologically mature among wide-bandgap semiconductors. SiC devices have become commercially available in form of light-emitting diodes (LEDs) [14], Schottky diodes [15], junction gate field-effect transistors (JFETs) [15], and also MOSFETs [16], among others.

Table 1.2: Material properties of 4H-SiC compared to other semiconductors [22, 31, 32, 33].

Property	4H-SiC	Si	GaAs	diamond	GaN
Bandgap energy (eV)	3.26	1.12	1.43	5.45	3.45
Breakdown field $\left(\times 10^5\,\mathrm{Vcm}^{-1}\right)$	32	3	4	57	30
Thermal conductivity $\left(\mathrm{Wcm}^{-1}\mathrm{K}^{-1}\right)$	4.9	1.5	0.46	22	1.3
Sat. electron drift velocity $\left(\times 10^7\,\mathrm{cm\,s}^{-1}\right)$	2.2	1.0	1.0	2.7	2.2
Electron mobility $\left(\mathrm{cm}^2\mathrm{V}^{-1}\mathrm{s}^{-1}\right)$	700-1200	1500	8500	2200	900-1250
Melting point (°C)	2830	1420	1240	4000	2500

1.3 Bulk growth

A good review on SiC bulk growth can be found in chapter 2 of the book "Silicon Carbide Microsystems for Harsh Environments" by M.B.J. Wijesundara and R.G. Azevedo [24]. As outlined above, SiC has a high chemical stability with a melting point of 2830 °C. While for Si it is possible to pull a single crystal out of molten Si with a seed crystal in the so-called Czochralski process [34, 35], for SiC this is not the case [36]. This has hindered the development of relatively fast and inexpensive growth of large SiC crystals with high quality until today, as different processes have to be used. While for Si typical growth rates of the crystal in the growth direction are some mm/min, for SiC they are at the most a few mm/h [37, 38]. Bulk crystals for commercial wafers are generally grown by seeded sublimation in a process often referred to as physical vapor transport (PVT) [9, 24, 39]. Figure 1.4 shows a schematic of how a crystal is grown by seeded sublimation. A seed crystal is placed on the top of the reaction chamber and the source material is heated to a temperature of about $2000 - 2500\,°\mathrm{C}$ [13]. The seed is held at a lower temperature which drives the sublimed Si and C containing vapor towards the crystal where it crystallizes [40]. With this method commercial wafers of up to 150 mm diameter are available today [14]. The most commonly used growth direction is the [0001] direction, often offsetted by a few degrees, as this results in the highest quality of wafers [39].

The growth of SiC bulk crystals is still facing many challenges. One problem lies within the relatively high density of extended defects such as micropipes, dislocations, stacking faults and unwanted changes of the polytype that reduce the yield of device manufacturing and cause reliability issues [12, 37]. While the growth conditions are still being optimized for a reduction of these unwanted defects, another challenge is to reduce the costs. Therefore, it is desired to obtain faster growth rates and to increase the size of wafers, which can both result in higher throughput.

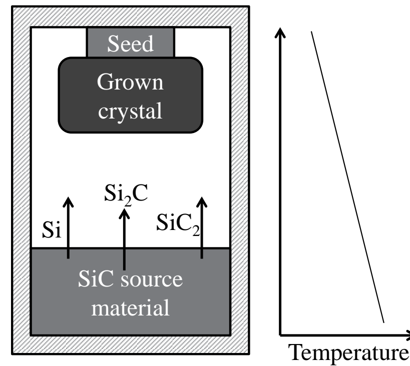

Figure 1.4: Schematic of a crucible for SiC crystal growth from seeded sublimation.

Alternative growing methods for bulk crystals are the seeded solution method [37, 41, 42] and the high temperature chemical vapor deposition (CVD) method [38]. Both methods result in higher quality crystals but are not yet able to compete with the established PVT methods, as the achievable wafer diameters are bigger with this method [37]. In order to reach the full potential of SiC for high power devices the quality of crystals and therefore the growing methods will have to be further improved in the future [12, 37].

1.4 Homoepitaxy

As-grown wafers with the processes outlined above have not yet reached a quality to be directly used for device processing. It is necessary to further improve the crystalline quality of the substrate, which is achieved by growing a homoepitaxial layer on top of a sublimation-grown wafer. Good introductions into the topic can be found in the references [22, 24, 43]. For SiC, the most commonly used process is the CVD process in a hot-wall reactor. Figure 1.5 shows a schematic of a simple hot wall reactor. A wafer is placed in a graphite susceptor with an opening that allows for the reaction gas to flow through. The reaction gas is composed of different Si and C-containing precursor molecules, e.g. silane (SiH_4) and propane (C_3H_8) [22], and a carrier gas, typically dihydrogen (H_2) [24]. The precursor molecules chemically react

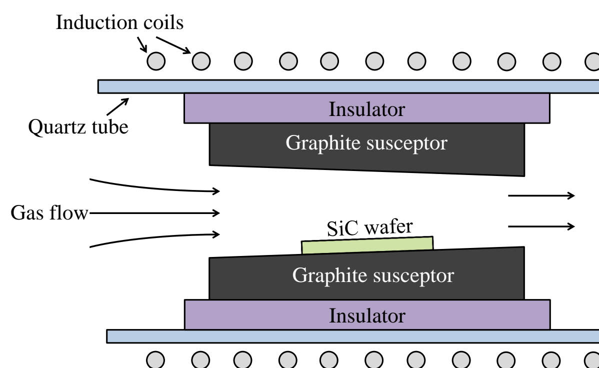

Figure 1.5: Cross sectional side view of a simple hot wall reactor.

with the surface resulting in epitaxial growth of the SiC crystal. The concept of a hot wall reactor results in efficient heating and a high uniformity of the temperature distribution in the wafer and allows for the growth of high quality epitaxial layers. Different reactor concepts have been realized, as reviewed in [24]. Typical temperatures for hot wall CVD are in the range of $1500 - 1650\,^{\circ}$C [22]. An alternative process is high temperature CVD and uses temperatures up to $2300\,^{\circ}$C [22]. The growth rates for epitaxially grown layers range between some tens of μm/h up to $250\,\mu$m/h for CVD and up to $800\,\mu$m/h for high temperature CVD [24].

One important issue in epitaxial growth is polytype control. When a new bilayer forms on top of an existing bilayer, the stacking order needs to be maintained so that there are no changes in the polytype. This is achieved by the step-controlled epitaxy process [10, 43, 44]. The basic formation process of a new bilayer is sketched in Figure 1.6. The (0001) surface of a crystal with some bilayer steps is shown. When a new bilayer starts to form on a (0001) terrace there are two possibilities how it can be stacked on the layer below. Evidently only one of them maintains the correct stacking sequence for a given polytype (see also Figure 1.2). The two possibilities differ in the angle of the bond directions of the new layer, i.e. whether a $60\,^{\circ}$ rotation in the bond directions takes place or not. This information is only passed on by the edges of the already existing layers. This effect can be used for polytype control by growing on substrates that do not have a perfectly aligned (0001) surface, but one that contains steps.

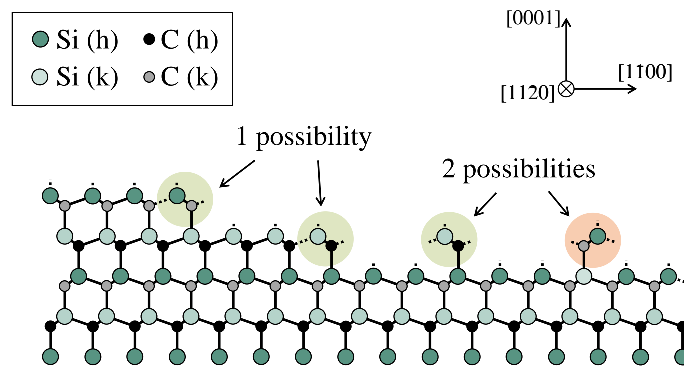

Figure 1.6: Schematic of the basic principle of polytype control by step-controlled epitaxy [43].

Figure 1.7 shows a schematic of a substrate with a surface that was polished with a certain tilt angle θ away from the (0001) plane. This results in a surface with an increased density of bilayer steps. The benefit of growing on such a tilted substrate is that the information on the proper stacking that maintains the polytype is communicated to the newly formed bilayers by the edges of the steps. While the new bilayers grow in the direction perpendicular to the [0001] direction, the epilayer as a whole grows in the direction of the cutting axis. Clearly, the off-cut angle plays an important role as the density of steps on the surface are dependent on it. Also the efficiency of the conversion of basal plane dislocations to less harmful threading edge dislocations is dependent on the tilt angle [45]. Typical angles used in commercial wafers are $4\,^{\circ}$ or $8\,^{\circ}$ [14]. Unlike what is shown in Figure 1.6 for better clarity, the steps in these commercial substrates are perpendicular to the [11$\bar{2}$0] direction.

Investigations of the surface morphology of the step structures on SiC substrates have shown that the steps tend to accumulate resulting in a faceted structure [46, 47, 48, 49]. Instead of uniformly distributed steps there are regions practically free of steps (terraces) followed by regions with several steps close together (macrosteps). The effect is commonly referred to

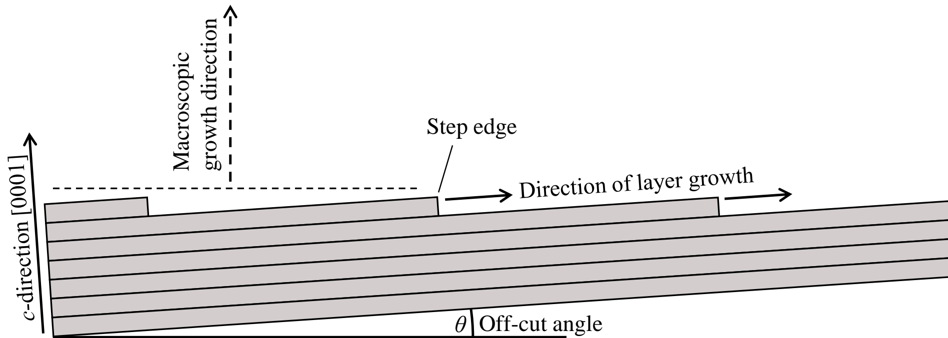

Figure 1.7: Schematic of crystal growth on an off-axis cut wafer.

as "step bunching". An interesting remark is that there is a tendency in 4H-SiC for one macrostep being composed of four bilayer steps (the height of one unit cell) or two bilayer steps (half the height of one unit cell) [48, 49, 50]. In other words two neighboring terraces tend to be equivalent in terms of symmetry, i.e. they both are h or they both are k.

1.5 Doping

Doping is used in all semiconductor materials in order to change the conductivity of the material. Doping is achieved by bringing impurity atoms into the crystal that generate energy states close to the band edges. In an n-doped material these states are close to the conduction band and result in an increased electron concentration. In a p-doped material the levels are close to the valence band and the concentration of holes is increased. The energy difference between the dopant energy level and the respective band edge is also known as the ionization energy. The ionization energy determines the doping concentration at a given temperature and concentration of donors and acceptors [22]. For a larger ionization energy the fraction of ionized dopants is smaller at a given temperature. A consideration of the temperature and dopant concentration dependence of the ionization rates for the most common dopants in 4H-SiC can be found in reference [22].

Doping of SiC substrates and epitaxial layers can be realized during growth by adding precursors containing the doping atoms [24, 43]. However, for device manufacturing it is required to form both n- and p-doped regions of specific geometry in a controlled way. A simple way to achieve this for other semiconductors is to drive in the dopant atoms by diffusion. One disadvantage for SiC is that it has low diffusion constants which practically allows for no migration of impurity atoms [31, 51]. For this reason selective area doping can only be achieved by ion implantation [51]. While ion implantation is a commonly used process in the semiconductor industry it has some disadvantages. On the one hand the dopant atoms are predominantly residing at interstitial sites after the implantation. On the other hand the implantation creates damage in the crystal lattice. High temperature anneals are required in order to move the dopants to the desired substitutional lattice sites and to heal the damage in the crystal. In SiC these anneals are typically carried out at temperatures of about 1700 °C and above [52]. However, even after the anneals point defects can remain in the crystal and influence the performance of a device. What adds to the problem are the relatively high ionization energies even for the shallowest dopants, requiring generally a higher concentration of dopants to be implanted. This again increases the lattice damage due to the implantation.

The doping concentrations achievable with ion implantation for device applications range from the high $10^{16}\,\text{cm}^{-3}$ to the low $10^{20}\,\text{cm}^{-3}$ [51].

1.5.1 *n*-type doping

All group V elements (N, P, As, Sb, and Bi) have been demonstrated to be *n*-type dopants [53, 54, 55]. However, N is the most commonly used shallow donor in 4H-SiC and is also the one used for all samples described in this work. It is preferred due to its low ionization energy and low mass [51]. It has been shown that N substitutes for C in the SiC lattice [56]. In 4H-SiC the substitutional nitrogen at the carbon site (N_C) can reside either in the h or in the k site. As the sites are inequivalent it is not surprising that they differ in certain properties. For the former the ionization energy is $\approx 61\,\text{meV}$, while for the latter it is $\approx 125\,\text{meV}$ [57]. The site dependence also results in significantly different electron paramagnetic resonance (EPR) parameters which have been extensively studied in the literature [58, 59, 60, 61].

In order to achieve device regions with low resistivity, high doping concentrations in the range of $n \approx 10^{19}\,\text{cm}^{-3}$ are required. One problem that has often been reported for highly N-doped SiC is dopant deactivation. For implantation doses exceeding $5 \times 10^{19}\,\text{cm}^{-3}$ the carrier concentration saturates [51]. The problem is, that not all the implanted N forms N_C donors, but also other defect complexes. These complexes may be electrically inactive, or deeper in the bandgap. Therefore, they do not contribute to the doping. The mechanism for this dopant deactivation is still under debate. Suggestions include the formation of Si-N complexes [62], Si-C-N complexes [63], or N complexes with intrinsic defects [64]. Especially the last of these suggestions has been studied extensively, as the damage of the ion implantation results in an increased density of intrinsic defects like vacancies and interstitials. It is reasonable to assume that N would react with these defects to form complexes during the dopant activation anneal. Further discussions on intrinsic and N-related defects can be found in section 1.7.

1.5.2 *p*-type doping

Acceptors in SiC are the group III elements B, Al, and Ga, as well as the group II element Be [51]. Al is the most common acceptor, as it has the lowest ionization energy and a high solubility in SiC [51]. All samples used in this study are *p*-doped with Al. It substitutes for Si and also shows some site dependence. The ionization energy of the substitutional aluminum at the silicon site (Al_{Si}) is $\approx 198\,\text{meV}$ for the h site and $\approx 201\,\text{meV}$ for the k site [57]. These values are significantly higher than for the N_C and result in a significantly smaller ionization rate. For a dopant concentration of $10^{17}\,\text{cm}^{-3}$ the ionization rate at room temperature for Al acceptors is only $\approx 15\,\%$ while for N donors it is $\approx 90\,\%$ [22]. However, the dopant deactivation due to formation of other defect complexes than the Al_{Si} acceptor seems to be less of a problem and high activation can be achieved for the implanted Al [51, 65, 66].

1.6 The SiC-SiO_2 interface

In order to manufacture SiC-MOSFETs, an insulating gate oxide needs to be formed on the SiC substrate. SiC is the only wide-bandgap semiconductor that possesses a native oxide. Like for Si, the native oxide of SiC is SiO_2. Therefore, an SiO_2 layer can be grown on a SiC substrate by a thermal oxidation. The grown oxide layers have a comparable bulk quality to those grown on Si [67]. However, the SiC-SiO_2 interface has inferior properties compared to the Si-SiO_2 system [67, 68]. The mobility right at the interface, which is a key parameter for power MOSFETs, is well below the bulk value of $\mu_n \approx 1000\,\text{cm}^2\text{V}^{-1}\text{s}^{-1}$ [69, 70, 71]. Even

in commercially available state of the art MOSFETs the mobility is below $100\,\mathrm{cm^2V^{-1}s^{-1}}$ [72]. Consequently, until today numerous studies have been performed to learn more about the structure of the SiC-SiO_2 interface and the mechanisms that degrade the mobility in order to find ways of improving the performance of SiC MOSFETs. There is a certain consensus that the main reason for the low mobility is a high density of interface traps (D_{it}) [68, 73, 74, 75]. In the following the SiC-SiO_2 system is explained and the current status in terms of its characterization and understanding is reviewed.

1.6.1 MOSFETs

Before continuing with properties of the SiC-SiO_2 interface, a few important considerations on SiC MOSFETs are given here. For a detailed introduction into the principles of MOSFETs the reader is referred to the referenced textbooks [76, 77, 78]. In this section only the most basic principles relevant for this work are shown. It shall be noted that the current research is mostly focused on *n*-channel MOSFETs, due to the higher electron mobility, as shown in table 1.1. Consequently, all further considerations are made for the example of an *n*-channel MOSFET.

A MOSFET is an electronic device where the conductivity of a channel between two electrodes, the source and drain, can be controlled by the voltage applied to a third contact, the gate. The gate is electrically insulated from the substrate by a dielectric, usually SiO_2. A fourth contact goes to the *p*-substrate and is called the body. It is often shorted with the source. Figure 1.8 shows a very simplistic conceptual images of a SiC MOSFET. A MOSFET can be used as a switch, allowing practically no current to flow through the channel when it is "off" and having a very low resistance when it is "on". Power MOSFETs are a special category of MOSFETs that are used in circuits where high voltages and/or currents occur. Generally, a power MOSFET must block high voltages in the "off" state and allow the flow of high currents in the "on" state. For the latter it is particularly important to result in a low resistance of the channel so that the dissipated power in the device itself is minimized.

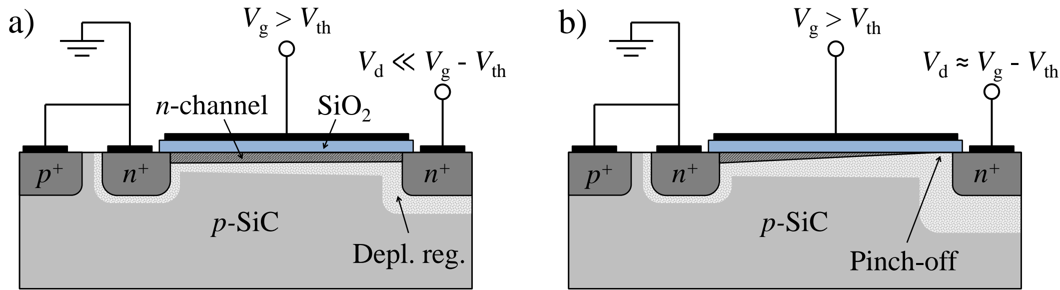

Figure 1.8: Schematic of a SiC *n*-channel MOSFET: a) biased in the linear region, b) biased at the transition from the nonlinear to the saturation region.

The conductivity of the channel is controlled by the gate voltage V_{g} which can change the Fermi level and the charge density Q_{i} at the SiC-SiO_2 interface. An important figure is the threshold voltage V_{th} at which the channel is inverted:

$$V_{\mathrm{th}} = V_{\mathrm{fb}} + 2\Psi_{\mathrm{b}} + \frac{\sqrt{4\epsilon_{\mathrm{SiC}} q_{\mathrm{e}} N_{\mathrm{a}} \Psi_{\mathrm{b}}}}{C_{\mathrm{ox}}}. \tag{1}$$

with the flatband voltage V_{fb}, the bulk potential Ψ_{b}, the permittivity of SiC ϵ_{SiC}, the elementary charge q_{e}, the acceptor density N_{a}, and the oxide capacitance C_{ox} [76]. V_{fb} is dependent on the charge density at the interface and in the oxide [77]. Consequently, if the charge density is changed, e.g. by trapping of charge in the oxide, it causes a threshold voltage shift ΔV_{th}. Ψ_{b} in equation (1) is simply the offset of the Fermi Energy E_{F} from its intrinsic level E_{i} in the body region far away from the channel, which is dependent on the doping

$$\Psi_{\text{b}} = \frac{E_{\text{i}} - E_{\text{F}}}{q_{\text{e}}} = \frac{k_{\text{B}}T}{q_{\text{e}}} \ln \frac{N_{\text{a}}}{n_{\text{i}}} \tag{2}$$

with the Boltzmann constant k_{B}, the temperature T, and the intrinsic carrier concentration n_{i} [78]. In the following, the dependence of the drain current I_{d} on the applied voltages is discussed. Different operation regions which depend on V_{g}, V_{th} and the drain voltage V_{d} are defined. The sub-threshold region ($V_{\text{g}} < V_{\text{th}}$) is of minor importance for device operation, as long as the channel can be shut off sufficiently. More important are the regions as follows:

- The linear region ($V_{\text{d}} \ll V_{\text{g}} - V_{\text{th}}$): Figure 1.8 a) shows a MOSFET biased in the linear region. The n-channel has an ohmic resistance and the inversion charge density Q_{i} is approximately uniform over the channel. In the linear region I_{d} is proportional to V_{d}:

$$I_{\text{d}} \approx \frac{W}{L} \mu_n C_{\text{ox}} \left(V_{\text{g}} - V_{\text{th}}\right) V_{\text{d}} \tag{3}$$

  with the length L and width W of the channel, and the electron mobility μ_n.

- The nonlinear region ($V_{\text{d}} < V_{\text{g}} - V_{\text{th}}$): The space charge region close to the drain side due to the reverse-biased drain-to-body diode expands with increasing V_{d}. As the space charge region expands, the inversion charge density Q_{i} in the n-channel close to the drain side is decreased. The current is no longer proportional to V_{d}, because Q_{i} is not uniform over the whole channel length any more. The point where Q_{i} at the drain side is decreased to practically zero, is called "pinch-off point", as indicated in Figure 1.8 b). In the nonlinear regime I_{d} is given by the expression:

$$I_{\text{d}} = \frac{W}{L} \mu_n C_{\text{ox}} \left(V_{\text{g}} - V_{\text{th}} - \frac{V_{\text{d}}}{2}\right) V_{\text{d}}. \tag{4}$$

- The saturation region ($V_{\text{d}} \gg V_{\text{g}} - V_{\text{th}}$): In this region the channel is pinched off and there is no more dependence of I_{d} on V_{d} as the voltage drop from the pinch-off point to the source remains constant (unless L is very short). The pinch-off point simply moves from the drain towards the source with increasing V_{d}. I_{d} is approximated by the equation:

$$I_{\text{d}} = \frac{W}{2L} \mu_n C_{\text{ox}} \left(V_{\text{g}} - V_{\text{th}}\right)^2. \tag{5}$$

All of the described regimes have in common that the current is proportional to the term $\frac{W}{L} C_{\text{ox}}$ and μ_n. While the former can easily be changed by design, the latter is a physical parameter dependent on scattering that is hindering the motion of the carriers in the channel. Different scattering mechanisms can be present at the same time, all of them having an associated mobility μ_i. The total mobility μ_{tot} is given by Mathiessen's rule [77]:

$$\frac{1}{\mu_{\text{tot}}} = \sum_i \frac{1}{\mu_i}. \tag{6}$$

The different mobility contributions μ_i have different physical origins. Some examples for these mechanisms are ionized impurity scattering, acoustic phonon scattering, Coulomb scattering, surface roughness scattering, and surface phonon scattering [77, 79, 80, 81]. Due to their different physical origins the scattering mechanisms have different dependencies on the temperature and on the electric field. Therefore, studying the mobility dependence on T, V_g and V_d can give an insight to what scattering mechanism is dominant. The mobility can generally be extracted from the measured electrical characteristics of a MOSFET, which is usually performed in the linear region. However, these measurements are only approximations of the real mobility μ_n. The mobility extracted from the output characteristics is commonly referred to as effective mobility μ_eff and is given by the equation [77]:

$$\mu_\mathrm{eff} = \frac{L}{WC_\mathrm{ox}\left(V_\mathrm{g} - V_\mathrm{th}\right)} \left.\frac{\partial I_\mathrm{d}}{\partial V_\mathrm{d}}\right|_{V_\mathrm{g}=\mathrm{const}} . \tag{7}$$

The mobility extracted from the transfer characteristics is commonly called field effect mobility μ_FE and is given by the equation [77]:

$$\mu_\mathrm{FE} = \frac{L}{WC_\mathrm{ox}V_\mathrm{d}} \left.\frac{\partial I_\mathrm{d}}{\partial V_\mathrm{g}}\right|_{V_\mathrm{d}=\mathrm{const}} . \tag{8}$$

Since the dependence of the mobility on the electric field is neglected in the case of μ_FE it is generally lower than μ_eff, and less suitable for an appropriate device characterization [77]. A more sophisticated approach for evaluating the mobility and V_th from the transfer characteristics has been described by G. Ghibaudo in [82]. He derived the linear function

$$\frac{I_\mathrm{d}}{\sqrt{g_\mathrm{m}}} = \sqrt{\frac{WC_\mathrm{ox}\mu_\mathrm{LF}V_\mathrm{d}}{L}}\left(V_\mathrm{g} - V_\mathrm{th}\right) \tag{9}$$

where g_m is the transconductance, which is simply the term $\left.\frac{\partial I_\mathrm{d}}{\partial V_\mathrm{g}}\right|_{V_\mathrm{d}=\mathrm{const}}$ from equation (8). This equation holds at high gate voltages and allows for evaluating μ_LF from the slope and V_th from the intercept of a linear fit [82].

The quality of the SiC-SiO_2 interface strongly affects the resulting mobility of the carriers in the channel of a SiC MOSFET. Investigations have shown that a high density of interface traps D_it causes a severe mobility reduction [74, 75]. The mobility limiting scattering mechanisms at room temperature is Coulomb scattering, while at high gate voltages surface roughness dominates [74, 83]. In addition to scattering, the carrier trapping in deep levels can reduce the carrier lifetime and add to the channel resistance, as it reduces the amount of carriers present in the channel.

Reducing the D_it and maximizing the mobility of SiC MOSFETs is one of the main targets of current technology development. An important step is to learn more about the structure of the SiC-SiO_2 interface region and the origin of the D_it that reduces the mobility.

1.6.2 Oxidation

There is one main difference between oxidation of Si and SiC: the presence of C in the latter. There are the strong bonds between the C and Si atoms in SiC that need to be broken during oxidation. For this reason, the oxidation of SiC requires a higher thermal budget than Si for an oxide layer of a certain thickness to be formed. There is also a strong dependence of the growth rate on the crystalline orientation of the growing surface. The C-face $(000\bar{1})$ has the fastest growth rate, the Si-face (0001) has the lowest, and the a-face $(11\bar{2}0)$ is in between, but they are all below the growth rate of SiO_2 on Si [84].

The oxidation process can be described as follows. The diatomic oxygen (O_2) molecules diffuse through the already grown layer of SiO_2 down to the interface where the following chemical reaction takes place:

$$2SiC + 3O_2 \rightarrow 2SiO_2 + 2CO. \tag{10}$$

On the one hand the Si atoms are oxidized to SiO_2 which creates an oxide layer as the oxidation front moves further into the SiC. On the other hand the C atoms are oxidized to carbon monoxide (CO) and also further to carbon dioxide (CO_2) [85]. These oxidized C molecules need to diffuse out through the oxide and be removed, as they have no function in the grown oxide layer. If the C atoms are not removed completely one would expect some C excess residing at or very near the interface. This has often been suspected to cause the degraded properties of as-grown SiC-SiO_2 interfaces. The C excess has been suggested to result in the formation of graphitic layers [68], C clusters [68, 86], non-stoichiometric layers [87, 88, 89, 90], and C pairs [91, 92, 93]. The C excess could be explanation for the observed density of states deep in the bandgap (see section 1.6.3) [68]. However, some recent studies have put the existence of C excess in question [94, 95, 96].

An alternative process of oxide layer formation is CVD. In this process, a carrier gas containing precursor molecules of SiO_2 is brought to the sample. It decomposes to free radicals that deposit onto the sample and form the oxide. The carrier gas used for the samples in this work was tetraethyl orthosilicate ($Si(OC_2H_5)_4$). The decomposition is achieved either by a plasma ignition or by an elevated temperature. For more information on CVD processing the reader is referred to the reference [97]. The benefit of oxide deposition using CVD is that no C needs to diffuse away from the interface and there is no oxidation front moving into the SiC substrate. However, the oxide layers that are deposited onto the substrate are not bound very well, which makes a (short) thermal oxidation indispensable. This step can follow the deposition process in the form of an annealing step in various ambient environments [75, 98, 99]. The anneal assures a good physical contact between the SiC and the SiO_2 and densifies the oxide. The benefits of deposited oxides are the smaller thermal budget and faster processing [100]. It was shown that deposited and subsequently annealed oxides result in a higher channel mobility than thermal oxides [100].

1.6.3 Characterization of the D_{it} at the SiC-SiO_2 interface

As mentioned above, there is a high D_{it} present at the SiC-SiO_2 interface. Fundamental work in the characterization was carried out by V.V. Afanasev et al. [68]. Figure 1.9 shows experimental data of how this D_{it} is distributed in the SiC bandgap. Generally, there is a high D_{it} distributed over the whole bandgap at 4H-SiC-SiO_2 interfaces. The D_{it} can be divided into three groups: Defects close to the valence band, defects close to the conduction band, and deep level defects. For *n*-channel MOSFETs the defects close to the valence band are of little importance, as they only influence hole transport. The other two groups have more dramatic effects on the device performance and are more closely discussed in the following.

Starting with the interface states close to the conduction band, Figure 1.9 clearly shows that the D_{it} sharply increases towards the conduction band edge. The D_{it} for 4H-SiC results in a maximum value of $D_{it} \approx 10^{13}\,cm^{-2}eV^{-1}$ just below the conduction band which is about one order of magnitude higher than for 6H-SiC. It was suggested that the origin of the increasing D_{it} is the same for different polytypes but due to the wider bandgap mostly affects 4H-SiC [71, 101, 102]. As this peak in the D_{it} is present in different polytypes and always appears at the same energy with respect to the valence band it is commonly interpreted to be due to intrinsic defects in the oxide. These defects have to be close to the the interface in order to be accessible

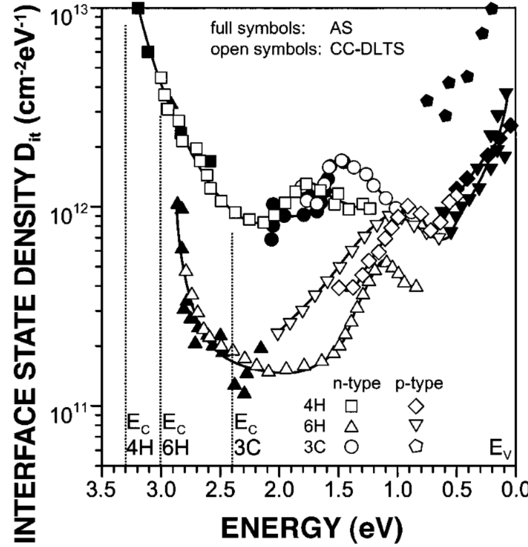

Figure 1.9: D_{it} as a function of the energy above the valence band for different n- and p-metal-oxide-semiconductor (MOS) capacitors on different SiC polytypes determined by admittance spectroscopy (full symbols) and deep level transient spectroscopy (DLTS) (open symbols). The conduction bands for the respective polytypes are marked by dotted lines. The Figure was taken from [68], with permission.

to charge carriers from the SiC and are, therefore, often referred to as near-interface traps (NITs) [68, 103]. In Si MOSFETs and SiC polytypes with a smaller bandgap these defects play a minor role as they are located above the conduction band [68, 101]. However, in 4H-SiC these defects are in the bandgap and can act as trapping centers for electrons [101]. As a consequence, a large fraction of the inversion layer charge in an n-channel MOSFET is trapped and becomes immobile, which results in a degraded mobility [71]. Additionally, the trapped charge causes Coulomb scattering, which further reduces the mobility [71]. Even though SiO_2 is a well-studied material, the origin of these oxide defects is not clear. There is an intrinsic trap level in SiO_2 approximately 2.8 eV below the conduction band which matches the energy of the NITs [68, 104]. In a recent theoretical study it was shown that electrons can be trapped by a Si atom in the oxide if the O-Si-O angle is larger than 132 ° [105]. However, until now there is no experimental confirmation of this model or an identification of the intrinsic oxide trap assigned to the NITs.

The D_{it} deep in the bandgap of 4H-SiC is about one order of magnitude smaller than close to the conduction band, as can be seen if Figure 1.9. It is more or less constantly distributed over the whole bandgap [100, 101]. Several distinct peaks in the D_{it} deep in the bandgap have been reported, as discussed in the work by P. Déak et al. [103]. While their influence on the mobility is less harmful compared to the defects close to the conduction band, they are still active defects that can act as recombination centers and decrease the carrier lifetime [106, 107]. In as-processed Si MOSFETs, the D_{it} is dominated by silicon dangling bond (P_b) centers [108]. However, for SiC there is no evidence for P_b centers playing a major role [68]. As the main difference between Si and SiC is the presence of C it is often argued that the high D_{it} has to be related to C. It is certainly a reasonable model, that C residuals or clusters of different sizes would result in a broadly distributed D_{it} [68]. An alternative model explaining the D_{it} deep

in the bandgap are non-stoichiometric transition layers at the interface [109]. However, there is still no clear identification of these C-related defects. Theoretical modeling of the four most pronounced peaks deep in the bandgap has assigned them to C dimers and C split interstitials [91, 92, 103]. The former is a doubly bonded C pair that can also be present in the oxide and is assigned to the shallower peaks of the D_{it} [92, 103]. The latter is a pair of C atoms sharing a C lattice site next to the interface and is assigned to the peaks deepest in the bandgap [91, 103]. As the C pair for this defect is only singly bonded it can be understood as a pair of carbon dangling bond (P_{bC}) centers. Several EPR studies of the SiC-SiO_2 system reported on P_{bC} centers [110, 111, 112, 113], while they do not necessarily agree in terms of the observations and their interpretations, as discussed in section 1.7.3. Theoretical calculations can be very useful to for the interpretation of EPR data, especially in such a complex system like the SiC-SiO_2 interface. A major problem that theoretical modeling is facing is that the exact microscopic interface structure is still unknown, as discussed in the following.

1.6.4 Interface structure

Most commercial 4H-SiC substrates are grown with a certain offset angle with respect to the *c*-plane. This results in a step bunching of the surface of the substrate, as discussed in section 1.4. Transmission electron microscopy (TEM) investigations of the SiC-SiO_2 interface have shown that the step bunching persists after the oxidation [94, 100, 114]. However, there is a dependence on the oxide processing as a much more pronounced step bunching is observed for oxides formed by CVD compared to thermal oxides [100]. It was shown by the work of F. Roccaforte et al. that the step bunching has no negative effects on the mobility [73]. In fact it was shown that faceted interfaces result in higher channel mobilities than flattened interfaces [115]. It was speculated whether the post-oxidation anneals (see section 1.6.5) that are used to passivate interface traps are more efficient on a vicinal interface due to a higher fraction of steps in the $[11\bar{2}0]$ direction [73]. Another explanation was that periodically ordered steps would be little hindering for electron Bloch waves, while small scale deviations from such an ideal structure could cause more scattering [94]. While the influence of the surface morphology is still not well understood, it was shown that for both flat and faceted interfaces the mobility is dominated by Coulomb scattering due to trapped charge [73].

The model of C excess from the oxidation process has led to many investigations for finding direct evidence for this. Several TEM studies found hints for an interlayer in the Z-contrast images and in electron energy loss spectroscopy (EELS) linescans [88, 89, 116]. However, in very recent studies no such interlayers with increased C content were found [94, 95, 96, 100, 117, 118, 119]. Nonetheless, what all these studies have in common is that there is a certain transition region of a few nm where the stoichiometry gradually changes from bulk SiC to SiO_2, though the measured values range from 1.5 nm up to 25 nm, indicating a strong dependence on the studied samples and experimental conditions [89, 120]. It was shown that the width of the transition region can be measured by different methods all leading to slightly different results, with the chemical shift of the Si-$L_{2,3}$ edge onset being the most reliable method [95]. Some studies found a strong correlation between the measured transition region width and the mobility [89, 95], while other studies found the opposite [120]. It is not clear with certainty whether the transition region is a region with different stoichiometry or simply interface roughness, since the interface has been shown not to be atomically flat [94]. For simulations using atomistic models of the interface such knowledge could be very helpful, as the outcome depends on the assumed interface model and bonding structure.

1.6.5 Post-oxidation annealing

In Si technology, the D_{it} (composed of P_b centers) can be efficiently passivated by post-oxidation anneals (POAs) in H-containing atmospheres [71]. For SiC this is not the case [68]. However, it has been shown that POAs in N-containing ambient significantly improve the quality of the SiC-SiO_2 interface and the performance of SiC MOSFETs [71]. It is well established that the best results can be achieved with nitric oxide (NO) [70, 75, 121, 122]. The exact mechanism of the N passivation of defects is still under debate, especially since the origin of the D_{it} is not yet completely understood. It has been suggested that the N atoms may remove the excess C atoms or saturate dangling bonds at the interface [103, 122]. Another effect that may influence the conductivity of inversion layers is the creation of donor states by the incorporated N atoms in the SiC close to the interface [123, 124]. The N passivation leads to a higher mobility at the *a*-face compared to the Si-face [120, 123]. This indicates that this face has a higher reactivity and the passivation is more efficient [73, 123].

The N profiles at the SiC-SiO_2 interface have been investigated with various methods [71]. X-ray photoelectron spectroscopy (XPS) and secondary ion mass spectroscopy (SIMS) as well as energy-dispersive x-ray spectroscopy (EDS) have shown an increased N intensity close to the interface [118, 125]. Very recent studies demonstrated that the N concentration is strongly bound to the SiC side of the interface, as it persists after etching away the oxide [120, 126, 127]. It was estimated that the N concentration at the interface is up to the equivalent of one atomic layer [126] and confined within a layer of $\approx 1\,\mathrm{nm}$ [71]. Even though such a concentration should be detectable by EELS, there is only a limitted number of EELS studies that showed a small N peak at the interface [119, 128]. Note that both of these studies only showed clearly resolved N peaks on C-face interfaces, while in the present work only Si-face devices were studied. None of the other referenced studies reported on any N concentration detectable by EELS at the Si-face. An effect reported in some EELS studies was a decrease in the thickness of the transition region at the interface after N passivation [89, 95]. However, other studies observed no such trend or even the opposite effect [96, 120].

It was shown that the N concentration at the interface saturates after a few hours of annealing, while the mobility is still well below the bulk value [70, 129]. Increasing the N concentration has also been reported to increase fast states at the interface [130]. In addition, an increase of hole traps in the oxide has been reported [129]. A very recent study compared the resulting on resistances and threshold voltage shifts after positive bias temperature stress (PBTS) of SiC MOSFETs for different NO annealing times and temperatures [131]. It was shown that a POA aiming to optimize one parameter degrades the other and vice versa. Consequently, the interface passivation by NO annealing, despite being the current standard in industry, may still be improved or combined with other processes.

Combining NO anneals with H has shown to result in a higher mobility but also increases reliability issues [71]. An alternative process is the passivation using P. Anneals in phosphoryl chloride ($POCl_3$) result in higher channel mobilities than NO anneals [73]. The mobility of a $POCl_3$-annealed SiC MOSFET decreases with temperature, as opposed to the case of N-passivation, suggesting that the dominant scattering mechanism is phonon scattering [132]. Therefore, the passivation effects of P are somewhat different than those of N. However, it was also shown that some serious reliability issues due to the incorporation of P atoms into the oxide remain [133]. Consequently, research aiming to find better annealing processes is ongoing.

1.7 Point defects in SiC

As discussed above, defects play an important role in the performance of SiC devices. Different experimental methods can be used to study point defects, including EPR [134, 135, 136], photoluminescence (PL) [135], positron annihilation spectroscopy [135], Raman spectroscopy [137], and DLTS [68]. However, theoretical *ab initio* calculations, often performed using density functional theory (DFT), are usually combined with these experimental techniques [138]. The most powerful experimental techniques are EPR and related methods like electrically detected magnetic resonance (EDMR) as they give direct information on the chemical structure of the studied defects (see also chapter 2). Many point defects in SiC, SiO_2 and their interface region have been identified using EPR, usually combined with theoretical calculations. One drawback of EPR is that it can only be used to study defects with one or more unpaired electrons, i.e. paramagnetic defects. However, as SiC is a wide-bandgap semiconductor there are usually several accessible charge states of a given defect in the bandgap. Out of these some are paramagnetic and some are not. The Fermi level position determines which states are occupied and thus visible in a EPR experiment. Some defects possess multiple accessible paramagnetic states in the bandgap [6, 139]. A list of EPR parameters obtained from several known and unknown defects in different charge states can be found in [140]. Reviews on the identifications of various defects in SiC are found in [59, 61, 138, 141, 142]. The study of point defects in SiC is ongoing, especially with a scope on electrically active defects that limit the performance of devices. Point defects in SiC have also gained more attention recently for possible quantum computing applications [143, 144, 145, 146, 147]. While other systems, like the well-known nitrogen vacancy (NV) center in diamond have superior properties to be used as a qubit [143], SiC benefits from its industrial maturity and availability of large high quality substrates. The most important identified defects for the scope of the present work are reviewed in this section. The first part focuses on intrinsic bulk defects, the second part on defects related to N doping, and the third part on defects at the SiC-SiO_2 interface.

1.7.1 Intrinsic bulk defects

The term intrinsic defects generally refers to defects that do not contain impurity atoms or larger aggregations of defects. For a compound material like SiC there are three basic types of intrinsic defects: vacancies, interstitials, and antisites. A vacancy is an unoccupied lattice site, an interstitial is an additional atom in between lattice sites, and an antisite is an atom of one species residing in a lattice site usually occupied by an atom of the other species. For SiC this gives a total of six basic intrinsic defects. However, in the literature also small defect complexes made up by these basic defects are often referred to as intrinsic defects [138]. Intrinsic defects in SiC that have been successfully identified using EPR are the carbon vacancy (V_C) [139], the silicon vacancy (V_{Si}) [136], the divacancy (V_CV_{Si}) [148], the carbon antisite (C_{Si}) [149], the antisite pair (Si_CC_{Si}) [150], and the C_{Si} coupled to a V_C ($C_{Si}V_C$) [151]. The following discussion only focuses on a selection of defects that have significant concentrations in 4H-SiC and are electrically active [152].

The carbon vacancy (V_C)

The V_C is among the intrinsic defects with the lowest formation energy leading to a high abundance [143, 153]. It possesses several charge states in the bandgap out of which the positive ($V_C{}^+$) and negative ($V_C{}^-$) are paramagnetic and have been identified using EPR [139, 154, 155]. In intrinsic high-purity 4H-SiC the $V_C{}^+$ is the dominant defect [142]. This defect has a strong site dependence, which results in a different structure for the k than for the

h site. While the former reconstructs in a Jahn-Teller like way lowering the symmetry to C_{1h}, the latter maintains the C_{3v} symmetry of the initial defect [138, 142]. As a consequence, the distribution of the unpaired electron densities are different resulting in two different resonance spectra. Both spectra have been observed with EPR in electron irradiated 4H-SiC and were labeled EI5 and EI6 [156]. While the former was correctly assigned to the V_C^+ [156], the latter was wrongly assigned to the silicon antisite (Si_C) [157]. Only by combining theoretical predictions with the experimentally observed EPR curves was it possible to identify the EI5 as the V_C^+ (k) and the EI6 as the V_C^+ (h) [139]. At room temperature both types of the V_C^+ show a smaller g-factor parallel the the c-direction ($g_{c\|B} \approx 2.0032$) than for the directions perpendicular to the c-direction ($g_{c\perp B} \geq 2.0046$) [140, 141]. The hyperfine (HF) structures are dominated by the four Si atoms next to the vacancy, which have HF splitting constants in the range of $a_{\mathrm{Si}} \approx 20 - 120\,\mathrm{G}$ at room temperature [139, 141].

In n-type material the V_C exists in the negative charge state. The V_C^- (h) has been identified by EPR soon after the V_C^+, while the V_C^- (k) has not been found, although theoretically predicted [141, 155]. At room temperature the V_C^- (h) has an almost isotropic g-factor of $g \approx 2.0039$ and shows a pronounced HF interaction with its four Si neighbors with the HF splitting constants in the range of $a_{\mathrm{Si}} \approx 40 - 90\,\mathrm{G}$ at room temperature [140, 155, 158]. The V_C^- (k) was only identified recently by EPR measurements under illumination at low temperatures but is not detectable at room temperature [158, 159, 160].

The V_C has been assigned to the $Z_{1/2}$ defect which is a well-known lifetime killer in 4H-SiC, by comparing concentrations obtained by DLTS with those obtained by EPR [161]. It was also associated with the deep level defects labeled $EH_{6/7}$ [159]. Despite these assignments of the V_C to deep level defects which should potentially be detectable with EDMR, no such measurements of the V_C have been reported so far.

The silicon vacancy (V_{Si})

The V_{Si} is a well-studied intrinsic defect in 4H-SiC, even though its formation energy is $\approx 3 - 4\,\mathrm{eV}$ higher than that of the V_C (for both defects in the neutral charge state) [143, 153]. Like the V_C it has several paramagnetic states in the bandgap out of which the V_{Si}^- was the first observed in EPR experiments [136]. The V_{Si} is very different from the V_C, as no Jahn-Teller reconstruction takes place and the C dangling bonds are simply pointing inwards to the vacancy without forming bonds with each other. As a consequence, the V_{Si} prefers high-spin states [141, 153].

The V_{Si}^- is a spin $S = 3/2$ state with a high isotropy and a g-factor of $g \approx 2.0030$ [136, 140, 141]. There are pronounced HF splittings due the four C neighbors ($a_C \approx 12 - 29\,\mathrm{G}$) and due to the twelve Si next neighbors ($a_{\mathrm{Si}} \approx 3\,\mathrm{G}$) [136]. Unlike the V_C, there is very little difference between the k and h site for the V_{Si}^- [141]. Despite the high spin state there is no zero-field splitting observable. However, a defect with a pronounced zero-field splitting that is often observed along with the V_{Si}^- is the T_{V2a}-center [141, 162, 163]. This defect was associated with the neutral charge state (V_{Si}^0) as the observed lines suggested a spin $S = 1$ defect [162]. It was later shown, that also the T_{V2a} is a spin $S = 3/2$ defect and was assigned to the V_{Si}^- with lowered symmetry and a pronounced zero-field splitting [141, 163, 164]. While further doubts about this assignment have been raised [165, 166], there is a broad agreement on the high-spin ground state of the V_{Si} making it a promising candidate for quantum computing applications [146, 165, 166].

The carbon antisite vacancy pair ($C_{Si}V_C$)

It has been predicted that the V_{Si} is only stable in n-type and metastable in intrinsic and p-type SiC where it can reconstruct to the $C_{Si}V_C$ [167]. The center has been identified in the negative [151] and positive charge state [168, 169]. Each come in four configurations due to the inequivalent lattice sites in 4H-SiC. The $C_{Si}V_C{}^+$ is observable at room temperature and shows a strong site dependence with different angular dependencies of their g-factors and HF patterns for each of them [169]. This is a strong contrast to the highly ordered V_{Si} and should be kept in mind in the study of p-type material. Irradiation and annealing studies suggested the $C_{Si}V_C$ to play a certain role in the compensation of N-donors [151].

The divacancy (V_CV_{Si})

The V_CV_{Si} is a highly stable defect that can form by migration of the V_C and the V_{Si} [170]. Like the V_{Si} it has a high formation energy but was often observed in EPR experiments [144, 148, 171, 172]. The center has been identified in its neutral charge state $V_CV_{Si}{}^0$ by comparison of calculated and measured EPR parameters [148]. Like the $C_{Si}V_C$ it comes in four inequivalent configurations. The $V_CV_{Si}{}^0$ is characterized by its spin $S = 1$ ground state with a large zero-field splitting for all four configurations [148]. This makes the V_CV_{Si} one of the defects being in the focus for quantum computing applications [144, 172]. The V_CV_{Si} is also a precursor for N dopant deactivation [173].

1.7.2 Nitrogen related bulk defects

The most commonly used n-dopant in 4H-SiC is N, as it has the lowest ionization energy (see section 1.5.1). As discussed, not all the implanted concentration of N atoms form the N_C donors but some of them are deactivated by forming other defect complexes that persist high temperature anneals [62, 63, 64]. Theoretical calculations have tried to find possible reactions paths with intrinsic defects in order to find the defects responsible for the deactivation [173, 174, 175, 176]. However, no convincing experimental identification has been achieved, even though a defect assigned to a deep level N complex was observed by EDMR [7]. In the following the N-related centers so far identified using EPR and related methods are discussed.

The nitrogen donor (N_C)

The shallow N_C center in SiC has been studied extensively with EPR and its first observations dates back to 1961 by H.H. Woodbury and G.W. Ludwig [58]. In 4H-SiC the N_C is characterized by a strong site dependence especially observed in the HF interaction. While the N_C (k) shows a pronounced HF splitting of $a \approx 18\,\mathrm{G}$ due to the spin $I = 1$ N atom, the splitting for the N_C (h) is very small [59, 61]. The former has the g-factors $g_{c\|B} = 2.0043$ and $g_{c\perp B} = 2.0013$, and the latter has $g_{c\|B} = 2.0063$ and $g_{c\perp B} = 2.0006$ [60]. EPR spectra of N-implanted 4H-SiC samples are usually dominated by these two defects. However, the resonance spectrum of a defect with smaller intensity was often observed along with the N_C donors, as discussed in the following.

The N_C donor pair (N_x)

The N_C donor pair defect (N_x) defect has been observed in heavily N-implanted 4H-SiC and was assigned to a closely located pair of N_C donors [60, 175, 177]. Both its g-factors and HF splittings are somewhat inbetween those of the N_C (k) and N_C (h) [60]. Further investigations have proven this model by confirming the spin $S = 1$ nature of this defect with a very small

zero-field splitting [178]. However, this identification excludes the N_x center from being a candidate for the N dopant deactivation, as it is only composed of N_C donors.

The N_C coupled to a V_{Si} (N_CV_{Si})

The only experimentally observed and identified N-containing complex in 4H-SiC other than the N_C donors is the N_C coupled to a V_{Si} (N_CV_{Si}) in the negative charge state [147]. The N_CV_{Si} has been suggested as an important defect forming in N-implanted SiC [143, 173], and several experimental studies on 6H-SiC have made assignments to the N_CV_{Si} [179, 180, 181, 182]. In a recent work by H.J. von Bardeleben et al. an unambiguous identification was achieved by comparing experimentally oberved EPR spectra with theoretical calculations [147]. The $N_CV_{Si}{}^-$ is a $S = 1$ defect characterized by a large zero-field splitting of $\approx 900\,\mathrm{G}$. The HF splitting due to the N atom is only $a_N \approx 0.4\,\mathrm{G}$ but resolvable, which was the basis of the identification of this defect [147]. The HF splitting of the Si atoms is $a_{Si} \approx 4\,\mathrm{G}$ and that of the C atoms is $a_C \approx 19 - 46\,\mathrm{G}$. Like other defects with a high spin ground state the $N_CV_{Si}{}^-$ is in the current focus for quantum computing applications [143, 145, 147].

1.7.3 Interface Defects

As discussed above, many defects in bulk 4H-SiC have been identified. However, there is still little known about the defects that limit the performance of 4H-SiC MOSFETs. The most important defects for Si-SiO_2 interfaces have already been identified decades ago [108, 183, 184]. For the SiC-SiO_2 system this is not the case and research is still trying to identify the most important interface defects that limit the performance of MOSFETs. A summary of observed defects and the suggested models can be found in [185]. In the following some of the defect models suggested from EPR and EDMR experiments are discussed. Note that the present work was only focused on the Si-face, i.e. the (0001) interface.

Carbon dangling bonds (P_{bC} centers)

Several EPR and EDMR studies have suggested P_{bC} centers at the interface [110, 111, 112, 113, 186, 187, 188]. EPR studies conducted on oxidized porous SiC show the signature of differently oriented defects identified as P_{bC} centers [110, 187]. The different orientations are likely a result of the differently oriented SiC-SiO_2 interfaces in the porous crystal and it is doubtful whether all of them would be observable on the (0001) face. An EDMR study on SiC MOSFETs found a defect with an anisotropic g-factor of $g_{c\|B} = 2.0026$ and $g_{c\perp B} = 2.0010$ which was interpreted as a C dangling bond aligned along the c-axis on the basis that $g_{B\|c}$ is closer to the free electron $g_e = 2.0023$ [111]. However, considering the results in [110, 187] it could also be interpreted as the overlapping and unresolved spectra of the C dangling bonds that are *not aligned* with the c-axis, which are more likely present on the Si-face. Further investigations of porous SiC annealed in H-containing atmosphere resulted in a significant reduction of the P_{bC} centers [186]. For the D_{it} in MOSFETs only little passivation effects are observed [68]. Therefore, while the existence of P_{bC} centers is evident [110, 187], their role in the degradation of MOSFETs remains unclear. A recent work by M.A. Anders et al. concluded that dangling bonds play a minor role in SiC MOSFETs [189].

The silicon vacancy (V_{Si})

The V_{Si} has been suggested as a dominant defect at the SiC-SiO_2 interface [190, 191], since it has also been identified as one of the dominant defects in bulk SiC [136]. Extensive research

by the group of P.M. Lenahan over the years has often revealed similar defect spectra in SiC MOSFETs obtained by EDMR measurements [190, 191, 192, 193]. All these defect spectra were characterized by an isotropic g-factor of $g \approx 2.0027$ and some HF lines which broadly matched with a tentative V_{Si} model. An identification of the V_{Si} defect was ultimately achieved by C.J. Cochrane et al. by measuring the EDMR signal under "fast passage" conditions [194, 195]. The observed lines could be well explained by the known model of the ${V_{Si}}^-$ [163, 194]. However, while this study is very convincing, the ${V_{Si}}^-$ does not satisfactory explain the spectra observed in a conventional EDMR experiment (without "fast passage"), as the HF constants and peak intensities are apparently different in those spectra [190, 191, 193]. Therefore, some doubt remains, whether the V_{Si} vacancy is really the dominating recombination center in those studies and some follow-up work [196, 197, 198, 199]. Some studies observed the same spectrum in n-channel MOSFETs by measuring EDMR using the bipolar amplification effect (BAE) technique [196, 197]. This technique is particularly sensitive on defects at the interface, which is in this case p-type material. Theoretical work has shown that the V_{Si} is a metastable defect in p-type SiC [167] which raises further doubt whether it would persist after the high temperature anneals usually applied in the manufacturing process of SiC MOSFETs. In summary, while the V_{Si} has shown to be present in SiC MOSFETs [194], it is likely not the only important defect.

1.8 Summary

The benefits of SiC for power semiconductor applications have led to extensive research in the past decades. Many challenges in the manufacturing have been overcome and SiC has reached a quality that allows for various types of devices to enter the market [14, 15, 16]. However, there are still major improvements to be made, particularly with regard to SiC MOSFETs. Due to the poor quality of SiC-SiO_2 interface MOSFETs are still facing channel mobilities well below the bulk mobility along with reliability issues. Despite being extensively studied and characterized, the SiC-SiO_2 interface is still poorly understood. Many of the referenced studies aiming to reveal the structure of the interface (i.e. by TEM) contradict each other in different points. There is not a real consensus on either the interface structure or the reason for the observed D_{it}. However, there is a general agreement that POAs in NO can significantly improve the channel mobility and reduce the D_{it} [70, 75]. This process has resulted in MOSFETs with acceptable channel mobility entering the market [16]. Nonetheless, there is still a lot of room for further improvements for both performance and reliability [72]. While existing processes are optimized and new processes are tried out, the key remains to reveal the structure of the interface and the D_{it}. Several point defects in the bulk have been identified using EPR. However, the defects at the SiC-SiO_2 interface are less well understood. While the defects observed by EPR and EDMR have been linked to P_{bC} centers and the V_{Si} there is not a good agreement between the different studies referenced above. An important question is how comparable the samples investigated in these studies are to each other and to state-of-the-art devices, as investigated in this work.

Chapter 2

Electrically detected magnetic resonance (EDMR)

Point defects in a wide-bandgap semiconductor like SiC usually possess several charge states in the bandgap out of which some are paramagnetic, i.e. they have a net electron spin. The interactions of the electron spin with an applied magnetic field and nearby nuclear or electron spins can be measured by EPR and give structural information on the defects. Since its development in 1945 by E. Zavoisky [200, 201], EPR has been extensively used to study and identify paramagnetic point defects in solid crystals. One major problem that conventional absorption-detected EPR faces is the detection limit of $\approx 10^{10}$ defects [202], which does not allow for the study of small samples or samples with small defect concentrations. Other methods with higher sensitivities have been developed, including EDMR [203] and optically detected magnetic resonance (ODMR) [204]. The former is in the focus of this work and can be realized in various ways [203] out of which spin dependent recombination (SDR) was used to study defects in SiC devices. The benefit of the electrical detection is the much higher sensitivity compared to absorption detected EPR [203, 205, 206]. In principle, the sensitivity of the measurement is limited by the minimum current changes that are observable with the electrical measuring instrumentation. A second benefit of EDMR comes from the fact that only paramagnetic defects that are in the pathway of the measured current are detected, while others are neglected. This allows for the study of particular regions of a fully manufactured device, e.g the SiC-SiO_2 interface of a MOSFET.

In principle, EDMR allows for the same structural information of the studied defects to be gained as with EPR. In the following the most important fundamentals of EPR and SDR are introduced. For a more detailed introduction into EPR the reader is referred to the referenced textbooks [134, 202, 207].

2.1 Spins in a magnetic field

Electrons and atomic nuclei are particles that possess the quantum mechanical property of spin. The following considerations treat the interactions between these particles and magnetic fields. Electrons are spin $S = 1/2$ particles and the spin angular momentum $\mathbf{S}$ gives rise to a magnetic moment $\boldsymbol{\mu}_S$ defined by the equation

$$\boldsymbol{\mu}_S = -g_\mathrm{e}\mu_\mathrm{B}\mathbf{S} \tag{11}$$

where g_e is the g-factor of the free electron ($g_e = 2.00232$) and μ_B is the Bohr magneton. An electron that is located in an orbital also possesses an orbital angular momentum $\mathbf{L}$ giving rise to the orbital magnetic moment $\boldsymbol{\mu}_L$ defined by

$$\boldsymbol{\mu}_L = -\mu_\mathrm{B}\mathbf{L}. \tag{12}$$

Nuclei are particles with spin I, which depends on the number of protons and neutrons in a particular nucleus [134]. In analogy to equation (11) the nuclear spin angular momentum $\mathbf{I}$ results in a magnetic moment $\boldsymbol{\mu}_I$ which is defined by

$$\boldsymbol{\mu}_I = g_\mathrm{N}\mu_\mathrm{N}\mathbf{I} \tag{13}$$

where g_N is the nuclear g-factor which depends on the number of protons and neutrons in a particular nucleus and μ_N is the nuclear magneton. The interactions between the magnetic moments defined in equations (11), (12), and (13) with an external magnetic field and with each other can be described by the Hamiltonian

$$\mathcal{H} = \mathcal{H}_\mathrm{Z,e} + \mathcal{H}_\mathrm{Z,N} + \mathcal{H}_\mathrm{HF} + \mathcal{H}_\mathrm{ee} \tag{14}$$

with the contributions of the electron Zeeman interaction $\mathcal{H}_\mathrm{Z,e}$, the nuclear Zeeman interaction $\mathcal{H}_\mathrm{Z,N}$, the HF interaction $\mathcal{H}_\mathrm{HF}$ and the electron-electron interaction $\mathcal{H}_\mathrm{ee}$. In the following the individual contributions to $\mathcal{H}$ are further discussed. Note that $\mathcal{H}_\mathrm{Z,N}$ is left out, as it has little relevance for the experiments described in this work.

2.1.1 Electron Zeeman interaction

The electron Zeeman interaction is the interaction of the electron magnetic moment $\boldsymbol{\mu}_\mathrm{e} = \boldsymbol{\mu}_S + \boldsymbol{\mu}_L$ with an applied magnetic field $\mathbf{B}$ defined by the equation

$$\mathcal{H}_\mathrm{Z,e} = -\boldsymbol{\mu}_\mathrm{e} \cdot \mathbf{B}. \tag{15}$$

In solids the orbital angular momentum contribution $\boldsymbol{\mu}_L$ is often strongly quenched and the magnetic moment $\boldsymbol{\mu}_\mathrm{e}$ is mostly dominated by the spin contribution $\boldsymbol{\mu}_S$ [208]. However, due to the effect of spin-orbit coupling ($\mathcal{H}_\mathrm{LS} = \lambda\mathbf{L} \cdot \mathbf{S}$, with spin-orbit coupling parameter λ) some contribution of the orbital angular momentum perturbs the local magnetic field interacting with the electron [134]. Including the contribution of spin-orbit coupling $\mathcal{H}_\mathrm{Z,e}$ can be written as

$$\mathcal{H}_\mathrm{Z,e} = \mu_\mathrm{B}\mathbf{B} \cdot \mathbf{g} \cdot \mathbf{S}. \tag{16}$$

where $\mathbf{g}$ is a 3×3 matrix that describes the angular dependence of the Zeeman interaction with respect to the applied magnetic field. The matrix can be diagonalized leading to the diagonal elements g_{xx}, g_{yy}, and g_{zz}, as also discussed in section 4.5 [134]. The symmetry of the Zeeman interaction is reflected in these g-factors, which in general differ from each other ($g_{xx} \neq g_{yy} \neq g_{zz}$), but are close to g_e [134]. For the isotropic case the g-factor is independent of the direction of the applied magnetic field and thus $g_{xx} = g_{yy} = g_{zz}$. Often axial symmetry is observed leading to $g_{xx} = g_{yy} = g_\perp$ and $g_{zz} = g_\parallel$. As the g-matrix depends on the spin-orbit coupling (i.e. the shape of the electron orbital), it is somewhat characteristic for a given defect and can be helpful to identify the structure of an unknown defect. However, more information on the nearby atomic species is contained within the HF interaction term $\mathcal{H}_\mathrm{HF}$, as follows.

2.1.2 Hyperfine (HF) interaction

HF interaction occurs when the magnetic moment of an unpaired electron interacts with the magnetic moments of surrounding nuclear spins $I > 0$. The Hamiltonian for HF interaction between an electron and a nucleus is defined by

$$\mathcal{H}_{\mathrm{HF}} = \mathbf{S} \cdot \mathbf{A} \cdot \mathbf{I} \tag{17}$$

where $\mathbf{A}$ is a 3×3 matrix called the HF coupling parameter matrix. $\mathbf{A}$ describes the magnitude and angular dependence of the HF coupling and can also be written in the form

$$\mathbf{A} = A_{\mathrm{iso}} \mathbb{1}_3 + \mathbf{T} \tag{18}$$

where A_{iso} is the isotropic HF coupling constant, $\mathbb{1}_3$ is the 3×3 unity matrix, and $\mathbf{T}$ is a 3×3 matrix describing the anisotropy of the HF interaction. A_{iso} is also called Fermi contact term and is given by the equation

$$A_{\mathrm{iso}} = \frac{2}{3} \mu_0 g \mu_{\mathrm{B}} g_{\mathrm{N}} \mu_{\mathrm{N}} \left| \psi_{\mathrm{e}} \left(0\right) \right|^2 \tag{19}$$

where μ_0 is the vacuum permeability and $\left|\psi_{\mathrm{e}}\left(0\right)\right|^2$ is the density of the electron wave function ψ_{e} at the site of the nucleus which is considered to be at the origin [134]. A_{iso} is only non-zero if the electron has a finite probability to be found at the nuclear site. The higher the electron density is at the nuclear site, the higher is the isotropic HF coupling. Only electron orbitals with a certain s-character give rise to the isotropic HF coupling. The p-, d-, and f- character of the electron wave function only gives rise to the anisotropic HF coupling described by the anisotropic HF coupling parameter matrix $\mathbf{T}$. The anisotropic HF coupling has its origin in the dipole-dipole interaction between the electron and the nucleus and is given by the equation

$$\mathbf{T} = g \mu_{\mathrm{B}} g_{\mathrm{N}} \mu_{\mathrm{N}} \left\langle \frac{3 r_i r_j - \delta_{ij} r^2}{r^5} \right\rangle \tag{20}$$

where r_i and r_j are the coordinates of the electron, r is the distance to the nucleus located at the origin, and the brackets indicate an integration over all electron positions in the orbital [134, 208].

Since an electron is usually distributed over several atoms in a solid crystal, equation (17) becomes a sum over all nuclei k interacting with the electron and their respective $\mathbf{A}_k$ and $\mathbf{I}_k$:

$$\mathcal{H}_{\mathrm{HF}} = \sum_k \mathbf{S} \cdot \mathbf{A}_k \cdot \mathbf{I}_k . \tag{21}$$

The HF interaction is directly dependent on the nuclear spins closest to an unpaired electron and therefore contains chemical information of the defect, i.e. the atoms residing at or close to the defect. Note that only nuclei with non-zero nuclear spin result in a non-zero HF interaction. Table 2.1 shows the paramagnetic isotopes of elements relevant for the samples described in this work and their respective natural abundances $\mathcal{N}$. More details on how the HF interactions contribute to an experimental spectrum are found in section 4.6.

2.1.3 Electron-electron interaction

In a paramagnetic system where two (or more) electron magnetic moments interact with each other the electron-electron coupling term becomes important. This can be the case for certain charge states of a given defect in the bandgap of a semiconductor. In the following the case

Table 2.1: Natural abundances $\mathcal{N}$ and nuclear spin I of the paramagnetic isotopes of the most important elements present in SiC devices [134].

Isotope	$\mathcal{N}$ (%)	I
^{1}H	≈ 100	1/2
^{13}C	1.11	1/2
^{14}N	≈ 100	1
^{27}Al	100	5/2
^{29}Si	4.67	1/2

of two interacting electrons is considered as an example. The total spin for two electrons can either be $S = S_1 + S_2 = 0$ resulting in a diamagnetic singlet state with or $S = 1$ resulting in a paramagnetic triplet state. The electron-electron coupling Hamiltonian $\mathcal{H}_{\text{ee}}$ contains two terms

$$\mathcal{H}_{\text{ee}} = \mathcal{H}_{\text{dd}} + \mathcal{H}_{\text{ex}} \tag{22}$$

where $\mathcal{H}_{\text{dd}}$ is the electron dipole-dipole interaction Hamiltonian and $\mathcal{H}_{\text{ex}}$ is the electron exchange interaction Hamiltonian. The former is only relevant for the triplet state and the latter describes the energy difference between the singlet and the triplet state (and which of them is lower in energy) [134]. In the following only $\mathcal{H}_{\text{dd}}$ is considered.

Electron dipole-dipole interaction

Similar to the HF interaction an unpaired electron magnetic moment can couple with the electron magnetic moment of another electron. The electron dipole-dipole interaction Hamiltonian $\mathcal{H}_{\text{dd}}$ is given by

$$\mathcal{H}_{\text{dd}} = \mathbf{S} \cdot \mathbf{D} \cdot \mathbf{S} \tag{23}$$

where $\mathbf{S}$ is the total spin operator $\mathbf{S} = \mathbf{S}_1 + \mathbf{S}_2$ and $\mathbf{D}$ is the electronic quadrupole parameter matrix. $\mathbf{D}$ is given by

$$\mathbf{D} = \frac{\mu_0}{8\pi} (g\mu_{\text{B}})^2 \left\langle \frac{3r_i r_j - \delta_{ij} r^2}{r^5} \right\rangle \tag{24}$$

which is in analogy to equation (20) now with one electron placed in the origin and integrated over all positions of the second electron. $\mathcal{H}_{\text{dd}}$ describes the energy splitting between the triplet states and is zero for the singlet state. As this interaction term describes the energy difference between the $m_S = 0$ and the $m_S = \pm 1$ states of the triplet at zero magnetic field, it is commonly called zero-field splitting [134].

2.2 Electron paramagnetic resonance (EPR)

The aim of EPR spectroscopy is to identify the structure of the studied paramagnetic defects by experimentally determining the interaction terms described above. In principle all of the above-mentioned interactions are present, but usually some terms are less important for a specific system. The basic principle of the measurement is to apply a magnetic field on the sample under study and induce transitions between the magnetically shifted energy levels by shining in photons. Resonance is observed when the photon energy matches the energy gap

between the energy levels of an allowed transition. In the following all considerations are made on defects in a crystalline environment.

The most simple system to study is an electron not interacting with any other spins in which case the Hamiltonian only contains the electron Zeeman interaction term $\mathcal{H}_{\mathrm{Z,e}}$. The electron has two possible spin states expressed by the electron magnetic spin quantum number $m_S = \pm 1/2$ which is the projection of the electron spin to the direction of the applied magnetic field B (conventionally chosen as z). The energy difference ΔE between the two spin states follows from equation (16) resulting in the resonance condition for a transition to be induced by a photon

$$\Delta E = E(m_S = +1/2) - E(m_S = -1/2) = \mu_{\mathrm{B}} g B = h\nu \tag{25}$$

where g is the g-factor for the particular orientation between the defect and the applied magnetic field, h is Planck's constant and ν is the photon frequency, which is often in the microwave regime. When the resonance condition is fulfilled the spin system will take up energy by absorbing photons and flipping the electron spin. Conventionally, the experiments are carried out with a constant microwave frequency while the magnetic field is swept slowly through the resonance field and the absorption of the photons is measured. Under resonance an increased absorption is detected and g can be determined from equation (25). By repeating the measurement with different orientations between the crystal and the magnetic field the matrix elements of the g-matrix can be determined (see section 4.5), revealing some valuable information about the defect's symmetry. While the g-matrix can be compared to literature values and may be used to identify an unknown defect, a more powerful means is the study of the HF structure.

The HF structure is directly dependent on the chemical environment of a defect electron, namely the nearby paramagnetic nuclei giving rise to the HF interaction. The magnetic moment of the nuclei may increase or decrease the magnetic field at the position of the electron. When a defect electron interacts with paramagnetic nuclei in its vicinity through the HF interaction the resonance condition becomes

$$h\nu = g\mu_B \left(B_{\mathrm{res}} + \sum_k a_k m_{I,k} \right) \tag{26}$$

where B_{res} is the resonance magnetic field, a_k is the HF splitting constant of the k-th nucleus ($a_k = A_k/(g\mu_{\mathrm{B}})$ for $g \approx g_e$) and $m_{I,k}$ is the magnetic nuclear spin quantum number of the k-th nucleus (i.e. the projection of I in the z-direction). Rewriting the equation yields

$$B_{\mathrm{res}} = \frac{h\nu}{g\mu_B} - \sum_k a_k m_{I,k} = B_0 - \sum_k a_k m_{I,k} \tag{27}$$

where B_0 is the resonance magnetic field without HF interaction, i.e. the center of the spectrum. Considering the simple case of an electron interacting with only one nucleus with $I = 1/2$ there are two possible spin states for the nucleus $m_I = \pm 1/2$ each resulting in a different resonance field. Note that it is still the transition of the electron spin between its two levels $m_S = \pm 1/2$ that is measured. The nuclear spin state is assumed not to change as the electron transitions happen much faster [134]. For a large ensemble of the same spin system 50 % of the nuclei will be in the $m_I = +1/2$ and 50 % in the $m_I = -1/2$ state resulting in a spectrum containing two lines of equal intensity. Note that this only holds true due to the fact that the nuclear Zeeman interaction is very small, which results in practically equally occupied nuclear spin states m_I at the temperatures and magnetic fields considered. For an $I = 1$ nucleus there will be three peaks of equal intensity due to the three possible spin states $m_I = -1, 0, \text{and} + 1$. For any

nucleus there is a total of $2I + 1$ lines due to its HF interaction, as this is the number of its possible states of m_I.

In a semiconductor the electron wave function is usually distributed over several neighboring atoms which all add to the sum in equation 27, given they have a spin $I > 0$. The total number of lines in the spectrum is the product of the number of possible lines due to each of the individual nuclei with $I > 0$. This results in spectra with many HF lines that are often close together and remain unresolved. Another level of complexity is added by the fact that some atoms are naturally abundant in different isotopes with different nuclear spin which is reflected in the relative intensity of the lines. All this makes the direct interpretation of the observed HF spectrum difficult, especially when the individual lines are unresolved. As the interpretation can be very ambiguous, EPR and EDMR experiments are often paired with theoretical calculations of candidate defects and their HF parameters. A more detailed discussion of how a HF spectrum can be accurately generated from theoretically calculated HF parameters is described in section 4.6.

The electron dipole-dipole interaction in $S > 1/2$ electron systems results in a zero-field splitting of the observed lines. The number of lines depends on the total spin $S = \sum_i S_i$ while the magnitude of the splitting depends on the coupling parameter D. As discussed in section 1.7.1, several defects in SiC show a pronounced zero-field splitting [147, 148, 164]. A special case is the V_{Si}^- which exists in two different conformations one of which has a pronounced zero-field splitting while for the other it vanishes [136, 164]. It is emphasized at this point that in none of the experiments described in this work any lines could clearly be associated with zero-field splitting and all interpretations only considered the HF interaction.

2.3 Spin dependent recombination (SDR)

The conventional approach taken in EPR is to detect the absorption of the microwave photons. However, this method faces a detection limit of 10^{10} total spins which requires large samples and/or defect concentrations. In semiconductors a number of alternative techniques exist for obtaining EPR through observables other than just the absorbed microwave power. The most common ones can be grouped in EDMR where the observable is an electrical signal, usually a current, and ODMR where the observable is the photoluminescence of the sample [203, 204, 209]. The former group summarizes different spin dependent processes that may influence the conductivity of the sample, such as spin dependent scattering, spin dependent tunneling, and SDR [203]. The experimental detection is realized in different ways which include the detection of the current in a biased device [210], the detection of a photocurrent [205], and the microwave contact-less photoconductive resonance method [211]. This work focuses on the detection of biased SDR on fully manufactured SiC devices. This method has been demonstrated to be particularly sensitive when studying defects at the SiC-SiO_2 interface of SiC MOSFETs [197]. The benefits of this method are that it does not require elaborate sample preparation as the biasing is used to selectively probe the device region of interest and that it is applicable on relatively low defect concentrations. In the following the principles of SDR are discussed.

The effect of spin dependent recombination was first described by the work of D.J. Lépine [205]. He discovered that by monitoring the photocurrent in Si devices in an EPR setup, one can measure the EPR spectrum with a high relative signal and a high signal-to-noise ratio. He explained the phenomenon by a spin-dependent component in the photocurrent, i.e. the recombination current, which changes as paramagnetic recombination centers become resonant. This model was based on Shockley-Read-Hall recombination through one paramagnetic state in the bandgap [106, 107]. However, the proposed quantitative model that suggested a dependence

on the polarization of the paramagnetic defect was not accurate and described a smaller relative current change than observed [205].

A more accurate model was proposed by D. Kaplan et al. which resulted in a more accurate description of the observed effect [206]. This model referred to as the spin-pair model considers an electron and a hole captured in two different paramagnetic states in the bandgap, as shown in Figure 2.1. Note that a captured hole is equivalent to an orbital containing one electron, i.e. a space that can be filled by another electron. The electron and hole have to be in proximity to interact with each other and are considered as the spin-pair. The recombination can be thought as a process where the electron fills the open space in the other level after which both levels can again capture an electron or a hole, respectively. Figure 2.1 shows a schematic of the two occupied states in the bandgap with the arrows indicating their spin. The total spin of the pair can be $S = 0$ (singlet) or $S = 1$ (triplet) and is crucial for the recombination.

After the recombination of the electron and the hole the total spin is zero. Due to the conservation of the spin this means that only the singlet state of the spin-pair allows for recombination. This selection rule results in much shorter recombination times of the singlets with respect to the triplets [206]. This results in a higher population of triplets with respect to singlets in steady-state conditions, meaning that more than 3/4 of the pairs will be in the triplet state and less than 1/4 in the singlet state. When resonance occurs triplets are converted into singlets (and vice versa) by flipping the paramagnetic spin of either the hole or electron that becomes resonant. This increases the population of singlets (up to 1/4 under full saturation) and allows for more pairs to recombine.

The increased recombination rate under resonance can be detected as a current change, which is the observable in SDR to study the EPR parameters of the resonant paramagnetic state. In principle both paramagnetic states forming the pair can become resonant and both EPR spectra can in principle be detected [203, 212, 213]. However, in most of the experiments described in this work only one dominant resonance feature was observed.

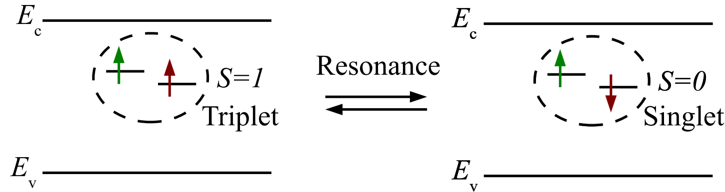

Figure 2.1: The spin-pair model suggests that an electron (green arrow) and a hole (red arrow) should be regarded in terms of their total spin S prior to recombination [206]. For $S = 1$ (triplet) recombination is forbidden, while for $S = 0$ (singlet) it is allowed.

Part II

Methodology

Chapter 3

Electrical characterization

This study is focused on understanding the microscopic defects that limit the electrical performance and reliability of SiC devices. Therefore, it is crucial to compare the studied devices not only in terms of their EDMR response, but also in terms of their electrical performance. In the following a brief summary is given on how electrical parameters like the low field mobility μ_{LF}, the threshold voltage V_{th}, and the density of interface defects D_{it} were extracted. The equipment used for the electrical measurements was an *Agilent B1500A* parameter analyzer, a *Keithley 2636A* sourcemeter, a *Jäger ADwin Pro II* digital-to-analog converter (DAC)-analog-to-digital converter (ADC), and a *Stanford Research SR570* current amplifier.

3.1 Transfer characteristics

The transfer characteristics are the measurement of the dependence of the drain current I_{d} on the gate voltage V_{g} for a given drain voltage V_{d} [76, 77]. Figure 3.1a shows the transfer characteristics of a SiC MOSFET. As discussed in section 1.6.1, this data can be used to determine μ_{LF} and V_{th} via equation 9, as suggested by G. Ghibaudo [82]. Figure 3.1b shows the data of the transfer characteristics plotted as $I_{\mathrm{d}}/\sqrt{g_{\mathrm{m}}}$ vs. V_{g} and a linear fit of the linear part of the curve. From the fitting parameters both μ_{LF} and V_{th} can easily be obtained.

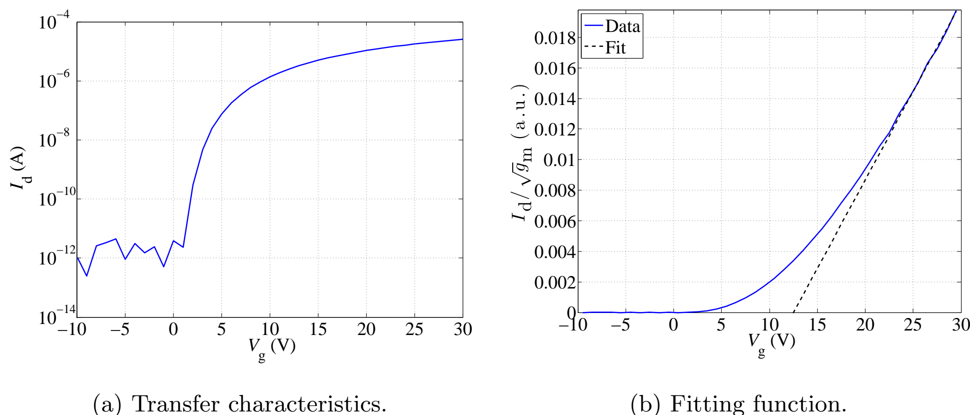

(a) Transfer characteristics.

(b) Fitting function.

Figure 3.1: Recorded transfer characteristics and fitting function to determine μ_{LF} and V_{th}.

3.2 Charge pumping

The charge pumping technique is a reliable means for studying the D_{it} at the SiC-SiO$_2$ interface of SiC MOSFETs [100]. The technique was introduced in the study of J.S. Brugler and P.G.A. Jespers [214] and was later more thoroughly described by G. Groeseneken et al. [215]. The benefit of charge pumping is that it can be used to characterize the D_{it} in fully processed MOSFETs, rather than MOS capacitors.

The principle of charge pumping is to apply voltage pulses to the gate of a MOSFET while monitoring the current between the source/drain and body contacts. Figure 3.2a shows a schematic of the biasing scheme for an n-channel MOSFET and the applied gate pulses. The gate voltage is pulsed between a base voltage V_{low} and a high voltage V_{high}. When V_{low} is in accumulation holes are attracted to the SiC-SiO$_2$ interface. When V_{high} is in inversion the holes are pushed back to the body and electrons are attracted to the interface. If any of those carriers are trapped at the interface during the pulse plateaus and t_{rise} and t_{fall} are sufficiently short (i.e. shorter than the emission time of the trapped carriers), they may recombine with the arriving carriers of the opposite charge on the next plateau. This gives rise to the measured charge pumping current I_{cp} between the source/drain and the body contacts.

In the present work only trapezoidal pulses of equal rise and fall times $t_{\mathrm{rise}} = t_{\mathrm{fall}}$ as well as equal duty times $t_{\mathrm{low}} = t_{\mathrm{high}}$ were used. The mode for the measurements was constant base charge pumping where V_{low} is kept constant and V_{high} is increased while the charge pumping current I_{cp} is monitored. A measurement series of constant base charge pumping curves with different charge pumping frequencies f_{cp} is shown in Figure 3.2b. The base level is usually chosen far in accumulation where only holes are present at the SiC-SiO$_2$ interface. As the high level of the pulses increases across the bandgap more and more electrons are present at the high pulse until ultimately deep inversion is reached and the charge pumping current saturates. The maximum charge pumping current I_{cp} is proportional to the D_{it} via the equation

$$I_{\mathrm{cp}} = q_{\mathrm{e}} f_{\mathrm{cp}} A_{\mathrm{g}} \Delta E_{\mathrm{cp}} D_{\mathrm{it}} \tag{28}$$

where f_{cp} is the charge pumping frequency, A_{g} is the gate area and ΔE_{cp} is the energy window probed by the charge pumping measurement. Note that the D_{it} is averaged over an energy window of $\Delta E_{\mathrm{cp}} \approx 2.9\,\mathrm{eV}$ symmetrically around midgap for the studied MOSFETs [100].

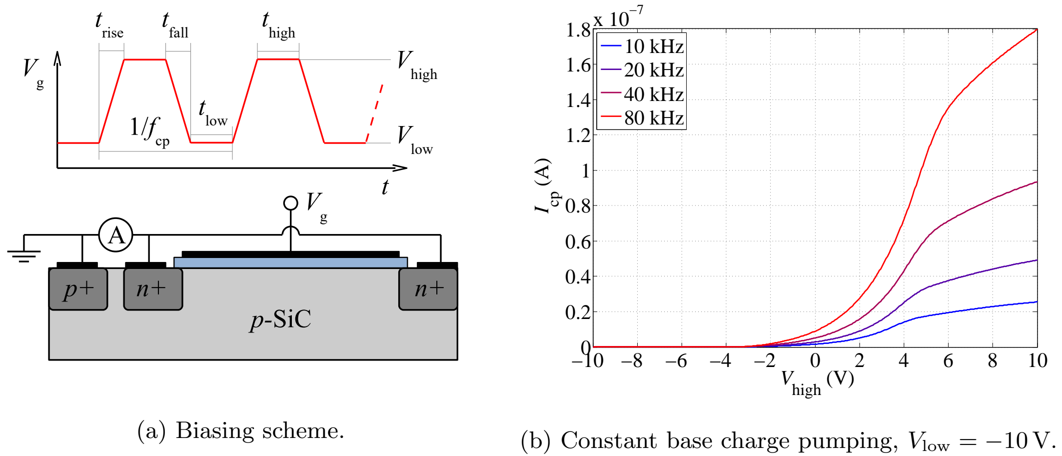

(a) Biasing scheme.

(b) Constant base charge pumping, $V_{\mathrm{low}} = -10\,\mathrm{V}$.

Figure 3.2: Charge pumping on a SiC n-channel MOSFET.

Chapter 4

EDMR

This section gives a brief introduction in the experimental setup and methods used for EDMR measurements and their interpretation discussed in chapters 6 to 8. The equipment used for this work as well as the routine of an EDMR measurement is described followed by an introduction of the biasing scheme used for EDMR on MOSFETs. Ultimately, the methods used for extracting and interpreting g-factors and HF parameters is given. The latter was based on simulations for which a computer program was written, see also appendix B.

4.1 Experimental setup

The experimental setup was built around a *Varian E9* X-band EPR spectrometer and is mostly identical to the one described in the reference [1]. However, several adaptions have been made and a number of measurement units from the original setup have been replaced by more modern ones. The setup allows for both EPR and EDMR measurements at room temperature. Initially, the EDMR of the studied semiconductor device and the EPR of a known standard were recorded simultaneously in order to correct for instabilities of the magnetic field during measurements, see reference [216]. However, by the use of more stable current sources and better monitoring of the magnetic field the instabilities were no longer an issue [1]. Further adaptions to the setup have recently been performed by R. Meszaros in order to allow for EDMR at cryogenic temperatures [217].

Figure 4.1 shows a schematic of the experimental setup used for the EDMR measurements. Every measurement is controlled by a computer which is linked to the measurement units via different interfaces and a LABVIEW program [218]. The program is used for putting in the experimental parameters such as scan speed and range of the magnetic field scan, starting and stopping a measurement, and acquiring and saving the measured data. The studied sample is located in a position of minimal electric field in a TE_{103} cavity labeled C. Microwaves of constant frequency are generated by an *HP 8672A* synthesizer and amplified by an *HP 8348A* microwave amplifier. This setup allows for power levels of $\approx 1\,W$ in continuous wave mode. The microwaves are fed into a system of waveguides labeled W and coupled into the cavity via an iris screw. Both the screw position and the microwave frequency are set for an optimized coupling of the microwaves into the cavity. The signal reflected from the cavity can be picked up by a detector diode and is used for EPR measurements. The cavity is located in the center of the pole shoes of an electromagnet where the magnetic field is the most homogeneous. There are three sets of coils contributing to the magnetic field at the position of the cavity. One set of coils labeled B1 is used to generate a static magnetic field and is powered by a *TTi QPX1200*

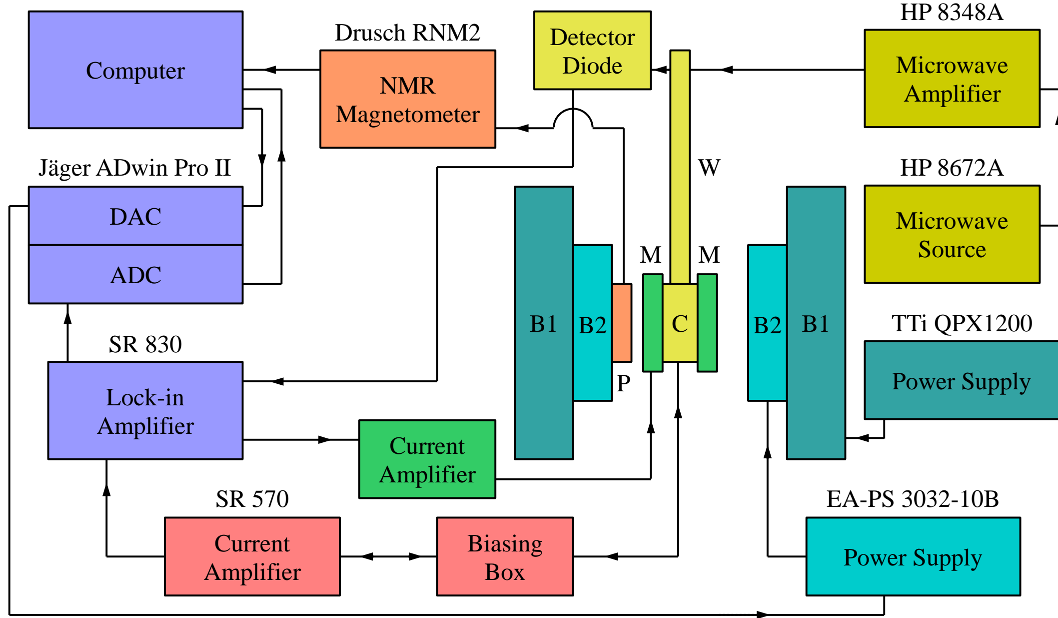

Figure 4.1: Schematic of the experimental setup used for EDMR and EPR.

power supply. This magnetic field is set below the resonance field of the sample. A second set of coils labeled B2 is used for the quasi-static scan of the magnetic field through the resonance field. This set of coils is powered by an *EA-PS 3032-10B* power supply and allows for magnetic field scans of up to $\approx 500\,\mathrm{G}$. The current output of the *EA-PS 3032-10B* can be controlled via a voltage input. This is accomplished by the output of the DAC of a *Jäger ADwin Pro II* eight channel ADC-DAC which can be programmed by the computer. The total magnetic field produced by the coils B1 and B2 is monitored by a *Drusch RMN2* nuclear magnetic resonance (NMR) magnetometer. This device measures the resonance of a known NMR standard in a probe labeled P that is placed between the pole shoes of the electromagnet, close to the sample cavity. The *Drusch RMN2* automatically performs a frequency scan in order to obtain the resonance frequency of the NMR standard and outputs the determined magnetic field. The third set of coils labeled M is used for the modulation of the magnetic field. This set of coils is directly attached to the cavity using a Helmholtz configuration and does not influence the NMR standard of the *Drusch RMN2*. A sine signal is output by a *Stanford Research SR830* lock-in amplifier and is amplified by a current amplifier in order to drive a current through the modulation coils. This setup allows for modulation amplitudes of up to $\approx 20\,\mathrm{G}$ and modulation frequencies of up to $\approx 10\,\mathrm{kHz}$. For EDMR measurements a *Stanford Research SR570* current amplifier is used. The *Stanford Research SR570* allows for biasing of the current input pin and includes the possibility for a current offset as well as filters. For devices that require several contacts to be biased, e.g. MOSFETs, a custom built biasing box was used. This box can be connected to the $-12\,\mathrm{V}$, $0\,\mathrm{V}$ and $+12\,\mathrm{V}$ outputs of the *Stanford Research SR570* and uses voltage dividers in order to obtain the desired biasing voltages which can be connected to the different contacts of the sample. The measured current is amplified by the *Stanford Research SR570* and fed to the lock-in amplifier. The final measurement signal that is output by the lock-in amplifier is then passed on to the computer via the ADC of the *Jäger ADwin Pro II*.

4.2 Description of an EDMR measurement

Each sample described in this thesis was extensively characterized by electrical measurements and EDMR in order to find the optimal experimental conditions for a narrow linewidth and a high signal-to-noise ratio. For this, the sample was biased by predetermined basing conditions where a maximum EDMR signal is to be expected. Then the EDMR peak was searched for by measuring with a high modulation field and microwave power, both of which maximizes the signal amplitude. Once a resonance peak was found, the biasing conditions were changed in order to optimize for a high relative signal and a high signal-to-noise ratio. Subsequently, the modulation amplitude and microwave power were adjusted to find an optimum between linewidth and signal-to-noise ratio. Once these parameters were determined a series of measurements was performed by recording the resonance spectrum multiple times. By averaging multiple scans a higher signal-to-noise ratio is obtainable, as any random noise is averaged out.

At the beginning of a measurement series the magnetic field scan was set so that the resonance is observed in the center of the scan. After allowing the magnetic field to stabilize the magnetic field scan was characterized by the *Drusch RMN2* magnetometer. Afterwards an EPR measurement of a 2,2-diphenyl-1-picrylhydrazyl (DPPH) standard with a known g-factor of $g = 2.0036$ was performed [219]. This measurement was used to correct the difference between the resonance field measured by the *Drusch RMN2* probe and the actual field inside the cavity. Then the DPPH sample was removed and the EDMR scans were started. Note, that some measurements were performed over the time of several days in which changes of the ambient temperature resulted in small changes of the magnetic field. Therefore, for each individual scan the magnetic field was monitored by the *Drusch RMN2* in order to correct for changes of the magnetic field during the long lasting experiments. Once enough scans were recorded to obtain a sufficient signal-to-noise ratio by averaging the individual scans the measurement was stopped. Subsequently a second calibration by the DPPH standard was performed for checking purposes. All post-processing of the recorded data was performed using a MATLAB script [220]. This script automatically averaged the data using a binning procedure and included the magnetic field measurements and corrections from the DPPH standard.

4.3 The gated diode SDR technique

The gated diode SDR method has often been applied for the study of defects at the SiC-SiO_2 interface of MOSFETs [190, 193, 221, 222]. Figure 4.2 shows the biasing schemes used for this technique for two different cases of fully manufactured n-channel MOSFETs.

When all contacts can individually be biased, the source and drain contacts can be shorted, see 4.2a. The resulting source/drain-to-body diode is forward biased and a current flows. This current contains contributions from the bulk as well as the interface. The former is the diode current including recombination in the space charge region of the pn-junction and the latter is the surface recombination current through defects at the SiC-SiO_2 interface. By changing the gate voltage one can find a small peak in the current, which corresponds to the maximum in the surface recombination [222]. This usually occurs when the Fermi level is close to midgap, as deep levels are the most efficient recombination centers [106, 107]. All other contributions to the current are bulk contributions that are not dependent on the gate voltage. The current through the gated diode is picked up by the *Stanford Research SR570* and used to measure the EDMR signal. When resonance occurs a current change is observed as the recombination rates through interface defects change. The problem with this technique is that the relative current change due to SDR at the interface is very small, since the bulk contribution I_{bulk} to the current is much larger than the change of the interface recombination current ΔI [197].

Fully manufactured devices often have a double-diffused MOSFET (DMOSFET) like geometry with the source and body internally shorted, as indicated in Figure 4.2b. In this case only the drain-to-body diode can be used to let a current flow through the device. While in principle the same measurement as for the other case is possible, finding the recombination peak in the current can be more challenging. The reason is that here the total current is gate-dependent due to the conductivity change of the channel between source and drain [2]. However, also for this measurement the bigger problem is the large bulk contribution I_{bulk} to the current that is independent of the recombination at the interface.

Due to the large bulk contribution to the current and the resulting small relative change of the current under resonance, the gated diode SDR technique is only applicable for relatively high defect concentrations at the SiC-SiO_2 interface. For devices that received a modern defect passivation treatment the method is simply not sensitive enough as the signal-to-noise ratio is too poor. However, an alternative biasing scheme can be used in which the large bulk current I_{bulk} is not picked up in the current measurement.

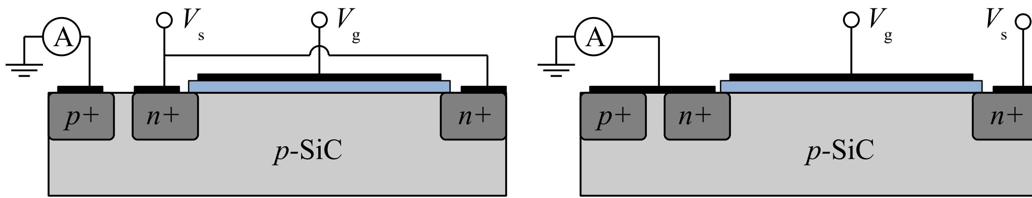

(a) Conventional gated diode biasing scheme.

(b) DMOSFET biasing scheme.

Figure 4.2: Biasing schemes for SDR measurements on n-channel MOSFETs.

4.4 The bipolar amplification effect (BAE) technique

The bipolar amplification effect (BAE) technique is described in the work by T. Aichinger and P.M. Lenahan [197]. They showed that by adapting the SDR biasing scheme one can measure the same signal with a dramatically increased signal-to-noise ratio. The key in BAE is that the high diode current is not part of the current used for the EDMR measurement. Figure 4.3 shows the biasing scheme used for BAE. The source-to-body diode is forward-biased resulting in a current I_{bulk} to flow to the body, as indicated by the solid arrows. However, the injection of carriers also results in a small diffusion current flowing to the drain, as indicated by a dashed arrow. The EDMR signal is measured at the drain contact, neglecting I_{bulk}. The current flowing along the interface is strongly dependent on the recombination at interface defects. When resonance occurs the relative change of this current is orders of magnitudes higher than the one in gated diode SDR. It has been shown that the relative signal can be as high as 1.4×10^{-2} [197]. Another benefit is that the diode can be forward biased at a higher voltage than in gated diode SDR, as the *Stanford Research SR570* does not need to be offset by such a high current value as in gated diode SDR. This further increases the signal-to-noise ratio of the measurement. Except one device with a DMOSFET-like structure all MOSFETs discussed in this work were measured by applying the BAE technique due to the much higher sensitivity the EDMR signals of. The samples were specifically designed for the application of BAE.

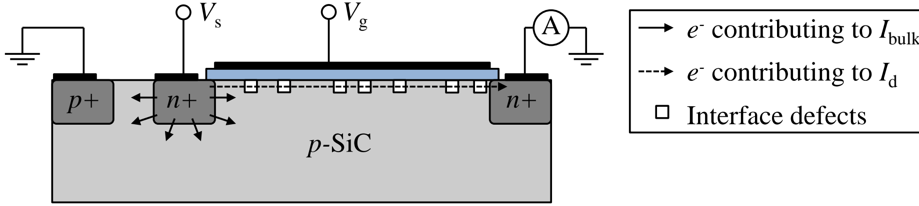

Figure 4.3: Biasing scheme for BAE measurements.

4.5 Determining the principal g-factors

As discussed in chapter 2, the g-factor contains information on a defect's symmetry and can be compared to the literature. The observed value depends on the angle between the defect's symmetry axes with respect to the applied magnetic field. The angular dependence of the measured g-factor is given by the general equation

$$\begin{aligned} g^2 = \; & (\mathbf{gg})_{xx} \sin^2\theta \cos^2\phi + 2\,(\mathbf{gg})_{xy} \sin^2\theta \cos\phi \sin\phi + (\mathbf{gg})_{yy} \sin^2\theta \sin^2\phi + \\ & 2\,(\mathbf{gg})_{xz} \cos\theta \sin\theta \cos\phi + 2\,(\mathbf{gg})_{yz} \cos\theta \sin\theta \sin\phi + (\mathbf{gg})_{zz} \cos^2\theta \end{aligned} \tag{29}$$

where $(\mathbf{gg})_{ij}$ are the matrix elements of the matrix $\mathbf{gg} = \mathbf{g} \cdot \mathbf{g}^{\mathrm{T}}$ for the different directions of the applied magnetic field x, y and z [134]. When measuring the angular dependence of g for different directions where some of the terms in eq. (25) vanish (i.e. tilting in the xy-, xz- and yz planes) the individual terms can be determined by a fit of the recorded data points. If the matrix **gg** has off-diagonal elements it means that the laboratory axes are different from the defect's symmetry axes. A diagonalization of **gg** results in the principal values g_{xx}, g_{yy}, and g_{zz} of the g-factor in the defect's symmetry axes and the respective angles between the two coordinate systems.

4.6 Simulations of EDMR spectra

The most straightforward strategy to identify an unknown defect is to compare experimental EPR or EDMR spectra with theoretical calculations, as often found in the literature [139, 147, 148]. The theoretical calculations are usually based on DFT and are in principle capable to both calculate the g-factor as well as the HF parameters [175, 223]. While both can be used to identify an unknown defect, the latter is easier to interpret as it is dependent on the chemical surrounding the unpaired electron density, i.e. the nearest atoms interacting with the unpaired electrons. As demonstrated in chapter 6, an accurate comparison of experimental spectra with the calculated HF parameters of different defect models can identify an unknown defect. In the following the principles of how a spectrum can be generated from a set of calculated HF parameters are discussed.

4.6.1 What makes up a HF spectrum?

For simplicity only the case of one type of defect with one unpaired electron is considered here. All nearby atoms with nuclear spin $I > 0$ that interact with the electron will give rise to a certain HF interaction. The HF interaction is stronger for atoms that are closer to the unpaired electron density, as discussed in section 2.1.2. The HF interaction of the k-th nucleus is observed in terms of the HF splitting constant a_k. The sum over all N nuclei and their

respective a_k and $m_{I,k}$ results in the total shift of a line with respect to the center field. At this point equation (27) is recalled as it is the basic equation defining the position of a line B_{res} with respect to the center of the spectrum found at B_0:

$$B_{\text{res}} = B_0 - \sum_{k=1}^{N} a_k m_{I,k}. \tag{30}$$

All the defects considered in this thesis are made up of Si, C, and N atoms. As shown in table 2.1 there are abundant isotopes with $I > 0$ for all of these atoms. Furthermore, each of them has a total of three possible $m_{I,i}$ values (with i=1,2,3) with a respective probability P_i due to the natural abundance of the respective isotopes, as summarized in table 4.1.

Table 4.1: Possible $m_{I,i}$ values and their respective probabilities P_i for C, Si, and N [134].

Atom	$m_{I,1}$	P_1 (%)	$m_{I,2}$	P_2 (%)	$m_{I,3}$	P_3 (%)
C	$-1/2$	0.55	0	98.90	$1/2$	0.55
Si	$-1/2$	2.33	0	95.33	$1/2$	2.33
N	-1	33.33	0	33.33	1	33.33

In a crystal with a certain concentration of the same type of defect each individual defect will be made up by the same N atoms at the same position with respect to the defect electron. However, each individual atom k will possess one of the three possible m_{I,k,i_k} states for the given element. The different isotopes will be randomly distributed over the whole crystal resulting in a total of 3^N permutations of sets of m_{I,k,i_k}. Each permutation will result in a line position according to equation (30). The total probability $\mathcal{P}$ for a given permutation of m_{I,k,i_k} values of k atoms is simply the product of the individual probabilities P_{i_k} for the atoms that interact with the defect electron:

$$\mathcal{P} = \prod_{k=1}^{N} P_{i_k}(m_{I,k,i_k}) \tag{31}$$

This probability $\mathcal{P}$ is reflected in the relative intensity that a certain permutation adds to a spectrum. More likely permutations will be present more often and consequently result in a stronger signal. The sum over all $\mathcal{P}$ of all permutations is unity.

What has been discussed so far is the position and the relative intensity of each observed line. What also must be considered are broadening mechanisms that cause the observed line profiles. Generally, Gaussian and Lorentzian line profiles are the most commonly observed profiles dependent on which broadening mechanism is dominant. The following equations are based on Lorentzian lineshapes as they were a better representation for all described experiments in this work. A Lorentzian line profile $\mathcal{L}$ due to a given permutation of nuclear spins is described by the equation

$$\mathcal{L} \propto \frac{\mathcal{P}}{\Gamma^2 + (B - B_{\text{res}})^2} \tag{32}$$

where Γ is a broadening parameter linked to the linewidth. Since in EPR and EDMR experiments lock-in-amplification is applied, the lines are observed in terms of first derivative Lorentzians described by the equation

$$\mathcal{L}' \propto \frac{-\mathcal{P}(B - B_{\text{res}})}{\left[\Gamma^2 + (B - B_{\text{res}})^2\right]^2}. \tag{33}$$

The total spectrum is obtained by summing over all permutations of the N atoms. Putting equations (30), (31), and (33) together the full spectrum is described by the equation

$$\mathcal{L}'_{\text{total}} = \sum_{i_1=1}^{3} \sum_{i_2=1}^{3} \dots \sum_{i_N=1}^{3} \left(-\prod_{k=1}^{N} P_{i_k}(m_{I,k,i_k}) \frac{B - B_0 + \sum_{k=1}^{N} a_k m_{I,k,i_k}}{\left[\Gamma^2 + \left(B - B_0 + \sum_{k=1}^{N} a_k m_{I,k,i_k}\right)^2\right]^2} \right). \quad (34)$$

In the following it is described how a computer code can accurately generate the spectra described by the above equation. The key is to find a way to overcome the computational problem of dealing with the enormous number of lines adding to the sum.

4.6.2 Generating simulated spectra

In order to generate a spectrum from simulated HF data one needs to find an efficient way to sum up all the individual lines described by equation (34). In principle, it can be straightforwardly achieved by a computer code to run through all the permutations of m_{I,k,i_k} with their corresponding a_k and P_{i_k} in order to find the position and relative intensity of each line and add them to the resulting spectrum. However, there are 3^N individual lines contributing to the sum which can require an enormous amount of computational resources as N can be up to 33 for the defects considered in this work. This large number comes from the fact that in some of the considered defects the nearest neighbor (nn1), second nearest neighbor (nn2) and even third nearest neighbor (nn3) atoms contribute to the HF spectrum. The vast majority of the 3^N individual lines is extremely improbable with an insignificant relative intensity. The key is to ignore all these lines while at the same time maximizing the simulated relative intensity.

The program written for this work achieves simulations of high accuracy with fast computation times. The program was written in the Matlab code [220] and is shown in appendix B. The key of the program is that a probability threshold P_{th} is defined in order to filter out lines that have a low probability. However, since every line still has to be checked for whether it is above or below the threshold, this alone does not avoid computational treatment of all 3^N lines. For this reason, the total number of atoms is split into smaller groups of up to 10 atoms and every combination of these groups is checked for its probability. Every combination that is below the threshold is filtered out at this step and for the rest the resulting line positions are saved in a vector. The groups are then combined to bigger groups followed by a further filtering step and a calculation of the line positions until ultimately all groups are combined and a spectrum of the remaining lines is generated.

Table 4.2 shows how the probability threshold P_{th} influences the total simulated intensity, the number of lines, and which interactions are considered. The simulated defect is a $\mathrm{N_C V_{Si}}$ which is composed of 28 atoms with a considerable HF splitting, resulting in a total number of $3^{28} \approx 22.87 \times 10^{12}$ lines. Figure 4.4 shows how more and more distinct features are added to the spectrum as the simulation is performed with higher accuracy. The program containing this particular simulation is fully printed in appendix B. Note that while the simulation program includes the option to plot a simulated spectrum using Lorentzian or Gaussian lineshapes only the former was found to be a good representation of the spectra observed in this work, as mentioned above. The simulation demonstrates the efficiency of the filtering steps that pick the most important contributions to the spectrum out of the 3^{28} possibilities. Furthermore, it shows that a spectrum of high accuracy requires consideration of lines that are individually well below the detection limit. However, there are many of these lines close together all contributing to the spectrum and ultimately adding up to observable line features.

Table 4.2: Influence of the probability threshold on the total simulated intensity, the number of lines, and the included interactions for a simulation of the $N_C V_{Si}$ defect. This table was generated by the program as printed in appendix B.

P_{th}	Simulated intensity (%)	Lines	Included interactions
10^{-2}	76.6	57	^{29}Si (1×)
10^{-3}	87.3	165	^{29}Si (1×) , ^{13}C (1×)
10^{-4}	92.0	597	^{29}Si (1×, 2×) , ^{13}C (1×)
10^{-6}	99.2	21945	^{29}Si (1×, 2×, 3×) , ^{13}C (1×, 2×),...

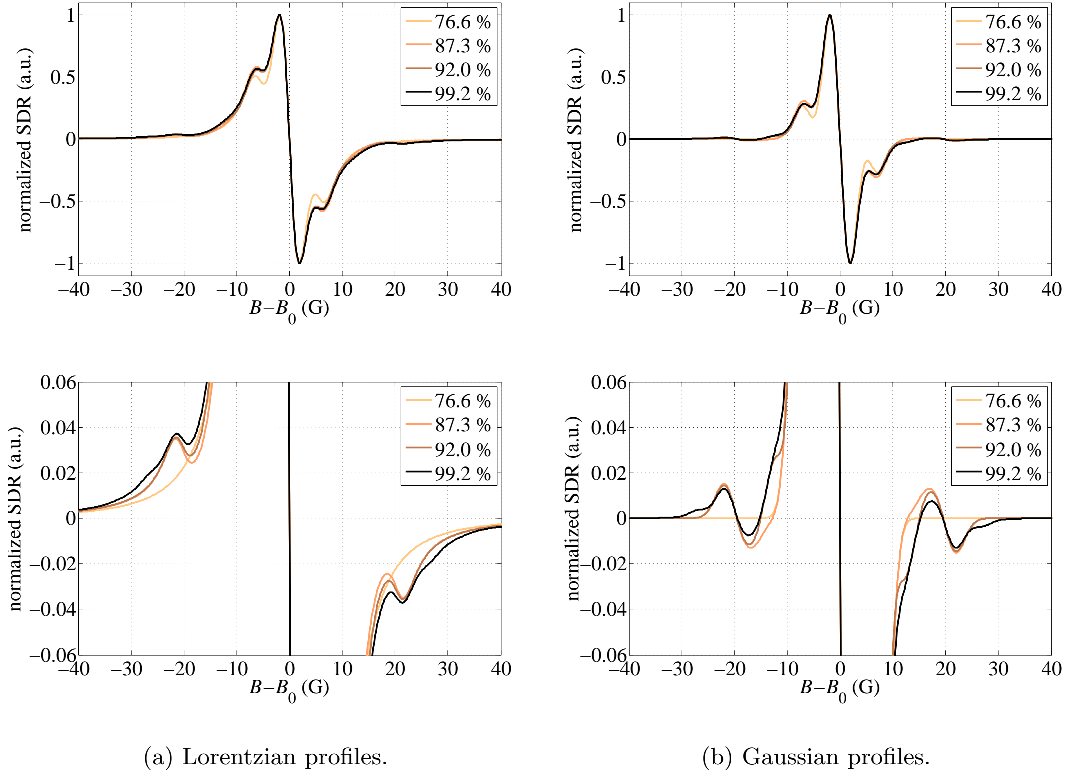

(a) Lorentzian profiles.

(b) Gaussian profiles.

Figure 4.4: Simulated EDMR curves considering different fractions of the total relative intensity (see also table 4.2) and different line profiles. The upper graphs show the full spectra which were normalized with respect to the peak-to-peak height and the lower graphs show a magnified view.

Chapter 5

Transmission electron microscopy (TEM)

Electron microscopy techniques are well-established means in materials science for the study of the microscopic structure of various materials. The techniques are based on detecting the signals caused by the interactions of a high-energy electron beam with a specimen. Figure 5.1 shows the detectable signals that are generated by the interactions of the beam electrons with a thin specimen that allows for the electrons to be transmitted. The arrows do not necessarily reflect the direction of the signals but crudely indicate where the respective signal is usually detected. While there are multiple techniques in electron microscopy, this chapter only introduces TEM techniques which predominantly focus on the electron signals in the lower half of Figure 5.1. Note that only a brief introduction of the detectors and experimental methods used in this work is given in here. A very detailed introduction into TEM can by found in the textbook by D.B. Williams and C.B. Carter [224].

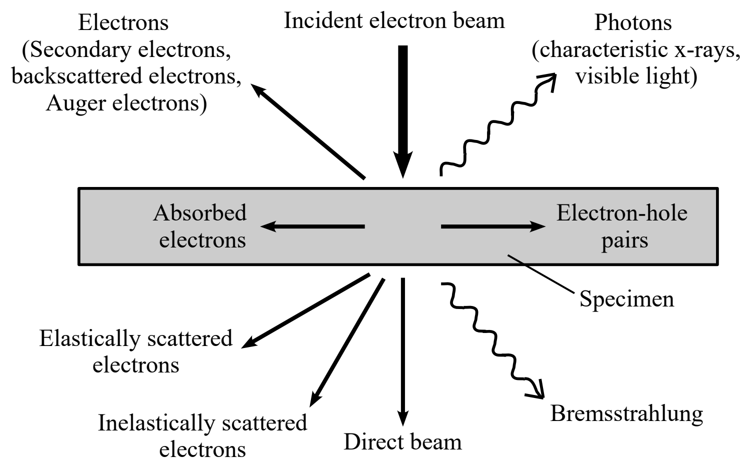

Figure 5.1: Signals created by the interaction of an incident high-energy electron beam with a thin specimen [224].

5.1 Instrumentation

The microscope consists of a high vacuum chamber where an electron beam is accelerated by a high voltage and focused by electromagnetic lenses. The beam interacts with the specimen which is thinned to electron transparency. The electrons penetrating through the sample are detected by different detectors. The microscope used for this study was a *FEI Titan*^{3} *G2 60-300* C_s-corrected transmission electron microscope [225, 226, 227]. This microscope allows for high-resolution TEM and EELS measurements. All measurements were performed in the scanning transmission electron microscopy (STEM) mode in which the beam is scanned over the sample allowing for high resolution imaging (see Figure 5.2) and spatially resolved EELS analysis. All data analysis was performed using the Gatan Microscopy Suite software [227]. In the following the detectors used are briefly introduced.

5.1.1 Bright field (BF)

The bright field (BF) is the signal generated by the direct beam and is therefore a measurement of the electrons that pass through the specimen without any interaction. The BF is the most basic STEM signal. The contrast in a BF image comes from the absorption or scattering of electrons which is dependent on the sample thickness and density of the sample [225, 227].

5.1.2 Annular dark field (ADF)

The annular dark field (ADF) is the signal of the electrons scattered by low angles of typically $< 3\,°$ [224]. The detector is a ring detector surrounding the direct beam and picking up the signal of the scattered electrons [225, 227]. This signal is in principle complementary to the BF signal [224].

5.1.3 High-angle annular dark field (HAADF)

The high-angle annular dark field (HAADF) signal comes from electrons scattered by high angles of $> 3\,°$ [224]. The HAADF detector is a ring detector surrounding the ADF detector [225, 226, 227]. The signal is strongly dependent on Rutherford scattering and the scattering cross section is dependent on the atomic number Z, and consequently the density of the material [224]. The HAADF signal can be used for atomically resolved Z-contrast imaging which shows the areal density ρ of the studied sample.

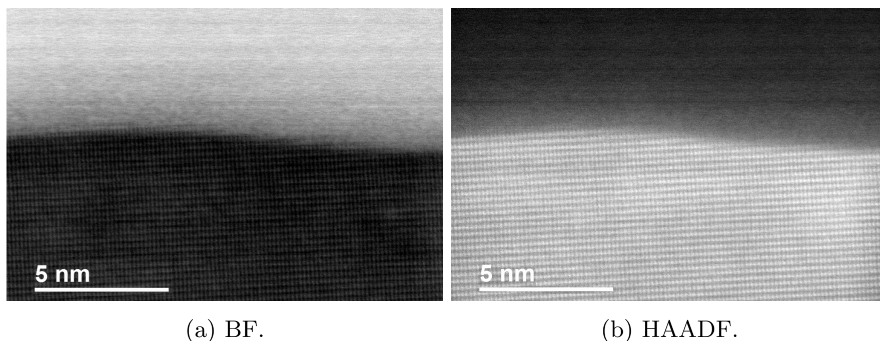

(a) BF. (b) HAADF.

Figure 5.2: Comparison of STEM images of the SiC-SiO_2 interface recorded with different detectors.

5.1.4 Electron energy loss spectroscopy (EELS)

The inelastically scattered electron passing through the sample contain valuable chemical information on the atoms they interacted with. EELS aims to gain this information by measuring the energy distribution of the electrons transmitted through the sample. An EELS detector contains an energy filter that allows for the detection of electrons of a specific energy. The energy filter is basically a magnetic prism, usually with an energy resolution of $< 1\,\text{eV}$ [224]. The system used in this work is a Gatan Quantum ERS energy filter with a minimum energy dispersion of $< 0.1\,\text{eV}$ [225, 227].

An EELS spectrum is the distribution of detected electrons plotted over the energy loss E_{loss}, as shown in Figure 5.3. The energy loss of an electron passing through the sample strongly depends on the atomic species it interacts with. Inelastic scattering of a beam electron with an electron in the sample causes the electron to lose energy. When a beam electron ionizes a core electron it loses the energy required for the ionization. Since every chemical element has specific ionization energies [228], EELS can give clues about the chemical composition of the sample. Figure 5.3 shows the position of the ionization edges of Si, C, and O [228]. The dashed line is a $10\times$ magnified view in order to show the edges at lower intensity. Note that the vast majority of electrons pass through the sample without ionizing atoms. Therefore, the zero-loss peak is orders of magnitudes higher than the elemental peaks and is not shown in Figure 5.3.

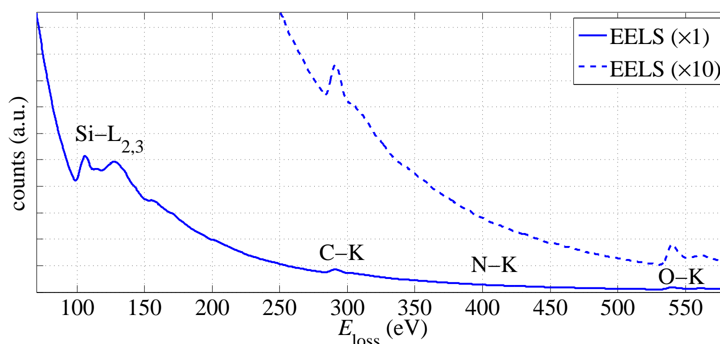

Figure 5.3: EELS spectrum of the SiC-SiO_2 interface with the labeled ionization edges of the present atom species [228].

The experimental setup allows for "Dual EELS", i.e. the simultaneous recording of two windows on the energy loss scale. One window was set on the zero-loss peak and was used to calibrate the energy loss axis of the spectra. The second window was set as shown in Figure 5.3 in order to get the EELS signals from the atom species contained in the studied samples.

Figure 5.4 shows the Si-$L_{2,3}$ EELS ionization edge for a linescan across the SiC-SiO_2 interface. What is clearly observed is that the position of the Si-$L_{2,3}$ edge shifts by $\approx 5\,\text{eV}$ from bulk SiO_2 to bulk SiC. Also the energy-loss near-edge structure (ELNES) which is the spectrum range towards higher energy from the edge changes. Both clearly indicates a difference of the chemical environment of the Si atoms in the different materials, which demonstrates the analytical power of spatially resolved EELS.

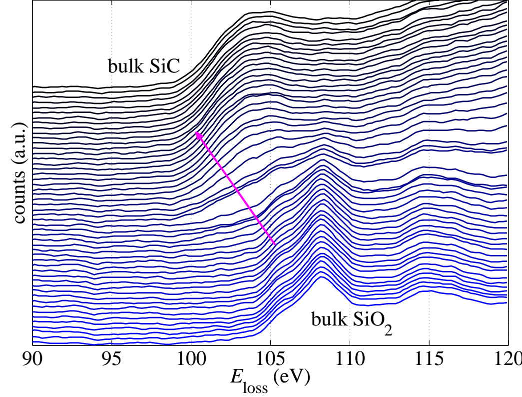

Figure 5.4: Si-$L_{2,3}$ EELS ionization edge for different positions on a linescan across the SiC-SiO_2 interface. The spectra are vertically shifted for better visibility.

5.2 Determining the interface thickness

One task in the experiments described in chapter 9 was to compare the interface thickness of two differently processed SiC-SiO_2 interfaces, since some studies in the literature found a correlation between the interface thickness and the channel mobility [89, 95]. Therefore, it was important to find a reliable method to determine the interface thickness.

Several interface profiles can be gained from the detected signals described above. The Z-contrast from the HAADF detector changes from one side of the interface to the other due to the different atomic mass and density of the materials. The C intensity vanishes towards the SiO_2 side and the O intensity vanishes towards the SiC side. The Si-$L_{2,3}$ edge shifts in energy which can be plotted as a profile. All those profiles are shown in 5.5. Note that for better comparison all profiles have been normalized and some of them inverted. Figure 5.5a shows one individual recording of a linescan across the SiC-SiO_2 interface, while Figure 5.5b is the mean of five individual recordings.

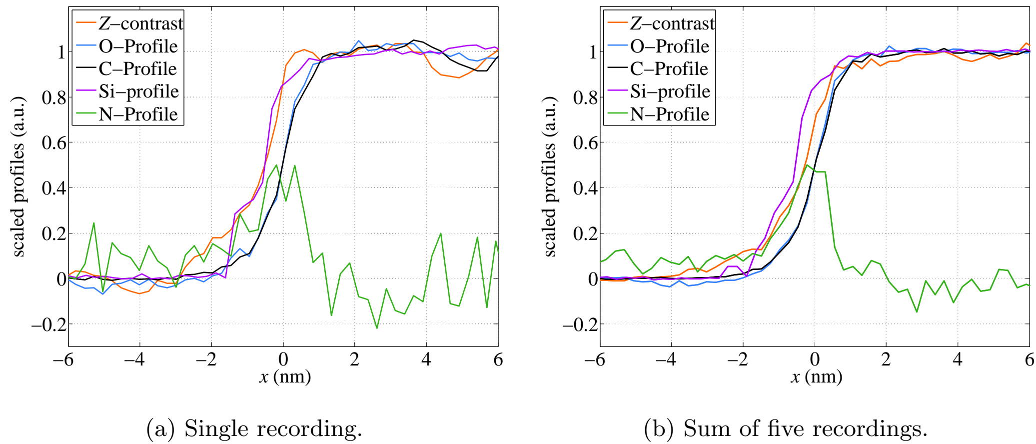

(a) Single recording.

(b) Sum of five recordings.

Figure 5.5: Normalized profiles of the SiC-SiO_2 interface obtained by STEM and EELS.

While each of the profiles mentioned above can in principle be used to determine and compare the interface thickness, it was suggested by J. Taillon et al. that the Si-$L_{2,3}$ chemical shift method is the most reliable method [95]. What is evident is that the Z-contrast profile contains some artifacts and is generally wider than the other profiles. Consequently, it is deemed not to be reliable for determining the interface thickness. The C and O profiles are matched very well and have almost an identical trend all across the interface that is also well reproduced between individual measurements. Therefore, they are determined to be a good means of comparing the interface thickness. The Si-$L_{2,3}$ chemical shift profile contains certain artifacts and noise. While in principle the values determined by this method are slightly smaller than those obtained from the C and O profiles, some problems occur by determining the position of the ionization edge, see appendix C. Additionally, it is not understood why the profile is shifted by $\approx 0.5\,\mathrm{nm}$ towards the SiO_2 side. Therefore, it is concluded that the most trustworthy comparison of the interface thickness can be achieved using the C and O profiles and is the one applied in chapter 9.

Part III

Results

Chapter 6

Identification of the $N_C V_{Si}$ center in N-implanted 4H-SiC *pn*-junctions

This chapter demonstrates how a defect can be identified using EDMR combined with theoretical modeling. A N-implanted 4H-SiC *pn*-junction was measured by SDR and showed a well resolved spectrum of the dominant recombination center. The benefit of using SDR instead of EPR here is mainly that the high concentration of shallow N_C donors is not detected, as only deep levels play a role in the recombination [7, 106, 107]. The observed center has been studied by SDR before but its structure has not yet been identified with certainty [7, 176]. In the present work it was possible to identify this unknown defect as the neutral $N_C V_{Si}$ by comparing the experimental data with extensive simulations. This defect could be an explanation for the dopant deactivation that has been reported for highly N-implanted SiC [229]. The methodology that was developed to identify this bulk defect can be used for further identifications of defects that reside at the SiC-SiO_2 interface.

Starting out from the experimental results that suggested a N-containing defect, extensive DFT modeling was performed by J. Cottom in a joint project with the University College London. The theoretical work considered a list of simple N-containing defect complexes as possible candidates. Many of these were ruled out on the basis of energetic arguments, as a basic requirement is the existence of accessible paramagnetic states deep in the bandgap. From the remaining defects some were further excluded due to their symmetry and HF parameters. By comparing the experimental spectrum with simulated spectra the $N_C V_{Si}$ in the neutral charge state was the only defect that remained as a reasonable candidate. This simulation considered the most probable thousands of HF lines out of the billions of possibilities (see also section 4.6) and also included different sites of the defect. This work demonstrates how EDMR spectra can be used to successfully identify defects even though they are often broadened and many of the HF lines are hidden. This chapter outlines the steps that were necessary to achieve a convincing identification of an unknown defect. The work was published in a special issue of the *Journal of Applied Physics* [6]. The identification of this defect resulted in some follow-up theoretical investigations of how this defect can react or be passivated [230, 231].

6.1 Defects in SiC caused by N implantation

As outlined in section 1.5, N is the most commonly used shallow donor in 4H-SiC. The N atoms are conventionally brought into the crystal by ion implantation which damages the crystal lattice and leaves N atoms at various positions. High temperature anneals at $\approx 1700-1800\,^{\circ}$C are used to heal the damaged crystal and to create the desired N_C donors. However, it has been shown that even after these high temperature anneals the donor concentration can be lower than the implanted N concentration [229]. Even for very high implantation doses the resulting donor concentration saturates [51]. Consequently, part of the implanted N forms other defect complexes, likely by reacting with intrinsic defects. Theoretical work has demonstrated how N can react with the V_C, the V_{Si}, and the $V_C V_{Si}$ [173]. The resulting defect complexes create states deep in the bandgap or are even completely electrically and optically inactive, like the fully N-passivated V_{Si} ($V_{Si}\,(N_C)_4$) [173]. However, these models have yet to be confirmed by experiments of which EPR and related methods can give a lot of insight.

N-implanted SiC crystals have been well studied by EPR, proving that the dominant center that forms after N implantation is the shallow N_C defect [60, 175, 177, 178]. What has also been confirmed by those studies is a site dependence. The structure of the defect is different for the k and the h site. For the former the HF splitting due to the nuclear spin $I = 1$ of the N nucleus is clearly resolved while for the latter it is much smaller and remains unresolved. However, conventional absorption detected EPR spectra are generally dominated by these two patterns, as they are highest in concentration and overshadow most of the other defects present in the material. Therefore, these measurements give few insights into what other defects are formed by the implantation. One related center that was often reported is the N_x center [60, 175, 177, 178]. However, those studies have shown that this defect is simply a closely located N_C pair. Therefore, it is not a complex formed by interaction with an intrinsic defect. There are few EPR studies where other N-related defects could be observed. Some of them suggested the $N_C V_{Si}$ [147, 179, 232] out of which the study of van Bardeleben et al. very convincingly identified this defect in its negative charge state [147]. In that study the measured defect was compared to theoretical modeling and could be identified due to its calculated zero-field splitting and due to its resolved HF spectrum. The resolved lines showed a triplet of equal intensity lines split by $a_N = 0.4\,$G proving it to be the $N_C V_{Si}$. It was also possible to detect the EPR spectrum of this defect at room temperature [147].

EPR studies often use samples specifically treated for a *high concentration* of a certain defect to be studied. It is questionable which of the defects additional to the N_C are really present in functional devices, as device processing has the goal to minimize undesired defect concentrations. EDMR is the only method that can directly measure the EPR spectra of defects residing in fully manufactured devices. Several studies investigated defects in N-doped *pn*-junctions by using SDR [7, 233, 234]. A benefit of using SDR is that it only detects deep level defects as they are the most efficient recombination centers [106, 107]. Consequently, the spectra are free of the large concentration of the shallow N_C donors. The study by T. Aichinger et al. compared implanted N-doped samples with epitaxially grown ones [7]. They convincingly showed that a defect is created by implantation, as the observed spectrum was absent in the epitaxially grown sample. The defect due to the implantation was therefore assigned to an unidentified N complex [7]. The observed HF structure was interpreted in terms of a resolved N splitting. Theoretical work attempted to identify this defect by simulating different complexes using DFT [176]. The defect was tentatively assigned to the N_C coupled to a C_{Si} ($N_C C_{Si}$). However, the assignment was based on the resolved N splitting and there were certain doubts. On the one hand the observed symmetry was different and one the other hand the theoretically calculated HF splitting was too large [176]. In summary, while SDR

was able to measure dominant deep level defects in 4H-SiC *pn*-junctions and assigned them to N complexes, no convincing identification was achieved until the work presented here and published in [6].

6.2 Experimental results

The sample that was investigated was a 4H-SiC *pn*-junction embedded in a fully operational device. The *n*-doped region was formed by a N implantation that resulted in a doping concentration of $n = 5 \times 10^{17}\,\mathrm{cm}^{-3}$. The *p*-doped region was formed by an Al implantation at a similar dose. The sample received an anneal at 1800 °C in order to activate the dopants and to heal damage from the implantation. The SDR measurements were performed at a diode forward bias of $V_\mathrm{f} \approx 2.35\,\mathrm{V}$ which resulted in a high signal and a good signal-to-noise ratio. In order to minimize broadening effects and to have a good resolution of the HF structure, the measurements were performed at a microwave power of $P_\mathrm{mw} = 50\,\mathrm{mW}$ and a modulation amplitude of $B_\mathrm{mod} = 0.5\,\mathrm{G}$. Lock-in amplification with a modulation frequency of $f_\mathrm{mod} \approx 900\,\mathrm{Hz}$ and extensive signal averaging was performed.

The recorded spectra with the magnetic field applied in the [0001] ($B\|c$) and the [$1\bar{1}00$] ($B\perp c$) directions are shown in Figure 6.1. The determined *g*-factors are $g_{B\|c} = 2.0054(4)$ for the former and $g_{B\perp c} = 2.0004(4)$ for the latter. The defect is within the experimental error rotationally symmetric about the *c*-axis. There are some small deviations, likely due to the 4 ° off-axis growth of the substrate. There is a good agreement with the results obtained in the study by T. Aichinger et al. [7].

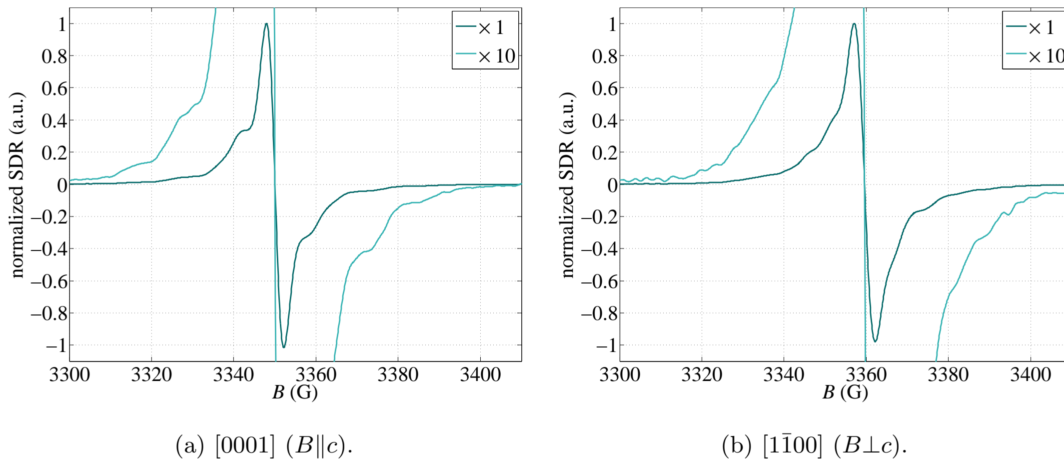

(a) [0001] ($B\|c$).

(b) [$1\bar{1}00$] ($B\perp c$).

Figure 6.1: Normalized SDR spectra of a N-implanted *pn*-junction with B applied in different directions.

The $B\|c$ spectrum is evidently sharper and has better resolved HF peaks than the $B\perp c$ spectrum. This can be understood in terms of the crystal structure of 4H-SiC. As the *c*-axis is the symmetry axis the spectrum for this direction contains the most equivalent lattice sites. When the sample is tilted out of this axis the degeneracy is lifted and more sites become inequivalent. Apparently there is a small anisotropic component in the HF splittings which broadens the $B\perp c$ spectrum and makes a clear determination for the HF parameters difficult. Therefore, all further considerations focus on the $B\|c$ spectrum.

The spectrum in Figure 6.1a contains two clearly resolved pairs of HF lines that are each equally spaced from the center line. The first pair is found at $\approx \pm 6.5\,\mathrm{G}$ away from the center line and is higher in intensity. These peaks have been assigned to N in the study by T. Aichinger [7]. However, this model was achieved by fitting, which can be misleading as the spectra are often made up of many unresolved lines. The second pair of HF peaks is found at $\approx \pm 21\,\mathrm{G}$. with a much smaller relative intensity. In a scan up to 600 G away from the center line no further resolved peaks were found outside the window shown in Figure 6.1a. Therefore, the comparison of the simulated models with the experiments was focused on how well they could match the $\approx \pm 6.5\,\mathrm{G}$ and $\approx \pm 21\,\mathrm{G}$ peaks as well as their relative intensities.

6.3 Theoretical modeling

The experimental results that have been briefly described above were the basis for extensive theoretical modeling using DFT. This was conducted in a joint project at the University College London by J. Cottom. All details on the DFT simulations are found in the joint paper [6] and only a brief summary of this theoretical work is presented here.

As the measured defect is caused by the N implantation and is absent in epitaxially grown N-doped samples [7], all considered defects were N complexes. The "long list" of simulated defects included the substitutional nitrogen at the silicon site ($\mathrm{N_{Si}}$), the $\mathrm{N_C}$, the nitrogen interstitial ($\mathrm{N_i}$), the $\mathrm{N_C}$ coupled to a $\mathrm{N_{Si}}$ ($\mathrm{N_C N_{Si}}$), the $\mathrm{N_C C_{Si}}$, the $\mathrm{N_C V_{Si}}$, and the $\mathrm{N_{Si}}$ coupled to a $\mathrm{V_C}$ ($\mathrm{N_{Si} V_C}$) defects. The defects were modeled by using the CP2K code with the PBE and HSE06 functionals [235, 236, 237]. The supercell used for the simulation was a $5 \times 4 \times 2$ orthorhombic supercell containing 480 atoms and a size of $15\text{Å} \times 16\text{Å} \times 20\text{Å}$. The model allowed for the defect relaxation to be contained within the supercell.

For all defects the formation energy E_{form} was calculated according to the equation

$$E_{\mathrm{form}} = E_{\mathrm{d}}\,(q) + \sum_{s} n_s \mu_s + q\,(E_{\mathrm{V}} + E_{\mathrm{F}}) - E_{\mathrm{bulk}} \tag{35}$$

where $E_{\mathrm{d}}\,(q)$ is the total energy of the defective cell for a charge state q, n_s is the number of atoms of species s and μ_s is their respective chemical potential, E_{V} is the energy of the valence band, E_{F} is the Fermi energy, and E_{bulk} is the total energy of the defect free bulk. It is worth noting that the calculations were made for $T = 0\,\mathrm{K}$. The resulting energies are used to find the transition levels between charge states in the bandgap by looking for the lowest energy state for a given Fermi energy. This assumes that the system is in thermodynamic equilibrium which may not always be valid.

For the different defect models which have paramagnetic charge states in the bandgap, which is a basic requirement to be detected by EPR and EDMR, the HF parameters were calculated. For this the Gaussian augmented-plane wave (GAPW) method [235] was used with the pcj family of basis-sets [223]. These basis sets are capable of accurately considering the Fermi-contact term, e.g. the density of the electron at the nuclear site, which gives rise to the isotropic HF component [134].

The functionals and basis sets were extensively tested on different systems and compared to the literature. This included the $\mathrm{N_C N_{Si}}$, $\mathrm{N_{Si}}$, $\mathrm{N_C}$, and $\mathrm{N_i}$ defects which were considered for completeness but can be ruled out as candidate defects based on prior studies [138, 173, 174, 175]. The "short list" of defects that were left as candidates were the $\mathrm{N_C V_{Si}}$, $\mathrm{N_{Si} V_C}$, and $\mathrm{N_C C_{Si}}$ defects. These defects have paramagnetic states deep in the bandgap and were further investigated in terms of their symmetry and HF structures.

The three remaining defect complexes are all composed of a neighboring pair of a N atom and a vacancy or antisite. Due to the inequivalent sites in the 4H-SiC crystal, the pair can have four different conformations: hh, $hk_{1,2,3}$, $kh_{1,2,3}$, and kk. As indicated by the indices the mixed symmetry conformations are triply degenerate. In terms of their formation energies the different conformations are within $\approx 0.05\,\mathrm{eV}$. Figure 6.2 shows the formation energy plotted over the Fermi level of the "short list" defects in their different charge states. The bold lines mark the lowest energy charge state for each defect at given Fermi energy. The $N_C V_{Si}$ and $N_{Si} V_C$ are considered as a reconstruction of the same defect. A more detailed theoretical consideration of the reconstruction of these defects is given in follow-up studies [230, 231]. All three defect candidates have accessible paramagnetic states in the bandgap. The $N_{Si} V_C$ is paramagnetic in the 0, -1, and -2 charge states. The -1 charge state can be ruled out as a candidate defect, as no spectral lines with the reported large zero-field splitting were observed in our experiments [147]. The $N_{Si} V_C$ in the +2 charge state is lower in energy than the $N_C V_{Si}$ close to the valence band and paramagnetic. The other charge states are much higher in formation energy and would be transformed into a $N_C V_{Si}$ during the high temperature anneal [230, 231]. For the $N_C C_{Si}$ only the 0 charge state is paramagnetic. It is emphasized here that especially the charge states close to the middle of the bandgap are expected to be efficient recombination centers which can be observed by SDR [7, 106, 107].

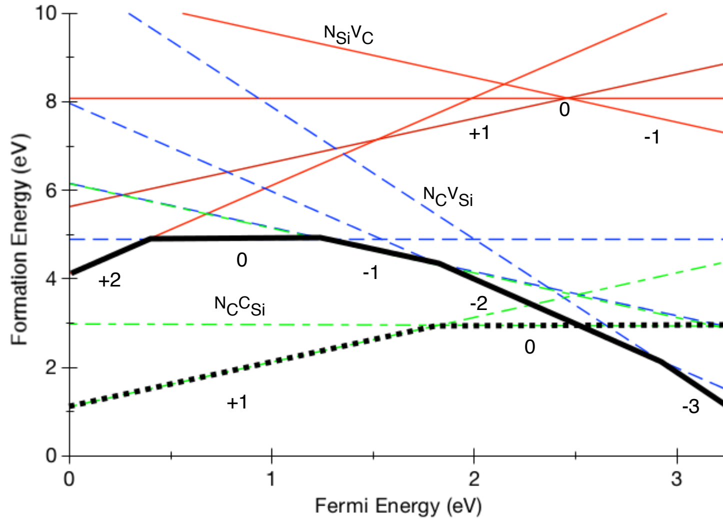

Figure 6.2: Formation energy of the $N_C C_{Si}$, $N_C V_{Si}$, and $N_{Si} V_C$ defects dependent on the Fermi energy with respect to the valence band edge. Reproduced from [6], with the permission of AIP Publishing.

The spin density plots of the $N_C V_{Si}{}^0$, the $N_{Si} V_C{}^{+2}$, and the $N_C C_{Si}{}^0$ are depicted in Figure 6.3. The comparison shows significant differences between these defect complexes. For the $N_C V_{Si}{}^0$ the spin density is mostly spread over the three nn1 C atoms and their back-bonded nn2 Si atoms while there is almost no spin density at the N atom. There is a weak correlation between two of the three unpaired electrons. Both a doublet and quartet state exist with the former being $\approx 0.1\,\mathrm{eV}$ lower in energy. The $N_C V_{Si}{}^{-2}$ looks very similar with just one unpaired electron cloud being present instead of three. The $N_C V_{Si}$ introduces very little strain due to relaxations as the bond lengths of the N-Si bonds (1.79 Å) are almost the same as for the C-Si bonds (1.75 Å). A very different picture is seen for the $N_{Si} V_C{}^{+2}$ where almost the entire spin

density is centered at the N atom which relaxes back to the plane formed by its back-bonded C atoms. This defect was discarded as the resulting symmetry does not match the experimental data and the HF splitting of the N atom is too high. The $N_C C_{Si}{}^0$ has the C antisite atom residing between the three nearest neighbor C atoms. Also for this defect a significant relaxation takes place. The spin density is to a large part located at the C antisite atom. There is also a considerable unpaired electron localization on the N atom. The symmetry of this defect is the same as for the $N_{Si}V_C{}^{+2}$ and also seems to rule out this defect. However, the $N_C C_{Si}{}^0$ defect was deemed a likely candidate in the literature [176]. For completeness, its HF parameters were calculated and compared to the experiment along with the more promising $N_C V_{Si}{}^0$ and $N_C V_{Si}{}^{-2}$ defects, as discussed next.

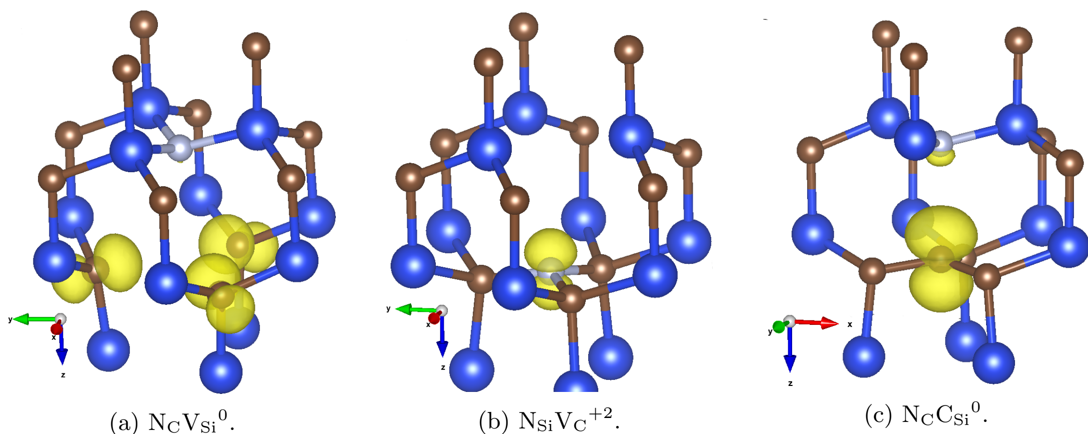

(a) $N_C V_{Si}{}^0$. (b) $N_{Si}V_C{}^{+2}$. (c) $N_C C_{Si}{}^0$.

Figure 6.3: Unpaired electron density (yellow) for different candidate defect models. Si atoms are blue, C are brown, N is white. Reproduced from [6], with the permission of AIP Publishing.

6.4 Comparison between experiment and theory

The defect models explained above were compared to the experimental spectrum by calculating the HF parameters and generating simulated spectra from this data. The calculated HF coupling constants for the various candidate defect models are summarized in Table 6.1. The values were calculated using the pcj-1 basis set [223]. The values are for simplicity averaged over the equivalent atoms and only contain the (lowest energy) hh conformation, as calculating all conformations would have been too expensive in terms of computation time. A significant difference between these defects comes mostly from the N splitting. As discussed above, the $N_C C_{Si}{}^0$ has a certain spin density located at the N atom while this is not the case for the

Table 6.1: Calculated HF splitting constants a_k for the $N_C V_{Si}$ and the $N_C C_{Si}$. The parameters have been averaged over the equivalent atoms of each shell. a_{C1} stands for the nn1 C atoms, a_{Si2} for the nn2 Si atoms, and a_{C3} stands for the nn3 C atoms.

Defect	a_N (G)	a_{C1} (G)	a_{Si2} (G)	a_{C3} (G)
$N_C V_{Si}^0$	0.8	39.9	10.7	6.7
$N_C V_{Si}^{-2}$	0.8	46.7	9.2	6.1
$N_C C_{Si}^0$	11.2	39.9	10.7	6.7

$N_C V_{Si}$. This large splitting would be easily observable in the SDR spectrum as the linewidth is significantly smaller. This was the basis of the assignments made in the literature [7, 176]. The HF splittings of the Si and C atoms are comparable for all defect models.

The splitting constants in Table 6.1 were used to simulate the defect's HF spectra according to the methodology described in section 4.6. These spectra are shown in Figure 6.4. This comparison reveals that the $N_C V_{Si}{}^0$ is by far closest to the experimental spectrum. Both the ± 6.5 G and ± 21 G peaks are well matched by the nn1 C and nn2 Si atoms, respectively. For the $N_C V_{Si}{}^{-2}$ the Si peaks are mostly hidden within the linewidth. The $N_C C_{Si}$ is at this stage ultimately ruled out as a candidate defect, as neither the HF splitting nor the relative intensity of the N peaks matches the experimental data. It is emphasized at this point that the error of the calculated splitting constants due to the use of the pcj-1 basis set was estimated to be ± 3 G. Even when considering this error the $N_C V_{Si}{}^0$ remains the best candidate defect and was simulated more extensively for an improved comparison.

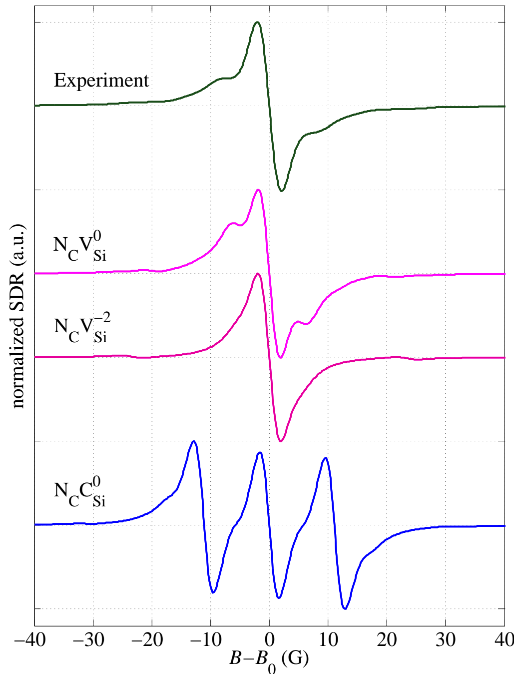

Figure 6.4: Experimental spectrum compared to simulations created with the values from Table 6.1. Reproduced from [6], with the permission of AIP Publishing.

As described above the $N_C V_{Si}$ comes in four conformations two of which are triply degenerate. So far only the hh conformation has been considered, as it is the lowest energy conformation. For a more sophisticated comparison, the different conformations have been calculated individually and their respective spectra were generated. The calculation of the HF splitting constants was performed with the pcj-1 basis set, despite the error of ± 3 G. Again the argument was that more accuracy would require too much computational effort. The HF parameters are listed in Appendix A. This time no averaging over the equivalent atoms was performed when generating the simulation. Every atom and its HF splitting constant was considered individually. The simulated spectra were generated according to section 4.6 for each of

the inequivalent sites and are shown in Figure 6.5a. The relative intensities are weighted with a Boltzmann factor in order to account for the different formation energies. Even though this assumes a thermodynamic equilibrium to be reached, which is a crude assumption, it is the most reasonable approximation to be made. The sum of these lines results in a spectrum that is evidently improved and closer to the experiment as can be seen in Figure 6.5c. The relative intensities of the HF peaks match very well with those in the experimental spectrum. However, the HF splitting constants are underestimated by $\approx 2\,$G. This comes from the chosen basis set and the error outlined above.

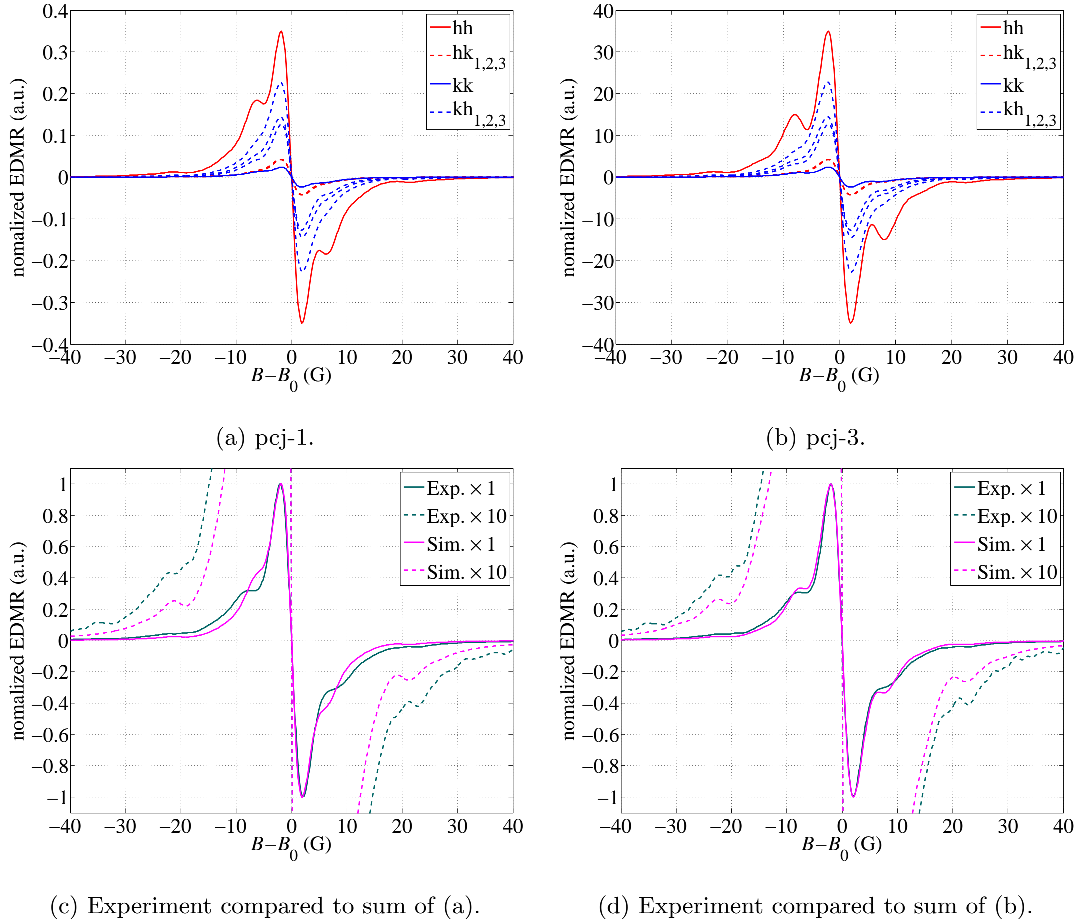

(a) pcj-1.

(b) pcj-3.

(c) Experiment compared to sum of (a).

(d) Experiment compared to sum of (b).

Figure 6.5: Weighted simulated spectra of the $N_C V_{Si}$ at different sites calculated with pcj-1 (a) and gauged with pcj-2 and 3 (b). The sums of the curves are compared to the normalized experimental spectrum in (c), and (d) respectively. Reproduced from [6], with the permission of AIP Publishing.

In order to further improve the simulation and to demonstrate that the mismatch is indeed caused by the error of the chosen basis set, a final simulation of the HF parameters was made using the pcj-3 basis set [223] with an estimated error of only $\pm 1\,$G. As this calculation required enormous computation it was only performed for the hh conformation of the $N_C V_{Si}{}^0$. The simulation resulted in nn1 C and nn2 Si splitting constants that are $\approx 2.5\,$G larger than

those calculated with the pcj-1 basis set. In order to demonstrate how this improves the accuracy of the simulation the spectra of the different conformations were generated again. The splitting constants were gauged with the result of the hh conformation, as a similar result for all conformations can be expected using the pcj-3 basis set. The improved weighted spectra are shown in Figure 6.5b. It can be clearly seen how the Si peaks moved outwards from the center when compared to Figure 6.5a. The sum of the peaks compared to the experimental spectrum is shown in Figure 6.5d. The spectra are matched extremely well and give a very convincing argument that the $N_C V_{Si}{}^0$ is indeed the dominant paramagnetic recombination center observed in the N-implanted 4H-SiC *pn*-junctions.

6.5 Summary

In this chapter it was shown how the structure of an unknown defect observed by SDR can be identified by the systematic approach of using DFT simulations and comparing the spectra generated from the theoretical results (as described in section 4.6) to the experimental spectra. A methodology was established that was successful in identifying a defect in bulk SiC and can be further used for identifying defects at the SiC-SiO_2 interface.

The basic observations made in the experimental spectra of a 4H-SiC *pn*-junction were used to define requirements for the candidate defects. These requirements were: a) accessible paramagnetic states deep in the bandgap in order to be observable by SDR, b) axial symmetry. From an initial list of possible candidates ($N_C V_{Si}$, $N_{Si} V_C$, $N_C C_{Si}$, N_C, N_{Si}, and N_i) a shorter list was generated and studied in terms of their formation energies of different states in the bandgap and the symmetry and HF splitting constants calculated for the states that are paramagnetic. The calculated HF splitting constants were used in order to generate simulated spectra that could be compared to the experimental data. This made it possible to narrow the list of candidates down to one remaining candidate: the $N_C V_{Si}{}^0$. This defect was then simulated further with a lot more accuracy and the final results showed an almost perfect match with the experiment. This defect is identified to be the dominant recombination center observed in a prior study on comparable samples [7]. The defect is associated with the dopant deactivation often observed in highly N-doped SiC. However, it cannot be ruled out that other diamagnetic or electrically inactive defects also contribute to the dopant deactivation, as the SDR measurement does not give any reliable information on the concentration of the observed defect.

Chapter 7

Defects at the SiC-SiO_2 interface of 4H-SiC MOSFETs and the influence of oxide processing

A central point of this work was the study of the defects at the SiC-SiO_2 interface using EDMR, as these defects have a major influence on the performance of MOSFETs. The biggest problem of state-of-the art SiC MOSFETs is the reduced channel mobility that is well below the bulk value [70]. There are different mechanisms that can reduce the channel mobility, but carrier trapping and scattering at defects at the interface are believed to be the most important ones [121]. Until today there is not a clear understanding of the structure of these defects and their passivation. It has been demonstrated that POAs in N-containing atmospheres can significantly reduce the defect concentration and increase the device mobility [75, 121]. Especially anneals in NO show enormous improvements of the channel mobility in SiC MOSFETs and have become a standard process in industry.

Due to its selectivity and sensitivity EDMR is a good tool to study the structure of electrically active interface defects in MOSFETs. Prior EDMR studies have suggested the V_{Si} [193, 194, 197, 199] or related defects [222] to be the dominant defect at the SiC-SiO_2 interface. It has also been shown how this defect can be passivated by NO anneals [196]. A study that was performed at an early stage of this thesis on n-channel MOSFETs with a DMOSFET-like structure suggested the dominant defect to be a V_{Si} close to the interface [2]. However, these measurements used a gated-diode-like biasing scheme that is not optimal for measuring defects at the interface, see also section 4.3 [197]. Consequently, these measurements were not very sensitive especially in terms of resolving low-intensity HF peaks.

In this chapter more extensive studies of the dominating defects in 4H-SiC MOSFETs processed with a modern deposited oxide were conducted. The focus was mainly put on a set of samples that received different POAs while having identical geometries. The devices were particularly designed to apply the BAE technique, which is extremely sensitive to paramagnetic defects at and very close to the interface, see section 4.4 and [197]. With this approach the best comparison of the defects that are dominant after the respective anneals could be achieved. Parts of these results were presented at the *International Conference on Silicon Carbide and Related Materials 2015* in Giardini-Naxos, Italy [5].

7.1 Sample description

The samples that were compared are summarized in Table 7.1. All samples are lateral n-channel 4H-SiC MOSFETs processed on the Si-face. One sample had a thermally grown oxide while the other samples had an oxide deposited by CVD. The oxide process for the former resulted in a very high defect concentration and the highest relative signal obtained out of all devices studied in this thesis. This device was mainly used as a reference sample. It has an $\approx$ 65 nm thick thermally grown gate oxide that received a POA in nitrous oxide (N_2O) containing atmosphere. The channel length is 5 μm and the channel width is 850 μm. The body is p-doped with Al at a concentration of $N_a \approx 10^{17}\,\mathrm{cm}^{-3}$ and the n-doped source and drain were formed by N implantation at a concentration of $N_d \approx 10^{20}\,\mathrm{cm}^{-3}$. All the other devices have an $\approx$ 80 nm thick oxide deposited in a CVD process. The channel length is 5.3 μm and the channel width is 100 μm. They are identical samples that only differ in terms of their POA anneal, as summarized in table 7.1. The p and n-regions have approximately the same doping concentrations as for the thermally grown sample.

All described samples were specifically designed to apply the BAE biasing scheme described in section 4.4, which allows for the highest sensitivity EDMR measurements of the defects at the SiC-SiO_2 interface [197]. This means that they all have a channel length in the range of the minority carrier diffusion length. Especially the CVD samples allow for a good comparison between their electrical properties and the measured EDMR response, as they have an identical geometry and oxide deposition process and only differ in their respective POA. Therefore, these devices are ideal to study the influence of the POA in different atmospheres on the defects at and very near the interface. Note that in the following the samples are referenced by their oxide process: therm. w/ N_2O, dep. w/ O_2, dep. w/ N_2O, and dep. w/ NO.

Table 7.1: Processing parameters of the studied n-channel MOSFETs.

Oxide	POA	t_{ox} (nm)	L (μm)	W (μm)	N_a (cm^{-3})	N_d (cm^{-3})
therm.	N_2O	65	5.0	850	$\approx 1 \times 10^{17}$	$\approx 1 \times 10^{20}$
dep.	O_2	80	5.3	100	$\approx 1 \times 10^{17}$	$\approx 1 \times 10^{20}$
dep.	N_2O	80	5.3	100	$\approx 1 \times 10^{17}$	$\approx 1 \times 10^{20}$
dep.	NO	80	5.3	100	$\approx 1 \times 10^{17}$	$\approx 1 \times 10^{20}$

7.2 Electrical characterization

Before conducting the EDMR experiments all samples were electrically characterized. Besides testing the devices for their functionality it gives a good insight into the impact of the POA on the device performance. The most important parameters that were extracted are the mobility μ_{LF} and the density of interface traps D_{it}. The former is a key parameter in terms of SiC MOSFET technology development. The second parameter tells about recombination centers at the interface. Additionally, the threshold voltage V_{th} was determined. The N treatment has been shown to have an enormous effect on these device parameters [75]. All measurements were performed on a wafer probing station at room temperature, as described in section 3.

Figure 7.1 shows the recorded electrical measurements. The transfer characteristics were measured by setting the source and body contacts to ground and putting a constant positive bias on the drain contact while measuring the drain current. Apart from the sample dep. w/ NO, all devices have rather flat transfer characteristics due to a low mobility. For this reason the drain voltage was increased for these devices in order to record transfer characteristics

suitable to extract the device mobility. The curves shown in Figure 7.1a were recorded with a drain bias of $V_\mathrm{d} = 5\,\mathrm{V}$ for device therm. w/ N_2O, $V_\mathrm{d} = 1\,\mathrm{V}$ for devices dep. w/ O_2 and dep. w/ N_2O, and $V_\mathrm{d} = 0.1\,\mathrm{V}$ for device dep. w/ NO. The mobility and threshold voltage were extracted from the transfer characteristics using the method of Ghibaudo (see section 3.1 and [82]). The respective values are summarized in Table 7.2. It is evident that sample dep. w/ NO is the sample with the best electrical properties followed by dep. w/ N_2O, dep. w/ O_2 and therm. w/ N_2O.

The density of interface traps was determined by constant base charge pumping measurements which are shown in Figure 7.1b. The base level was set to $-25\,\mathrm{V}$ and trapezoidal pulses with a duty cycle of $50\,\%$ and a frequency of $f_\mathrm{cp} = 100\,\mathrm{kHz}$ were applied. The rise an fall slopes of the pulses were $26.7\,\mathrm{V}/\mu\mathrm{s}$. From these measurements the density of interface traps was extracted according to section 3.2. For device therm. w/ N_2O, no reliable charge pumping measurements could be achieved, as the device geometry did not allow for it. However, due to the very poor mobility and flat transfer characteristics this device must have the highest defect density of all studied n-channel MOSFETs. The obtained values for the devices dep. w/ O_2, dep. w/ N_2O, and dep. w/ NO can be found in Table 7.2.

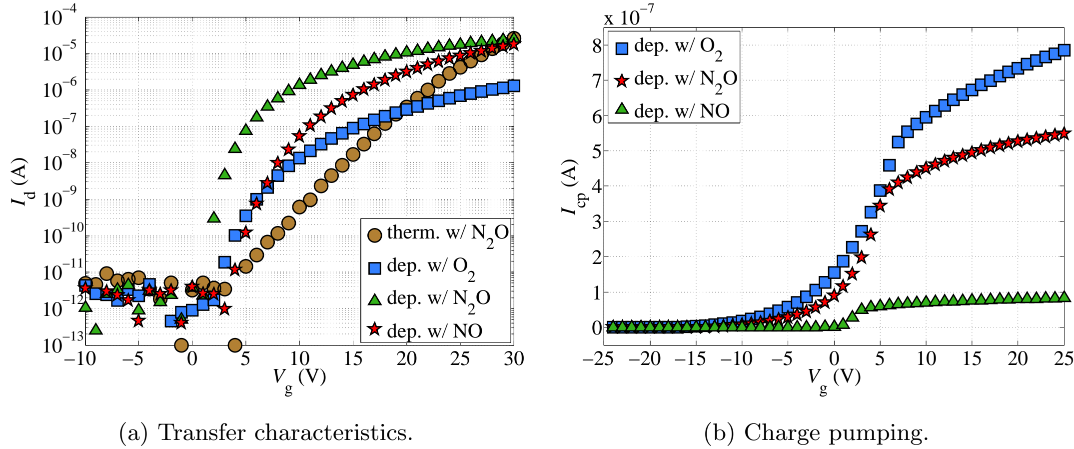

(a) Transfer characteristics.

(b) Charge pumping.

Figure 7.1: Electrical measurements on the differently processed MOSFETs.

Table 7.2: Device properties determined by electrical measurements of the studied n-channel MOSFETs.

Sample	μ_LF $\left(\mathrm{cm^2V^{-1}s^{-1}}\right)$	$V_\mathrm{th}\,(V)$	D_it $\left(\mathrm{cm^{-2}eV^{-1}}\right)$
therm. w/ N_2O	0.006	22.8	-
dep. w/ O_2	0.2	20.3	2.3×10^{12}
dep. w/ N_2O	2.2	19.5	1.7×10^{12}
dep. w/ NO	17.6	14.5	2.9×10^{11}

As expected, the electrical measurements demonstrate that the oxide processing has dramatic effects on the mobility, threshold voltage and density of interface traps. The obtained values in Table 7.2 are in agreement with a related study that focused on accurate characterization of devices that received identical oxide processing [75]. There is an inverse correlation between the density of interface traps and the device mobility indicating that the defects at

the interface are the reason for the degradation of the device performance. The electrical characterization indicates that this set of devices is ideal to study the effect of defects on the device performance as they cover a wide range of mobility and defect density. Especially the comparison between the devices dep. w/ O_2, dep. w/ N_2O, and dep. w/ NO which are identical despite their respective POA can give new insights into the defect passivation by N and its influence on the device characteristics.

7.3 EDMR results

All devices were extensively studied with EDMR using the BAE biasing scheme [197]. The source-to-body diode was therefore forward biased at usually $V_{\mathrm{sb}} = -3.5\,\mathrm{V}$. For all measurements shown in this chapter the microwave frequency was $f_{\mathrm{mw}} = 9.402\,\mathrm{GHz}$ and the magnetic field modulation frequency was $f_{\mathrm{mod}} = 900\,\mathrm{Hz}$. All spectra were recorded at room temperature, unless stated otherwise. In the following sections the devices are compared in terms of their EDMR signals.

7.3.1 Relative signals

As a first step, the relative signal intensities of the different n-channel MOSFETs were investigated. These measurements are important for determining the gate voltage at which the highest relative signal can be obtained for a given device. They also can be used as a qualitative comparison of the density of spin dependent recombination centers in the device channel. These measurements should be in accordance with the D_{it} determined through charge pumping.

Figure 7.2a shows a comparison of the relative current change $\Delta I/I_{\mathrm{d}}$ of the different MOSFETs and their dependence on the gate voltage. ΔI was determined by the double numerical integral for each recorded spectrum. A high microwave power of $P_{\mathrm{mw}} \approx 1\,\mathrm{W}$ and a high modulation amplitude of $B_{\mathrm{mod}} = 5\,\mathrm{G}$ were used in order to get a good signal-to-noise ratio. Even with these chosen parameters the NO-annealed sample dep. w/ NO needed extensive averaging in order to estimate the relative peak intensity of the EDMR signal, while for the other samples single scans were sufficient.

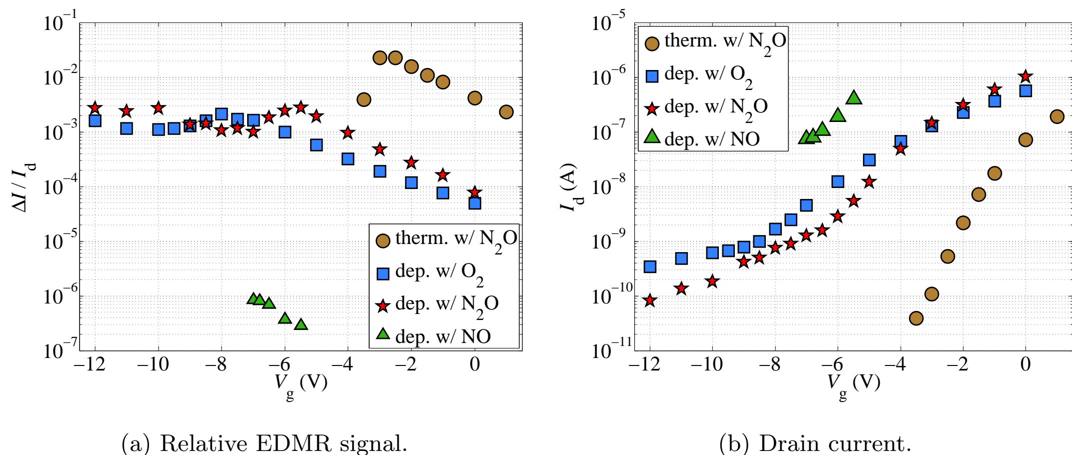

(a) Relative EDMR signal.

(b) Drain current.

Figure 7.2: Determination of the relative device current change under resonance and its dependence on V_{g}.

The results mostly correlate with what is expected from the electrical characterization with sample therm. w/ N_2O having the highest signal and dep. w/ NO having the lowest while samples dep. w/ O_2 and dep. w/ N_2O are in between. However, the maximum relative BAE current change obtained for sample dep. w/ O_2 is $\Delta I/I_d \approx 2.1 \times 10^{-3}$ while for sample dep. w/ N_2O it is $\Delta I/I_d \approx 2.7 \times 10^{-3}$. This seems to be at odds with sample dep. w/ O_2 having a higher D_{it} than sample dep. w/ N_2O. This result indicates that the D_{it} might also contain a certain concentration of defects that are invisible to the EDMR measurements. However, as the device parameters like channel mobility and threshold voltage also influence the drain current of the BAE measurements, it is not certain whether the relative intensities are comparable at the chosen biasing conditions. A better measurement to compare the relative intensities of paramagnetic interface defects could be attained by spin dependent charge pumping measurements [192]. However, these measurements were not in the focus of this work but rather a comparison using the BAE technique. Charge pumping measurements have been in the focus of a follow-up project [217].

7.3.2 Angular dependence of the g-factor

The angular dependence of the g-factors was measured as a first comparison of the different devices. The sample holder only allows for rotation along any axis that is perpendicular to the c-axis, as the sample has to be attached to the sample holder with its backside. Two tilt series were recorded which are shown in Figure 7.3. The rotational axes are the $[1\bar{1}00]$ in Figure 7.3a and the $[11\bar{2}0]$ in Figure 7.3b. As there was only one device of sample therm. w/ N_2O available, only one tilt series could be recorded. For sample dep. w/ NO every measurement required enormous signal averaging in order to determine the g-factor. Therefore, only a few points were recorded for this sample for a qualitative comparison. All recorded data points for the respective samples were fit with the function described in section 4.5. The principle values obtained from this fit are summarized in Table 7.3.

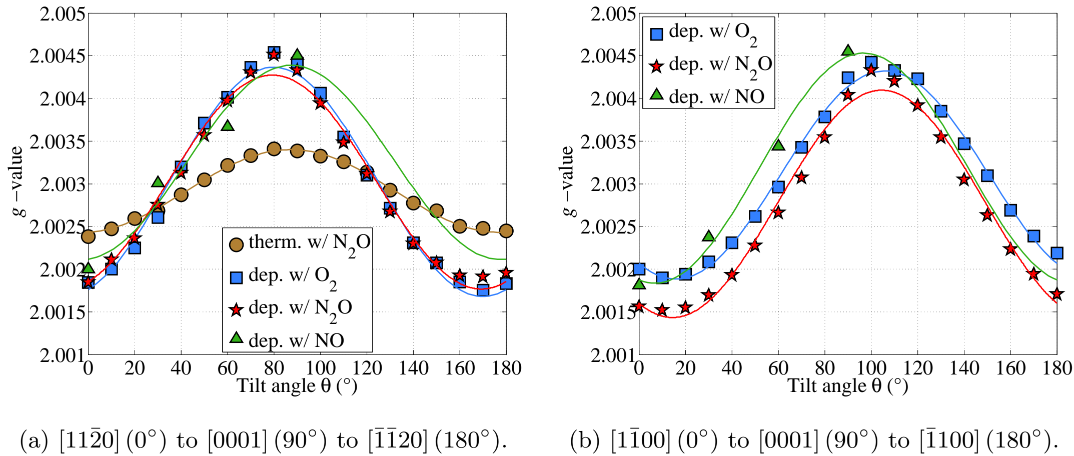

(a) $[11\bar{2}0]$ (0°) to $[0001]$ (90°) to $[\bar{1}\bar{1}20]$ (180°). (b) $[1\bar{1}00]$ (0°) to $[0001]$ (90°) to $[\bar{1}100]$ (180°).

Figure 7.3: Tilt maps of the different MOSFETs.

The results show that all samples have an anisotropic behavior with rotational symmetry (within the experimental error) where the crystalline c-axis is close to the symmetry axis. Sample therm. w/ N_2O has a significantly smaller anisotropy than the other samples. The other samples have a very similar angular dependence. As their device geometry and oxide

Table 7.3: Principal g-factors determined by fitting according to equation (29).

Sample	g_{xx}	g_{yy}	g_{zz}
therm. w/ N_2O	2.0024(4)	-	2.0034(4)
dep. w/ O_2	2.0016(4)	2.0019(4)	2.0045(4)
dep. w/ N_2O	2.0014(4)	2.0018(4)	2.0043(4)
dep. w/ NO	2.0018(4)	2.0021(4)	2.0045(4)

deposition process is identical, it is reasonable to assume, that they contain the same dominant defect. However, the symmetry axis for samples dep. w/ O_2 and dep. w/ N_2O is tilted away from the c-axis by approximately 15° in both measurements. This tilt angle is significantly larger than the 4° off-axis cut of the substrate. This could be an indication for defects at interfacial edge or corner sites playing a role. For sample dep. w/ NO no such tilt is observed. However, this observation has to be taken with care as the measurement of sample dep. w/ NO are less precise due to the noisy spectra and due to the fewer points that were used for the fit. Nonetheless it could indicate that defects at edges and corners might be passivated more efficiently by the NO anneal.

7.3.3 HF structure

The signal of the devices annealed in NO is very small and contains a lot of noise, even after very long signal averaging. The HF structure is hidden within the noise and can, therefore, not be compared to the other devices. As the following measurements only focus on a comparison of the HF structure of the various samples, the sample annealed in NO is left out here. More extensive measurements of NO treated MOSFETs are found in chapter 8.

All measurements were recorded with a magnetic field modulation amplitude of $B_{\mathrm{mod}} = 1\,\mathrm{G}$. Signal averaging was performed until the signal-to-noise ratio reached a reasonable limit in order to compare the main features of the spectra. The measurements of devices therm. w/ N_2O, dep. w/ O_2 and dep. w/ N_2O are shown in Figures 7.4a and 7.4b with $B \| [0001]$ and Figures 7.4c and 7.4d with $B \| [11\bar{2}0]$. For better comparison of the HF structure, the recorded spectra were normalized and shifted to their respective center field. The respective upper graphs show the full spectra and the lower graphs are a $10\times$ magnified view for better comparison of the small intensity HF peaks. Each measurement was performed at a low microwave power of $P_{\mathrm{mw}} < 10\,\mathrm{mW}$ (Figures 7.4a and 7.4c) and a high power of $P_{\mathrm{mw}} \approx 1\,\mathrm{W}$ (Figures 7.4b and 7.4d).

The low power curves show spectra with nicely resolved HF peaks at $\approx \pm 6\,\mathrm{G}$ away from the center line for all samples in the [0001] direction. The same peaks are observed in the $[11\bar{2}0]$ direction with a slightly smaller splitting which indicates a small anisotropic HF component. The relative intensities of these peaks are apparently the same in all samples, despite some small differences due to slightly different linewidths. Apparently, the spectra of samples therm. w/ N_2O and dep. w/ N_2O are broadened at higher microwave power. However, the results from the low power spectra indicate that the dominant defect is likely the same in these devices. A detailed discussion on the origin of this defect is given in section 7.4.

Whether there are any smaller intensity peaks hidden in these measurements is clarified in the high power spectra. Figure 7.4b shows a clearly resolved doublet split by $\approx 57\,\mathrm{G}$ in the devices therm. w/ N_2O and dep. w/ N_2O. This doublet is missing in sample dep. w/ O_2 which is a strong indication that it is due to a different defect. This is supported by the fact that the center of the doublet does not coincide with the center of the dominant peak. This doublet only appearing in the devices annealed in N_2O is further investigated in section 7.5.

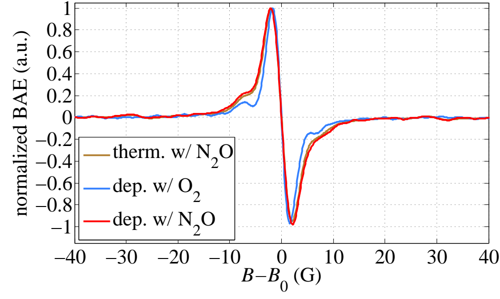

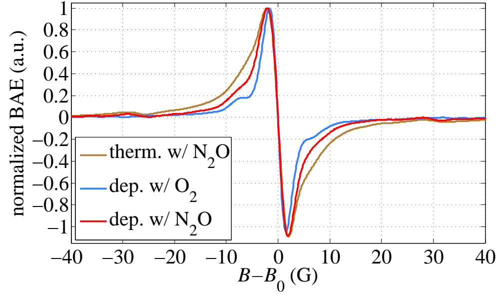

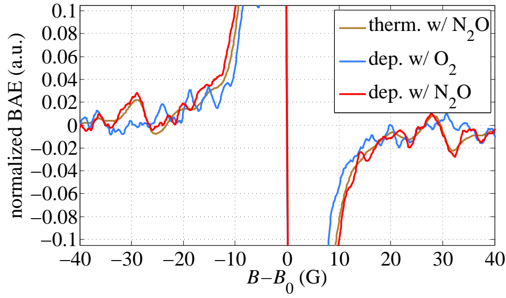

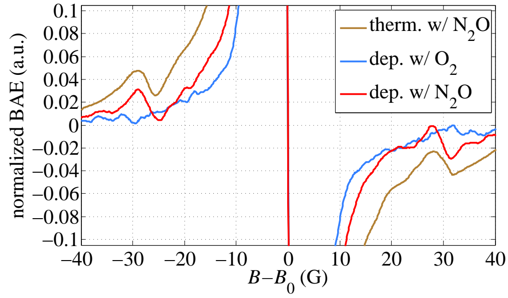

(a) $B \|$ [0001], low power ($< 10\,\mathrm{mW}$).

(b) $B \|$ [0001], high power ($\approx 1\,\mathrm{W}$).

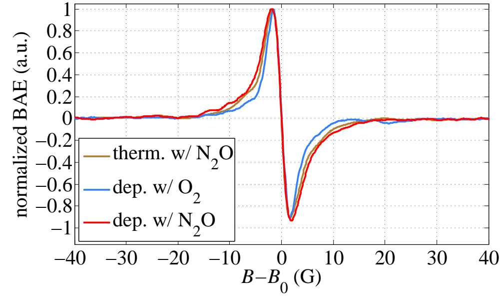

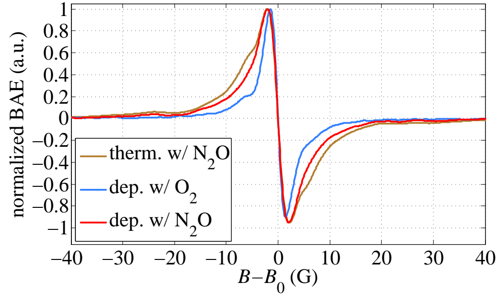

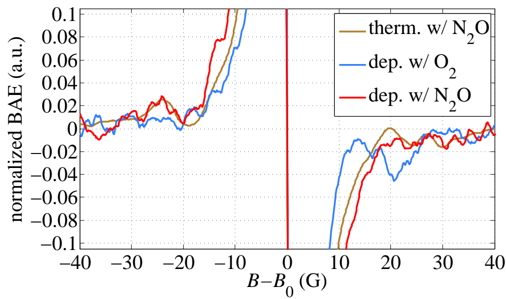

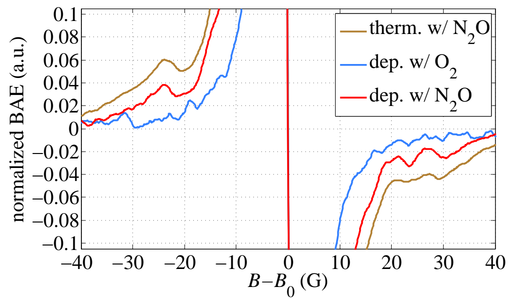

(c) $B \|$ [11$\bar{2}$0], low power ($< 10\,\mathrm{mW}$).

(d) $B \|$ [11$\bar{2}$0], high power ($\approx 1\,\mathrm{W}$).

Figure 7.4: Normalized spectra of different MOSFETs at different microwave power levels with B applied in different crystalline directions, modified from [5].

7.4 Investigation and simulation of the dominant defect

A summary of defects that have been detected with different EPR techniques at the SiC-SiO_2 interface is found in the reference [185]. EDMR studies on comparable SiC MOSFETs have so far associated the observed spectra with the V_{Si} defect [190, 191, 193, 194, 195, 196, 197, 199]. In this section it is shown that the HF structure is better explained by a C dangling bond.

As discussed above, the HF patterns of the studied MOSFETs suggest that all samples likely include the same dominant defect. In an early study conducted in this project a set of transistors with a DMOSFET-like structure were investigated by gated-diode SDR [2]. They had an oxide grown thermally in an N_2O atmosphere. The spectra of the samples dep. w/ O_2, therm. w/ N_2O and the DMOSFET are shown in Figure 7.5a and apparently contain the same prominent HF shoulders at $\approx \pm 6$ G from the center line. It is emphasized that these shoulders look very similar, if not identical, to the ones reported in comparable EDMR studies found in

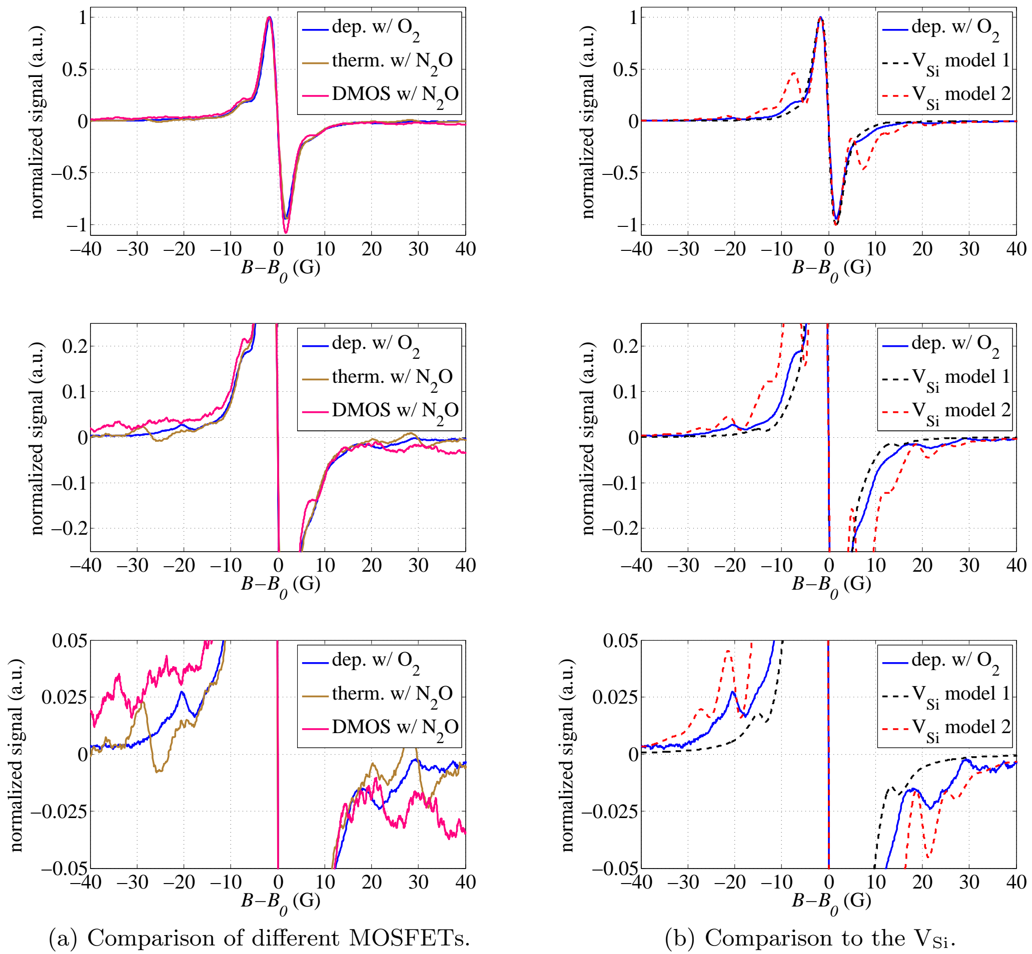

(a) Comparison of different MOSFETs.

(b) Comparison to the V_{Si}.

Figure 7.5: Comparison of the HF structure of the SiC-SiO_2 interface observed in different MOSFETs (a) and a comparison of an experimental curve with the simulations of two models for the V_{Si} [191, 193, 194] (b).

the literature [189, 190, 191, 193, 196, 197, 199]. All those studies reported on an isotropic g-factor of $g \approx 2.0030$ and were interpreted as the V_{Si} defect. This assignment is predominantly supported by the study conducted by C.J. Cochrane et al. where the experimentally observed HF structure was identified as the negatively charged V_{Si} by comparing the experimental data to a theoretical model based on HF parameters from the literature [194]. It is worth noting that in that particular study, unlike the others, EDMR measurements under "fast passage" conditions were conducted (see also [195]), which resulted in a spectrum with somewhat different HF peaks than those of the other studies. The spectrum was well explained by the HF interaction with the four nn1 C and the twelve nn2 Si atoms. The respective HF splitting constants were $a_{C,1-3} \approx 13\,\mathrm{G}$, $a_{C,4} \approx 28\,\mathrm{G}$ and $a_{Si} \approx 3\mathrm{G}$. However, while the V_{Si} seems to be able to explain the spectrum observed under "fast passage" conditions [194, 195] it cannot explain the one observed using a conventional detection scheme, as used in the references [189, 193, 196, 197, 199] which are very similar to those shown in Figure 7.5a. To support this claim the spectrum of the V_{Si} using the HF parameters as described above was simulated with the program described in chapter 4.6.2 and appendix B. In addition a second simulation was conducted based on a qualitative model for the V_{Si}, as suggested in [191, 193]. This model aims to explain the observed peak at $\approx \pm 6\,\mathrm{G}$ in terms of the twelve nn2 Si atoms and the further spread smaller peaks in terms of the four nn1 C atoms. Consequently, the parameters used for this simulation were $a_C \approx 40\,\mathrm{G}$ and $a_{Si} \approx 12\mathrm{G}$, which are matched to the peaks observed in device dep. w/ O_2.

The simulations are compared to an experimental curve in Figure 7.5b and clearly demonstrate that both models for the V_{Si} fail to explain the observed HF peaks at $\approx \pm 6\,\mathrm{G}$. In the first model the peaks are simulated by four C atoms which do not result in a sufficient relative intensity, as the natural abundance of C atoms with $I = 1/2$ is only $\approx 1.11\,\%$. Therefore, this model fails to explain the spectra shown in this work and in the references [189, 190, 191, 193, 196, 197, 199]. Only the experimental curves obtained under "fast passage" EDMR can reasonably be explained by the negatively charged V_{Si} [194, 195]. The second model results in much too high relative intensities which shows that the qualitative model of twelve Si atoms with their natural abundance to be spin $I = 1/2$ of $\approx 4.67\,\%$ cannot explain the spectrum either. Therefore, it is concluded that the observed spectrum is likely not dominated by the isolated V_{Si}.

What is at odds in the measurements presented in this work and those found in the literature is a significant disagreement in the g-factors and their angular dependencies. While the references [189, 190, 191, 193, 196, 197, 199] reported on an isotropic g-factor of $g \approx 2.0030$, all samples in this work have an anisotropic behavior. The samples with the deposited oxide all show a very similar angular dependence with $g_{\parallel} \approx 2.0045$ and $g_{\perp} \approx 2.0018$, independent of the post-oxidation anneal. The sample therm. w/ N_2O has a much smaller anisotropy with $g_{\parallel} = 2.0034$ and $g_{\perp} = 2.0024$. The DMOSFET samples had broadly scattered g-factors with the mean values $g_{\parallel} = 2.0051$ and $g_{\perp} = 2.0029$ [2].

A possible explanation for the different angular dependence of the g-factor could come from the different geometry of the samples. Magnetic fields induced by the device currents could cause a certain offset to the field at the defect sites. However, changing the direction and magnitude of the current gave the same result, which is why this effect was ruled out. Another effect coming from the device geometry is the presence of Ni in the ohmic contacts. Ni is ferromagnetic and might offset the field. In order to clarify the influence of the Ni, further measurements would have to be carried out on different samples. Other studies in the literature also investigated devices with Ni contacts and did not report on any influences [124, 188, 238]. Another plausible explanation is the abruptness of the interface itself. The thermally grown oxide is likely less abrupt than the deposited one. In a very abrupt interface the role

of defects directly at the topmost atomic layer could be more important. Also strain at the interface due to the lattice mismatch between the SiC and the SiO_2 can be an explanation for the anisotropy. This strain is again expected to be higher for the devices with the deposited oxide as the interface is more abrupt. However, at this stage no further understanding about the g-factors can be gained from these samples and it can be questioned, whether the observed values can be trusted. This is why the defect model established in the following predominantly considers the HF structure and only qualitatively discusses the g-factor.

All spectra shown in this chapter contain a well resolved pair of HF peaks at $\approx \pm 6\,\mathrm{G}$. As shown in Figure 7.5b the relative intensity is evidently larger than expected by the V_{Si} model from the reference [194] but smaller than the one from the references [191, 193]. Therefore, a defect containing four C atoms is unlikely the reason for the observed pattern. A defect with a higher number of equivalent C atoms does not seem to be a good model either, even though C clusters at the interface have been suggested as a possible defect model [68]. It is doubtful that a C cluster would contain a sufficient number of *equivalent* C atoms. Additionally, the reported EPR parameters assigned to C clusters do not match with the values observed in the present work [239]. It is more reasonable to explain these peaks by a small number of equivalent Si atoms as ^{29}Si has a higher natural abundance than ^{13}C. For the $N_C V_{Si}$ defect discussed in chapter 6 the Si atoms have a similar splitting as the one observed in the MOSFETs of this chapter. Following this thought a tentative defect model is established below.

In order to investigate the defect apparently dominant in all of the studied n-channel MOSFETs, sample dep. w/ O_2 was studied more carefully. The first step was to get a well resolved spectrum of the $\approx \pm 6\,\mathrm{G}$ peaks. For this reason, the O_2 annealed MOSFET was measured with $B \| [0001]$ where the signal is sharpest. To minimize broadening effects a modulation amplitude of $B_{\mathrm{mod}} = 1\,\mathrm{G}$ and a microwave power of $P_{\mathrm{mw}} \approx 10\,\mathrm{mW}$ was chosen. This spectrum is shown in Figure 7.6a. As this measurement was focused on a narrow linewidth, rather than a good signal-to-noise ratio, it contains a lot of noise which disguises small intensity lines. However, the $\approx \pm 6\,\mathrm{G}$ lines are well resolved and can be simulated by an assumed model of equivalent Si atoms with $a_{\mathrm{Si}} = 12\,\mathrm{G}$. The best match in relative intensity was achieved with a model containing three Si atoms, as shown in Figure 7.6a. This clearly demonstrates that the dominant defect has different properties than the isolated negatively charged V_{Si}, which contains twelve equivalent nn2 Si atoms.

In order to resolve smaller peaks the device was measured again with the same conditions but with increased microwave power of $P_{\mathrm{mw}} \approx 150\,\mathrm{mW}$. This gives the best compromise between linewidth and signal-to-noise ratio. The spectrum is shown in Figure 7.6b and resolves a second pair of peaks at $\approx \pm 19\,\mathrm{G}$ and a much smaller relative intensity, which suggests that they are due to a small number of C atoms. The spectrum was again simulated with three Si atoms and a splitting constant of $a_{\mathrm{Si}} = 12\,\mathrm{G}$ and a slightly increased linewidth, as the spectrum is broadened by the higher microwave power. Additionally, the interaction with C atoms and a splitting constant of $a_{\mathrm{C}} = 38\,\mathrm{G}$ was added to the simulation. The resulting simulated curves for one and for two equivalent C atoms are also shown in Figure 7.6b. The simulated spectrum with two C atoms seems to match the relative intensity of the peaks better at first sight. However, there is more intensity missing in the simulated spectrum which could be due unresolved lines from any neighbors with smaller HF splitting constants that influence the resulting lineshape. Detailed knowledge of such lines is missing and can only be established by DFT modeling. Therefore, a certain error in the lineshape representation cannot be ruled out and the exact number of equivalent C atoms can simply not be extracted with certainty from the simulation at this point.

The electron wave function is less localized at the Si atoms, as they have a smaller HF splitting than the C atom(s). The splitting constants for both the Si and the C atoms are very

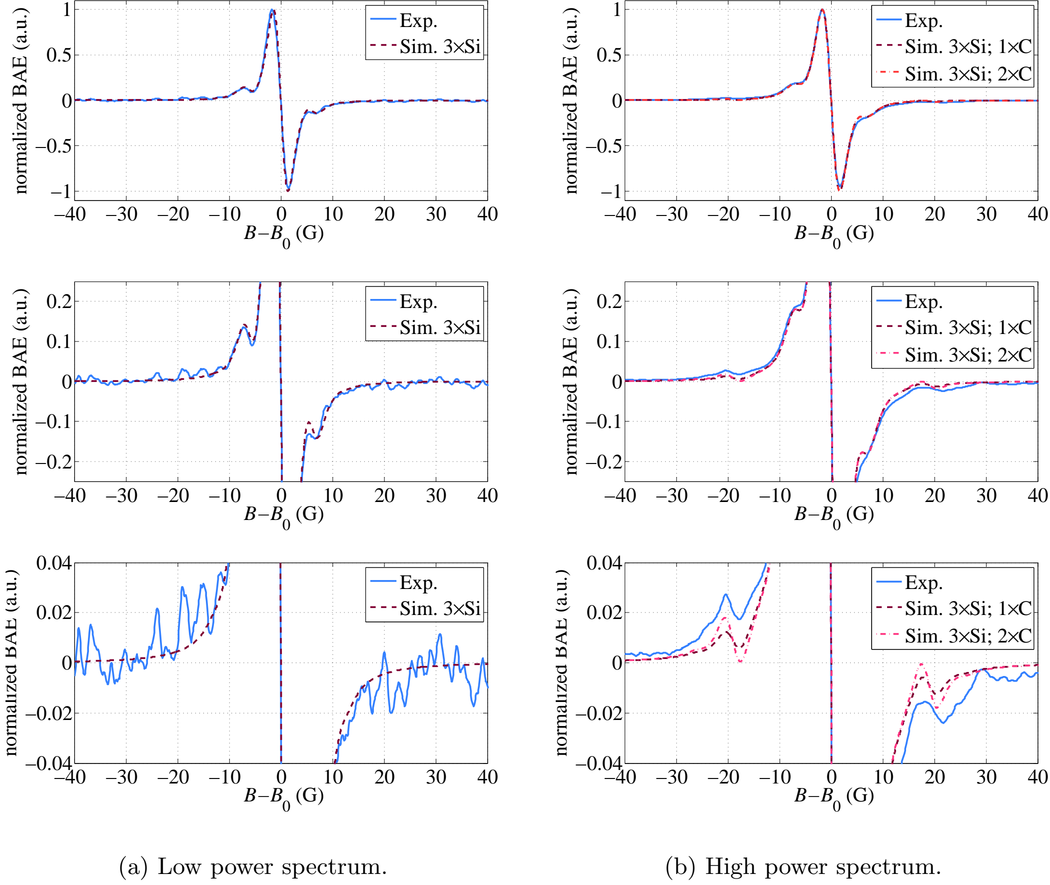

(a) Low power spectrum.

(b) High power spectrum.

Figure 7.6: Normalized experimental and simulated BAE spectra of a O_2 annealed MOSFET (upper), 4× magnified (middle), and 20× magnified (lower).

close to the ones observed for the $N_C V_{Si}$ in chapter 6 where the electron is mostly contained in the C dangling bonds of the defect. By assuming a similar structure a tentative defect model can be created. For the $N_C V_{Si}$ the electron wave function is spread over the three C atoms. Each of them have three Si neighbors. In the MOSFET spectrum, only three Si atoms are present which by analogy would be the neighbors of a single C atom. Therefore, the model that will be assumed for further discussion is that of a C dangling bond defect.

In Si MOSFETs the dangling bond defects have long been identified as the main interface defect [108, 183, 184]. Also for SiC devices C dangling bond-like defects have been observed and are often referred to as P_{bC} centers [110, 111, 112, 113, 186, 187, 188], see also section 1.7.3. When comparing the HF data presented in this chapter to the reported values in a study on oxidized porous SiC there is a good match for both the Si and the C splittings [110]. However, the observed g-anisotropy does not match with the one reported in this work. While for the defects shown here the anisotropy is $g_\parallel - g_\perp \approx 0.0025$, in the referenced study it is $g_\parallel - g_\perp \approx -0.0009$, note the sign. However, this symmetry is only observed for the bond that is aligned with the [0001] axis. On the (0001) surface this bond would point from a C atom down

towards the bulk SiC. Therefore, it is expected that this bond plays a minor role compared to the "planar" C bonds at the (0001) interface. For these bonds, the anisotropy broadly matches the one observed in this thesis, while the exact values do not agree well [110]. A different study that applied EDMR techniques on MOSFETs observed at least a similar anisotropy of $g_{\parallel} - g_{\perp} \approx 0.0016$ which was interpreted as a C dangling bond aligned with the [0001] axis [111]. However, this spectrum can also be interpreted as an average of the "planar" C bonds from reference [110] which would give the right shift of the g-factor. Unfortunately, no HF parameters were reported in that particular study [111]. In another recent study the presence of P_{bC} centers was ruled out based on two assumptions: First that the dominant peak is due to the V_{Si} and second that the g-factors reported in the literature can be reliably compared [189]. Both assumptions can be questioned based on the discussions above.

As the comparison to the literature is unsatisfying and it is doubtful how comparable the samples really are, a tentative model was created from the measured data for device dep. w/ O_2. Figure 7.7 shows a schematic of the Si-face 4H- SiC-SiO_2 interface. The SiO_2 is only sketched, since the detailed structure is not known. The topmost layer of Si atoms are connected with bonds to the first layer of O atoms in the oxide. Note that due to an overlap of the topmost layer of Si atoms in the viewing direction, not all bonds can be sketched correctly. The interface is indicated by the black dashed line.

There are several simple examples of how C dangling bonds may be formed at this interface. (1) is a V_{Si} at the topmost Si layer, which creates three C dangling bonds. As discussed above, the V_{Si} is a commonly reported defect in SiC and it is conceivable that it may also exist directly at the SiC-SiO_2 interface. (2) is a C dangling bond formed as a consequence of relaxations occurring at the SiC-SiO_2 interface. Due to lattice mismatch some distortions and relaxations must be present at the interface which may result in the formation C dangling bonds. (3) is a C dangling bond formed at an edge or corner site. Due to the step-controlled epitaxy processing, many of these sites are present at the SiC-SiO_2 interface. Note that all those examples result in C dangling bonds that reside more or less in the plane perpendicular to the c-axis. It is much less likely for a C dangling bond to be pointing down towards the bulk SiC, as shown in (4), since it would require some restructuring within the bulk SiC. Nonetheless, C dangling bonds aligned with the c-axis exist within other defect complexes, such as the bulk V_{Si}, as indicated by (5). However, none of the known bulk defect complexes characterized by EPR match the measured data.

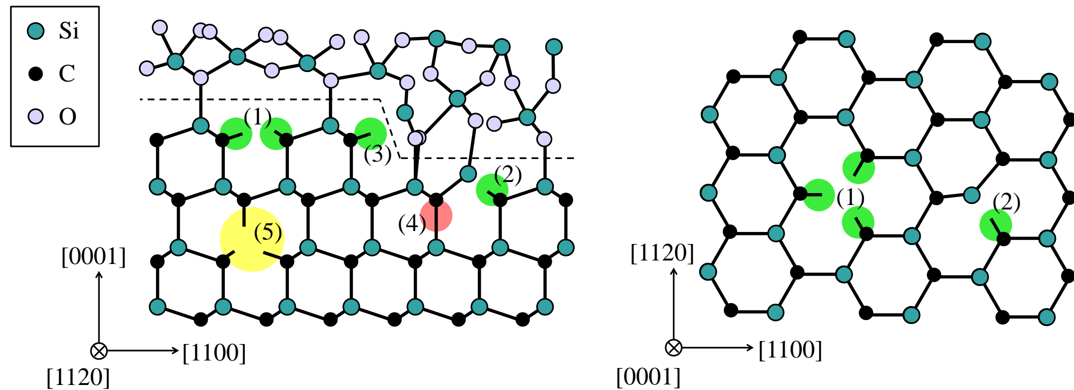

Figure 7.7: Schematic of different examples P_{bC} centers at the Si-face SiC-SiO_2 interface: (1) interfacial V_{Si}, (2) P_{bC} center due to relaxation, (3) P_{bC} center at a corner, (4) C bond pointing downwards, (5) bulk V_{Si}.

While it can only be speculated which of the cases (1)-(3) may be present in the studied devices, they all result in the same possible directions for the C dangling bonds. Note that due to the rotations occurring in the stacking of the 4H-SiC lattice, three additional equivalent C dangling bonds rotated by 60° can be present, but are not shown in Figure 7.7. Therefore, there are in total six arrangements of C dangling bonds which are equivalent upon rotation about the *c*-axis. When assuming the resulting orbitals to have a high p-character then the measured *g*-factor in the *c*-direction is expected to be larger than perpendicular to it [110, 187]. Therefore, the observed anisotropy can be qualitatively explained by C dangling bonds. Moreover, as the interface consists of steps due to the 4° off-axis cut, there are many edges and corners right at the interface. It is reasonable to assume that a certain amount of the C dangling bonds would reside at such sites. As an average over all sites is measured in the EDMR experiments this could be an explanation for the observed symmetry direction being tilted by more than 4°, see also section 7.3.2.

In summary, the model of C dangling bond defects can qualitatively explain the observed spectra. However, the model includes certain assumptions that require confirmation by simulation, as the SiC-SiO_2 interface is a very complex system. First results obtained by extensive DFT simulations that are currently being performed in a joint project by J. Cottom at UCL London show HF parameters that match the ones obtained from the experimental data [240].

7.5 Investigation of the 57 G doublet present in the N_2O-annealed devices

While all samples seem to contain the dominant C dangling bond-like defect, there is an additional doublet separated by 57 G that appears in the samples treated with N_2O, which is clearly visible in Figures 7.4b and 7.4d. Its presence in only these samples is a strong indication that it is due to a different defect. This idea is supported by the fact that the line pair is centered at a different position than the rest of the spectrum. In order to investigate the structure of this additional defect further measurements were performed.

One important question was whether there is a third line in the center and its relative intensity compared to the doublet. As the doublet line only appears in the N_2O-treated samples, a third line of equal intensity lines would strongly indicate a N-complexed defect as N has a nuclear spin of $I = 1$. However, a problem in determining the presence of a third peak, or generally any other smaller peak belonging to the spectrum of the unknown defect, comes from the fact that the dominant defect is much higher in intensity.

Several approaches were tried in order to determine the spectrum of this unknown defect and resolving the question of the presence of a third line. These approaches focused on changing certain measurement parameters where a different dependence of the relative intensities of the two individual defects can be expected. These parameters are the microwave power, the gate voltage, and the measurement temperature. The goal was to find measurement settings where the relative intensity of the 57 G doublet is increased with respect to the center line. Under such conditions a more meaningful interpretation of the structure of this defect could be possible. In the following, the results of the different approaches are presented.

7.5.1 Dependence on the microwave power

As a first approach the dependence of the relative doublet intensity on the microwave power level was investigated, as this is a parameter that is very easily changed in the experimental setup. Every magnetic resonance experiment has a dependence on the photon density inducing

the transitions between the Zeeman levels. When increasing the power, or in other words the photon density, transitions are more likely to happen. However, at a certain power level this effect saturates. For two different types of defects the saturation can occur at different power levels. Consequently, when starting out in full saturation and decreasing the power level, one defect may become relatively lower in intensity at a certain power level. A change of the relative intensities of the overlapping spectra can help to deconvolve them and to reveal the structure of the additional unknown defect observed in the N_2O samples.

A measurement series was conducted where the EDMR response of a MOSFET was recorded at different microwave power levels. As a good signal-to-noise ratio of the small peaks is crucial the device with the highest obtainable signal, namely sample therm. w/ N_2O, was chosen. Figure 7.8 shows the spectra of the device recorded at different power levels. As already discussed above, the spectrum at the highest power is significantly broadened, while this broadening does not play a role for lower power levels. The lowest power where a reasonable signal-to-noise ratio was attained after some signal averaging was $P_{mw} \approx 0.04\,\mathrm{mW}$. However, this spectrum apparently still contains the exact same relative intensity of all peaks. Therefore, changing the power level does not reveal any new insight into the structure of the additional defect as no clear change in the relative intensities was observed at power levels with a sufficient signal-to-noise ratio.

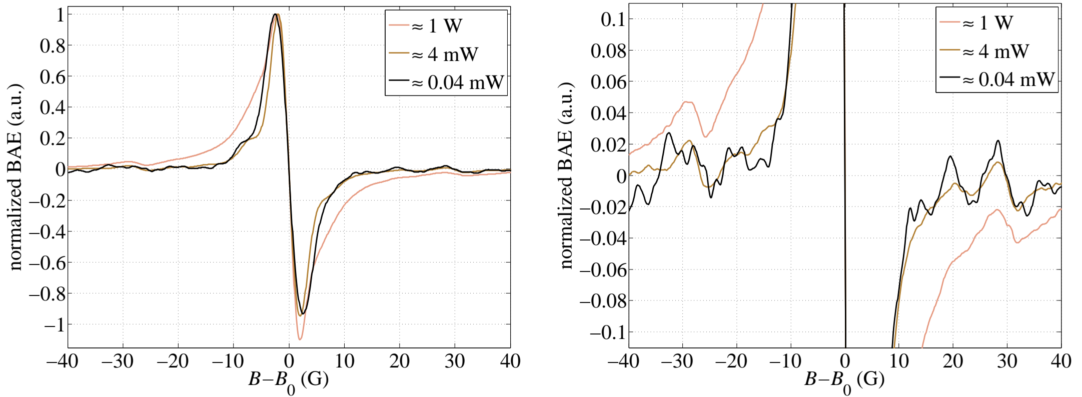

Figure 7.8: Normalized BAE spectra of sample therm. w/ N_2O at different microwave power levels (left), and 10× magnified (right).

7.5.2 Dependence on the gate voltage

Looking at the gate voltage dependence in Figure 7.2a device dep. w/ N_2O seems to show two maxima. This could be an indication for the presence of two different defects that have a different dependence on V_g. The maximum at smaller gate voltage could be the second unknown defect becoming larger in intensity, given that a significant intensity is also contained in its center line. However, as can be seen in Figure 7.2b, the drain current strongly decreases when going below $V_g = 5\,\mathrm{V}$, which makes the measurements extremely noisy. This hinders a good resolution of the low intensity side peaks that are of interest here. Nonetheless, the dependence of the relative intensities of the peaks in the spectrum of this device was investigated by successively going to more negative V_g and comparing the spectra.

In order to obtain a high signal-to-noise ratio the device was measured at the maximum microwave power level of $P_{\mathrm{mw}} \approx 1\,\mathrm{W}$ and a magnetic field modulation of $B_{\mathrm{mod}} = 5\,\mathrm{G}$. Starting at $V_{\mathrm{g}} = -5.5\,\mathrm{V}$ the signal was measured and signal averaging was performed until a sufficient resolution of the 57 G doublet was attained. Then the same was performed at lower gate voltages, as shown in Figure 7.9. As the drain current and also the relative signal intensity decrease, the required signal averaging had to be more extensive. For $V_{\mathrm{g}} = -7\,\mathrm{V}$ about 3000 individual scans were averaged but still no significant change in the relative intensity of the 57 G doublet was observed. This measurement was very time consuming but did not reveal any new findings. Measurements at even more negative gate voltage did not give any further insights as the noise could not be averaged out sufficiently. Therefore, revealing the structure of the unknown defect by changing the gate voltage was deemed impractical. The experiments reported in other studies where the gate was biased far in accumulation could not be reproduced with the studied devices [198].

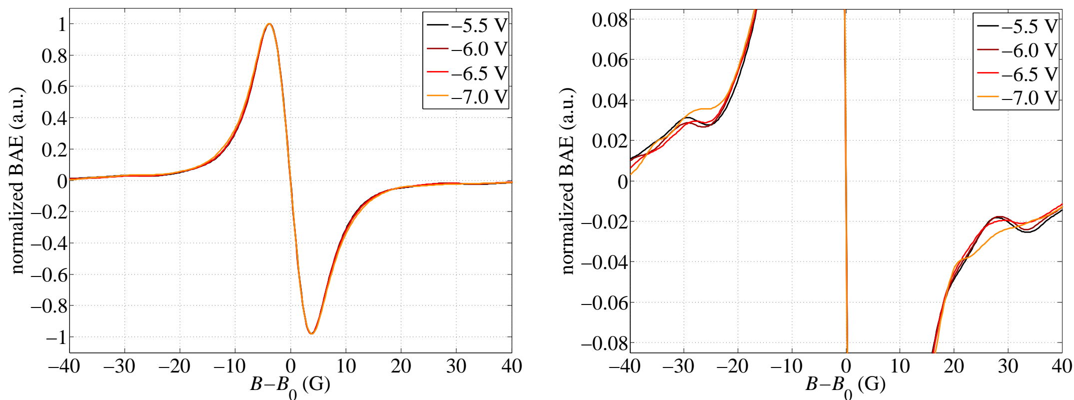

Figure 7.9: Normalized BAE spectra of an N_2O annealed MOSFET at different gate voltages (left), and 12× magnified (right).

7.5.3 Dependence on the temperature

In a recent study applying EDMR on 4H-SiC MOSFETs by M.A. Anders et al. a similar doublet was observed as in the N_2O annealed MOSFETs [198]. It was shown that the relative amplitude of this doublet increased at elevated temperature. The doublet was reported to have a HF splitting of 60 G. As the studied devices are very similar, it is reasonable to assume that the doublet observed by M.A. Anders could be the same as the 57 G doublet observed here. Sample dep. w/ N_2O is equipped with poly-heaters which allow for fast and controlled change of the device temperature [241]. Therefore, this sample was used for studying the effects of elevated temperatures on the relative intensity of the 57 G doublet.

For operation of the poly-heaters a *Keithley 2636A* sourcemeter was set to constant voltage mode while the resistance of the poly-heaters was measured. The temperature can be estimated from the resistance of the poly-heaters using the calibration curve shown in Appendix D. All measurements were performed using a microwave power of $P_{\mathrm{mw}} = 150\,\mathrm{mW}$ and a magnetic field modulation of $B_{\mathrm{mod}} = 1\,\mathrm{G}$. For the elevated temperature measurements longer signal averaging had to be performed as the poly-heater current increased the noise.

The recorded spectra for different temperatures are shown in Figure 7.10. First the device was investigated for several temperatures with the magnetic field applied in the [0001] direction (Figure 7.10a). The results are contrary to expectations, with the relative intensity of the 57 G doublet decreasing with increased temperature, as opposed to the work by Anders et al. [198]. At the highest measured temperature of 180 °C the doublet is already hidden in the noise. When switching off the poly-heaters the doublet is immediately measured again, despite the few minutes that pass for recording enough individual traces to sufficiently average the noise away. This quick reappearance is a strong indication that the elevated temperatures are depopulating the state that is responsible for the 57 G doublet signal while it is repopulated when the temperature is decreased. The same effect was observed for the magnetic field applied in the [11$\bar{2}$0] direction. However, due to a device failure only the 130°C curve was measured. The observed decrease of the doublet at high temperatures suggests that the device should also be measured at lower temperatures, as the doublet signal may increase. This is not possible with the current custom-built setup. However, in a follow-up project the setup has been adapted for low temperature measurements in order to carry out these measurements [217].

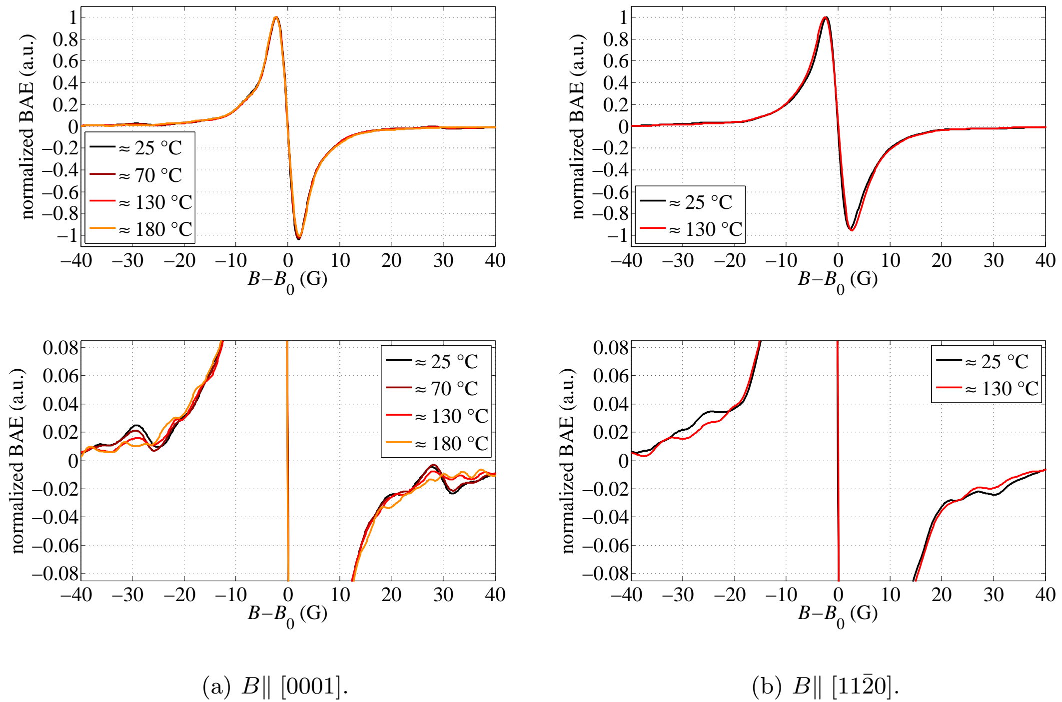

(a) $B \parallel$ [0001].

(b) $B \parallel$ [11$\bar{2}$0].

Figure 7.10: Normalized BAE spectra of an N_2O annealed MOSFET at different temperatures (upper), and 12× magnified (lower).

7.5.4 Simulations

In order to get a better understanding of the changes that occur to the spectra of sample dep. w/ N_2O at elevated temperatures some simulations were conducted. The idea was to subtract the C dangling bond model established for sample dep. w/ O_2 in section 7.4 and to look a

the residuals for the spectra recorded at different temperatures. A spectrum of sample dep. w/ N_2O with the simulated defect model is shown in Figure 7.11a. This model includes one C atom and a splitting of $a_C = 38\,\mathrm{G}$ and three Si atoms with splittings of $a_{Si} = 12\,\mathrm{G}$. For each temperature an individual simulated curve was generated as the linewidths were slightly different and had to be adapted. The residuals of the experimental curves subtracted by their respective simulated curves are shown in Figure 7.11b. It becomes more clear that the 57 G doublet is shrinking at elevated temperatures. In addition to the doublet some intensity close to the center line is changing. A peak positioned at slightly higher field than the center is disappearing along with the doublet. This is an indication for the doublet actually being a triplet. As mentioned above, repeating the measurement at lower temperature could confirm these observations. For now this experiment achieved the closest experimental insight into the nature of the defect associated with the 57 G doublet.

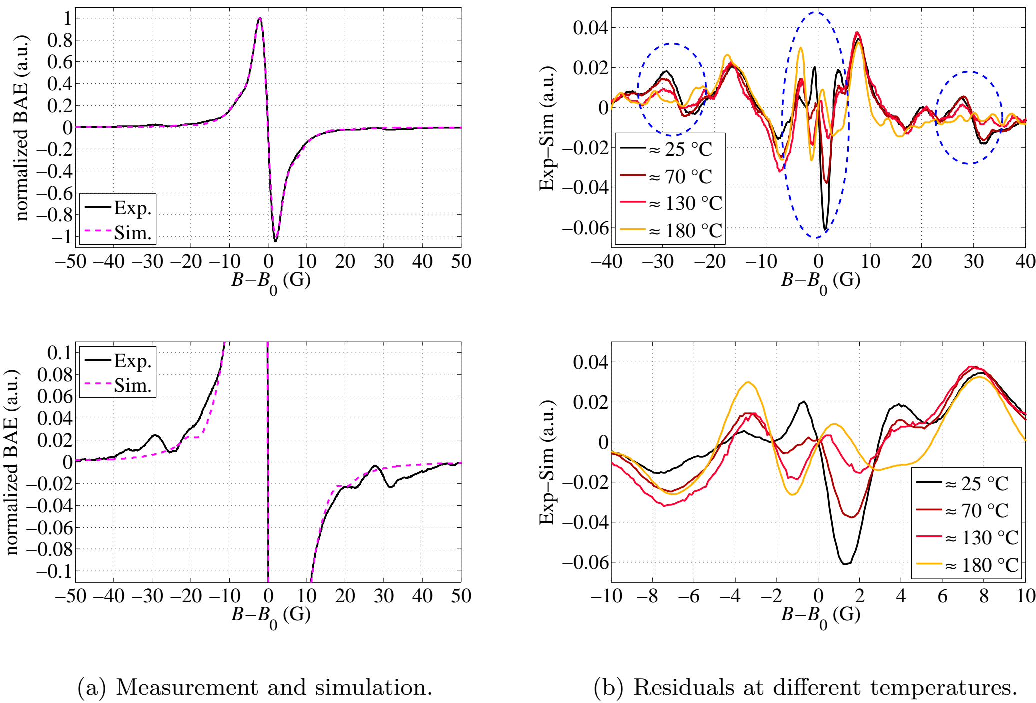

(a) Measurement and simulation.

(b) Residuals at different temperatures.

Figure 7.11: Normalized experimental BAE curve and simulation of sample dep. w/ N_2O with the magnetic field applied in the [0001] direction (a). Residuals of the spectra recorded at different temperatures and subtracted by the respective simulated curve (b).

7.5.5 Tilt series

The above measurements could not increase the relative signal of the 57 G doublet appearing in the N_2O annealed MOSFETs. In order to learn more about the structure of this defect and to demonstrate its independence of the central peak two tilt series were conducted. As the center of the peaks does not coincide with the main peak, it is expected that this defect should also have a different angular dependence than the rest of the spectrum. This can give

a better understanding of its structure. Out of all the devices, sample therm. w/ N_2O has by far the highest relative signal. However, at high microwave power levels significant broadening occurs. This broadening can smear out the spectrum, which makes it more difficult to assign the small intensity lines that are of interest here. Therefore, sample dep. w/ N_2O was chosen to investigate the behavior of the 57 G doublet.

Figure 7.12 shows the recorded tilt series. The measurements were performed at a microwave power of $P_{\mathrm{mw}} \approx 1\,\mathrm{W}$ and a modulation amplitude of $B_{\mathrm{mod}} = 1\,\mathrm{G}$. The devices were rotated with respect to the applied magnetic field B. The graphs on the left show the spectra tilted from the $[11\bar{2}0]$ (0°) to the [0001] (90°) direction in 15 ° steps and the graphs on the right $[1\bar{1}00]$ (0°) to [0001] (90°), respectively. For each measurement about 150 individual traces were averaged in order to improve the signal-to-noise ratio.

What becomes evident is that the spectra are rich in small intensity peaks that make clear assignments difficult. It is not possible to clearly follow the angular dependence of all observed peaks. However, in order to demonstrate how the 57 G doublet is part of an individual defect the positions of the outermost peaks were followed and are shown in Figure 7.13. The top graphs show the positions of the peaks and of the center line of the spectrum. It becomes apparent that the HF splitting of these peaks is only weakly anisotropic with values varying between 48 G and 57 G. The bottom plots show the calculated g-factors for the respective center positions of the doublet for each tilt angle. They were fit by equation (29). It becomes very clear in this plot that the doublet has an angular dependence of the g-factor different from the central peak associated with the C dangling bonds. However, unlike the C dangling bond, the determination of the position of the doublet peaks is very ambiguous which means that not too much confidence should be put in the resulting tilt map.

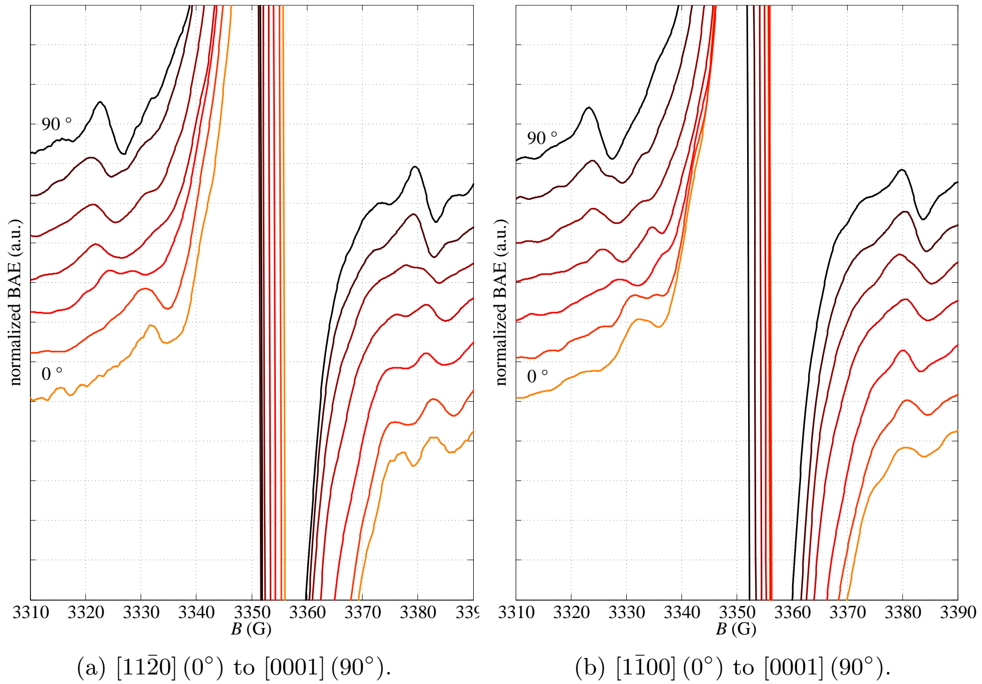

(a) $[11\bar{2}0]$ (0°) to [0001] (90°).

(b) $[1\bar{1}00]$ (0°) to [0001] (90°).

Figure 7.12: Tilt series of an N_2O annealed MOSFET. The spectra are magnified and vertically shifted in order to follow the low-intensity lines.

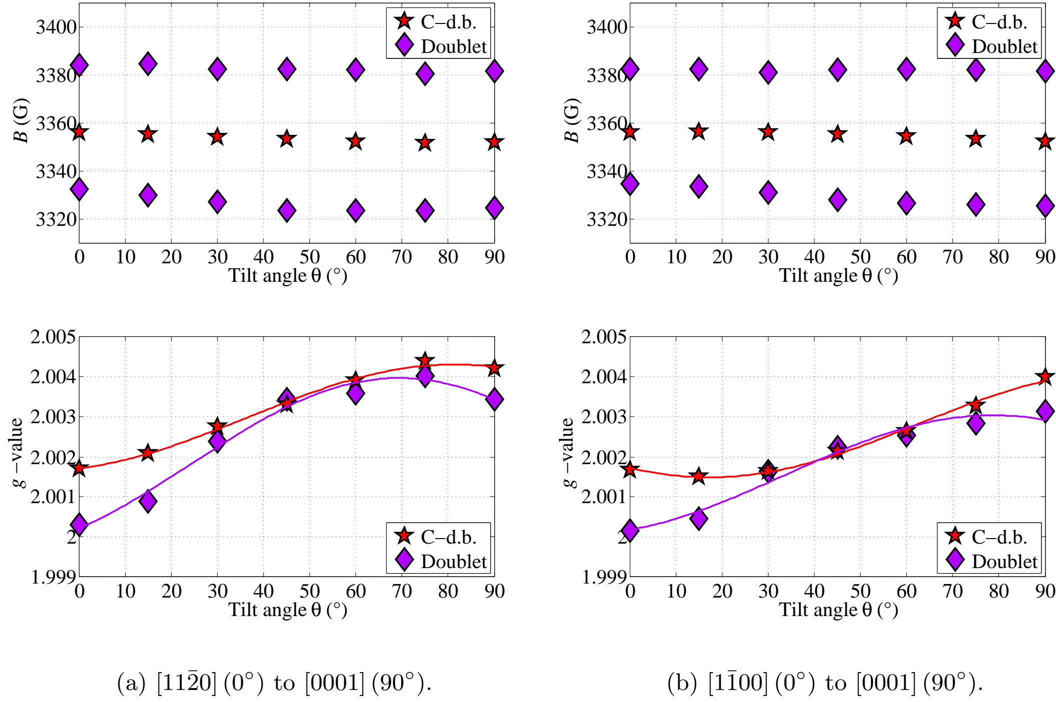

(a) $[11\bar{2}0]$ (0°) to [0001] (90°).

(b) $[1\bar{1}00]$ (0°) to [0001] (90°).

Figure 7.13: Angular dependence of the C dangling bond and the unknown doublet defect.

7.5.6 Discussion

The defect that is observed is best characterized by its close to isotropic peak separation of 57 G. There are a few defects in the literature that have a similar splitting. One of them is the one reported by Anders et al. already discussed above [198]. This defect is characterized by becoming higher in intensity at elevated temperature. As the opposite was observed for the 57 G doublet, this defect is discarded. A different defect associated with the V_{Si} is the T_{V2a} center [163, 164]. This defect is characterized by a high spin state that results in a splitting due to the electron-electron interaction. However, the angular dependence of this splitting is different from the one observed in this thesis [163]. A study focusing on EPR measurements at very low temperature (< 20 K) found a defect with high intensity side peaks split by 54 G [188]. This defect was associated to C dangling bonds coupled to H atoms. The reported principle values of the g-factor are different. Additionally, the samples studied in this thesis were not exposed to any H.

In summary a clear assignment of the 57 G doublet observed cannot be made at this point. It was demonstrated that this doublet is definitely independent from the rest of the spectrum indicating that it is due to an individual defect. As the defect is only present in samples exposed to N_2O it is possibly a N-coupled defect. This is supported by the measurements described in section 7.5.4 that found hints for a hidden third resonance line. However, further measurement paired with simulations will have to be conducted in order to confirm this finding and to identify this defect.

7.6 Summary

The work performed on 4H-SiC MOSFETs with differently processed oxides gives new insights into the structure of the dominating recombination centers at the interface. By using the BAE technique it was possible to measure the EDMR spectra of these defects and to compare the different devices. The results show the same dominating HF signature in all samples. However, differences in the angular dependence of the g-factor were found between grown and deposited oxides. As the HF structure was identical, these differences were associated with different strain environments as the abruptness of the interface for deposited and grown oxides is likely different. Furthermore, an influence of the Ni in the ohmic contacts cannot be excluded.

The defect apparently dominant in all samples was further investigated and simulations of the HF structure were performed. The simulations show a good agreement with the experimental spectra by assuming HF interactions with one C atom with a splitting constant of $a_{\mathrm{C}} = 38\,\mathrm{G}$ and three equivalent Si atoms with $a_{\mathrm{Si}} = 12\,\mathrm{G}$. This resulted in a proposed defect model of C dangling bonds ($\mathrm{P_{bC}}$) at the interface. As the samples were processed at the Si-face of the SiC substrate any C dangling bond would reside more or less perpendicular to the crystalline c-axis, which explains the observed anisotropy. A possible origin of this defect could be the presence of the $\mathrm{V_{Si}}$ right at the interface, as the $\mathrm{V_{Si}}$ is a defect already identified in SiC MOSFETs [194]. A different origin may be the interstitial C pair suggested by theoretical work [91, 103]. This defect is expected to result in two interfacial C dangling bonds [91, 103]. However, the defect model has yet to be confirmed by theoretical simulations which are currently performed by J. Cottom in a joint project with UCL London [240].

A second defect in much smaller intensity was found in devices that received an N_2O anneal. The defect is characterized by a resolved 57 G doublet of small intensity. In order to further resolve this spectrum and to clarify whether there is a third line hidden under the high intensity $\mathrm{P_{bC}}$ spectrum the influences of the gate voltage, the microwave power and the temperature was studied. Unfortunately, none of these measurement series resulted in a better resolved spectrum. However, at high temperature the doublet and simultaneously some small intensity in the center disappears which hints for a third line. As this defect is only found in samples exposed to N_2O it could be a N-containing complex.

Chapter 8

Defects at the SiC-SiO_2 interface of NO-annealed 4H-SiC MOSFETs and the influence of hot carrier stress

This chapter contains investigations of the influences of hot carrier stress (HCS) on the observable EDMR spectra and on electrical parameters of NO-annealed 4H-SiC n-channel MOSFETs. While the studies performed on differently processed MOSFETs described in chapter 7 gave some new insights into the defects dominant in devices annealed with O_2 or N_2O, not much could be stated for the devices that received an NO anneal. The problem was that the observed signal intensities were very small and thus did not reveal the HF structure of the dominant defect. The angular dependence of the g-factor was the only experimentally obtainable result that indicated the presence of the same defect in the NO-annealed devices as in the O_2 and N_2O-annealed ones. However, in a recent related study it was unambiguously shown how HCS can increase the density of interface defects [4]. In order to learn more about this degradation process and the defects present in the NO-annealed MOSFETs, a device was gradually stressed by HCS up to a time of 10^6 s. It was characterized in terms of its EDMR response (via BAE measurements) and electrical parameters were obtained after every stressing step. The electrical characterization showed an increased density of interface defects by a factor of ≈ 2.2 and a simultaneous dramatic decrease in the mobility over roughly five orders of magnitude. At the same time a significant threshold voltage shift was observed. The BAE spectra increased in intensity by a factor of ≈ 27 and are associated to an increased density of the defect already present in the unstressed device. This indicates that the defects that were passivated by the NO anneal can be depassivated by the HCS. In addition to the central peak, some very broad intensity of HF side peaks were found which were tentatively assigned to N. They are likely formed by the N atoms that get depassivated. Most of the study presented here was published in the reference [3].

8.1 Hot carrier stress (HCS)

The degradation of MOSFETs via HCS is a long-known and well-studied effect in Si MOSFETs [242, 243, 244, 245]. HCS occurs when a device is biased in saturation and minority carriers get accelerated along the channel and gain sufficient energy to cause damage in the crystal, resulting in the creation of defects at the semiconductor-oxide interface [242, 243, 244]. The effect predominantly damages the drain side of the channel, as the accelerating electric field is highest in that region under saturation conditions [244, 245]. Simulations of the potential distribution in a Si MOSFET for a constant gate voltage and different drain voltage regimes are shown in Figure 8.1. The channel region is indicated by a black ellipse and the electric field is the gradient of the potential distribution. In the linear region the potential gradually drops over the whole channel. At higher drain voltages the potential drop moves closer to the drain side. It is evident how in the saturation region almost the entire potential drop and, therefore, the electric field is concentrated at the drain side of the channel.

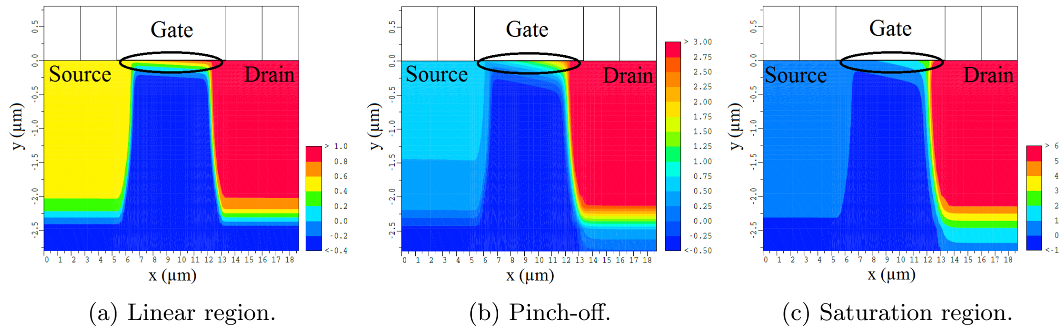

(a) Linear region. (b) Pinch-off. (c) Saturation region.

Figure 8.1: Simulation of the potential distributions in a Si MOSFET in different biasing regimes. Calculations were performed using the minimos-NT 2.1 device simulator [246], courtesy of A. Dorda [247].

While HCS is a well-studied effect in Si [242, 243, 244, 245], there are only a few studies on HCS in SiC [4, 248, 249]. In MOSFETs it was only possible to observe the effects of the stress by electrical measurements a few years ago [249]. The reason for this is that there used to be such a high defect concentration already present in the unstressed devices that the additional defects created by HCS could not be observed. Only improvements in device manufacturing and especially anneals in NO have made it possible for the effects of HCS to be observable. In state-of-the-art devices the effect of HCS has been shown to strongly degrade the device performance [4]. It is emphasized that even though HCS is not going to be an effect relevant for a power MOSFET during normal operation, it may occur when a device is switched or short-circuited. It has been demonstrated that only a few seconds of HCS already have a significant impact on the electrical parameters of a SiC MOSFET [4].

The questions arising are what are these defects that get created under the stress and are they also responsible for the degraded mobility in SiC MOSFETs? It is well established that there is a correlation between the defect density and mobility [75]. In chapter 7 it was shown that all devices, independent of their oxide process apparently contained the same dominant defect, which was assigned to C dangling bonds. Only for the devices annealed in NO a clear assignment could not be made due to the unresolved HF structure. These devices have a very low defect density and the impact of HCS should be well observable in these devices.

8.2 Experimental details

The devices studied in this chapter are identical to the NO-annealed MOSFET from chapter 7. The processing parameters can be found in table 7.1. One device was gradually stressed and for each stress step the transfer characteristics, the charge pumping current, and the EDMR spectrum obtained via BAE (see section 4.4) were measured. The HCS was performed with a drain voltage of $V_\mathrm{d} = 50\,\mathrm{V}$ and a gate voltage of $V_\mathrm{g} = 25\,\mathrm{V}$ applied by a *Keithley 2636A* sourcemeter with the source and body grounded. These stressing conditions were chosen based on the results of a related study on very similar devices where it was reported that the maximum stress occurs when $V_\mathrm{d}/V_\mathrm{g} \approx 2$ [4]. The transfer characteristics were recorded using the *Keithley 2636A*. From the transfer characteristics the mobility and threshold voltage were extracted using the method described in section 3.1 [82]. The charge pumping measurements were performed by pulsing the gate between $-10\,\mathrm{V}$ and $10\,\mathrm{V}$ at a frequency of $100\,\mathrm{kHz}$ using a *Jäger ADwin Pro II* DAC. The duty cycle was $50\,\%$ and the rising and falling slope was $20\,\mathrm{V}/\mu\mathrm{s}$. The charge pumping current was measured using a *Stanford Research SR570* current amplifier.

The BAE measurements were performed at a source voltage of $V_\mathrm{s} = -3.5\,\mathrm{V}$ and a gate voltage of $V_\mathrm{g} \approx -4.5\,\mathrm{V}$. This gate voltage was slightly adapted for each stress step to result in a drain current of $I_\mathrm{d} = 400\,\mathrm{nA}$ out of resonance in order to have a more meaningful comparison of the relative EDMR intensities after stress. All measurements were recorded at a microwave power level of $P_\mathrm{mw} = 200\,\mathrm{mW}$ and a microwave frequency of $f_\mathrm{mw} \approx 9.402\,\mathrm{GHz}$. A magnetic field modulation at a frequency of $f_\mathrm{mod} \approx 800\,\mathrm{Hz}$ was used for lock-in-amplification. Signal averaging of up to a few hundred individual traces was performed for each measurement. All of the above-mentioned measurements were performed at room temperature.

8.3 Results

It was very difficult to find the biasing conditions where the BAE spectrum of the virgin device could be recorded due to the extremely low signal-to-noise ratio. Therefore, a device was stressed with HCS for a time of $\approx 10^4\,\mathrm{s}$. The device was then measured with BAE in order to find the biasing conditions where a good signal-to-noise ratio could be obtained. These were the above-mentioned $V_\mathrm{s} = -3.5\,\mathrm{V}$ and $V_\mathrm{g} \approx -4.5\,\mathrm{V}$. The measurement of the stressed device (pink) compared to a virgin device (green) is shown in Figure 8.2. The spectra were recorded at modulation amplitude of $6\,\mathrm{G}$. It is evident how the stress results in an increased signal intensity. When the spectrum of the stressed device is recorded with BAE by injecting the carriers from the drain side and measuring the current at the source side the observed signal (black) is the same as in a virgin device. This observation can be understood as follows.

A BAE measurement takes advantage of the fact that the channel length is comparable to the diffusion length [197]. Only a small number of carriers initially injected from one side of the channel will reach the other side and are able to contribute to the measured current. This small current is strongly influenced by recombination centers along the diffusion path. HCS is known to mostly damage the region close to the drain side of the channel [244, 245]. When the carriers are injected from the source side they first face a practically undisturbed zone until they reach the highly defective drain side. The high concentration of recombination centers just before these carriers can reach the drain side will result in the recombination of a large fraction of these carriers. Under resonance, the recombination rate changes resulting a high relative signal. When the current direction is reversed by switching out source and drain the injected carriers will first face the largely defective drain side. The injection current floods this region with carriers. Even though this region contains a high concentration of recombination

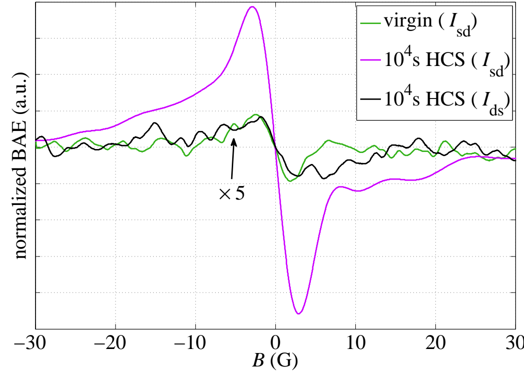

Figure 8.2: Comparison of the BAE signals of a virgin device and one that received HCS. For the latter the BAE measurement was once recorded at the drain with carrier injection from the source (pink) and once vice versa (black).

centers many of the carriers will be able to diffuse on towards the source side. However, like in the other case, only small number of these carriers will actually reach the source side due to the channel length. These remaining carriers will face a practically virgin device and therefore only a small fraction of them will recombine. Under resonance this results in a significantly smaller relative current change (close to that of a virgin device) than in the other case.

As the feasibility of creating spin dependent recombination centers through HCS was established with these preliminary measurements, a stressing series on a virgin device was conducted. The device was gradually stressed for 10^3 s, 10^5 s, and 10^6 s and for each step the electrical parameters and BAE spectra were recorded. Figure 8.3a shows the recorded transfer characteristics for the various stressing steps. The curves for the virgin device and after 10^3 s of HCS were recorded with a drain bias of $V_\mathrm{d} = 0.1\,\mathrm{V}$, the one after 10^5 s with $V_\mathrm{d} = 1\,\mathrm{V}$, and the one after 10^5 s with $V_\mathrm{d} = 5\,\mathrm{V}$. The increase of the drain voltage was necessary due to the extreme flattening of the transfer curves and an accompanied threshold voltage shift. The low-field mobility μ_LF as well as the threshold voltage shift ΔV_th were extracted using the method described in section 3.1 [82]. The respective values are found in table 8.1. The mobility drops over several orders of magnitude with the stress. This confirms the severe degradation of the HCS reported in the literature [4]. However, as the extraction model is based on a measurement of the transfer characteristics in the linear region, the increased V_d for the longer stressed curves may underestimate the mobility. Additionally, a significant shift of the threshold voltage is observed. Therefore, a severe effect on the HCS on the device performance is evident. The charge pumping measurements for the respective stress steps are shown in Figure 8.3b.

Table 8.1: Experimental parameters determined for the measured MOSFET after different stress times [3].

Stress time (s)	μ_LF $(\mathrm{cm^2V^{-1}s^{-1}})$	ΔV_th (V)	I_cp (nA)	$\Delta I/\Delta I_0$	$g_{B\parallel c}$	$g_{B\perp c}$
0	12.7	0	54	1	2.0045 (4)	2.0020 (4)
10^3	0.218	1.8	67	2.6	2.0053 (4)	2.0020 (4)
10^5	0.022	3.9	77	21.9	2.0060 (4)	2.0020 (4)
10^6	0.0003	4.0	120	27.3	2.0059 (4)	2.0019 (4)

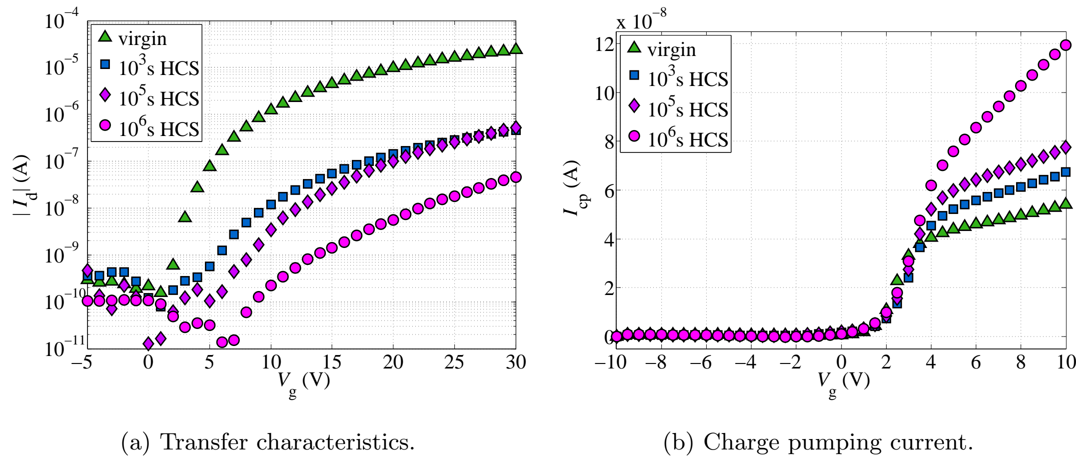

(a) Transfer characteristics.

(b) Charge pumping current.

Figure 8.3: Electrical measurements after different stress steps.

It is evident that the charge pumping current I_{cp} increases which corresponds to an increase of the defect density. Unfortunately with the equipment available for these measurements the gate voltage could only be pulsed between $\pm 10\,\text{V}$ which is apparently not sufficient to reach saturation in the charge pumping current. However, the measurements are still useful for a qualitative comparison. The maximum charge pumping currents are listed in table 8.1.

The evolution of the BAE spectra with HCS is shown in Figure 8.4a for B applied in the [0001] direction ($B\|c$) and in Figure 8.4b for B applied in the $[11\bar{2}0]$ direction ($B\perp c$). The spectra have been scaled according to the integrated intensity ΔI of each curve, which was determined by the double numerical integration of the measured curves. The respective values normalized to the unstressed integrated intensity ΔI_0 are listed in Table 8.1. The increase in intensity corresponds to an increase of the density of spin-active recombination centers in the channel region of the device. The spectra were recorded at a magnetic field modulation of $B_{\text{mod}} = 6\,\text{G}$ in order to achieve a meaningful signal-to-noise ratio, especially for the virgin device. Therefore, the spectra are broadened by overmodulation. Nonetheless, it can be observed how some additional broad side shoulders occur with stress time. The g-factors of the recorded curves are also listed in table 8.1. There is a significant increase for $g_{B\|c}$ with HCS while $g_{B\perp c}$ stays constant. A comparison of the angular dependence of the g-factor recorded for the virgin device and after $10^6\,\text{s}$ of stress is shown in Figure 8.5.

8.4 Discussion

The results clearly show how all measured parameters are subject to significant changes after HCS. The most indicative numbers here are the integrated intensity ΔI increased by a factor of 27.3 and the increased charge pumping current I_{cp} increased by a factor of 2.2 after the longest stress period of $10^6\,\text{s}$. Both numbers show that there is a significant defect density created at the interface. The disagreement in the magnitude of these numbers can be explained by the fact that the stress mostly damages the region close to the drain. As discussed, the BAE is sensitive particularly to this highly stressed region. The charge pumping measurement averages the defect density over the whole channel area and therefore results in a smaller relative current change.

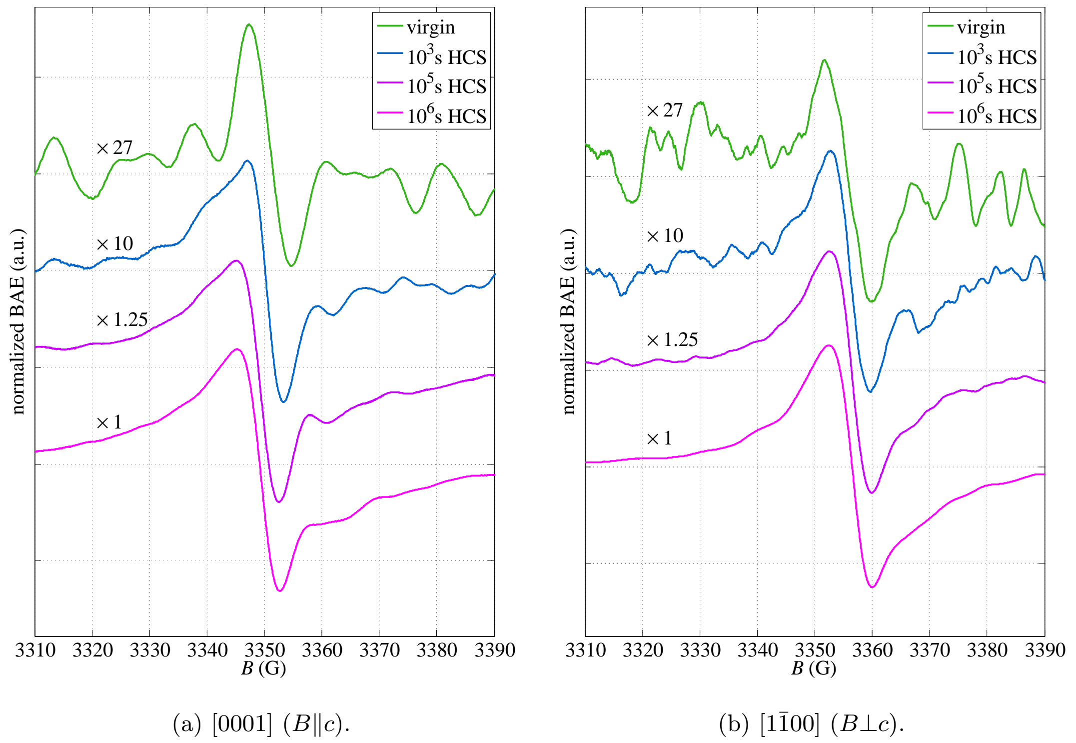

(a) [0001] ($B \| c$).

(b) [1$\bar{1}$00] ($B \perp c$).

Figure 8.4: Normalized BAE spectra of an NO-annealed SiC MOSFET after different times of HCS with B applied in different directions (modified from [3]).

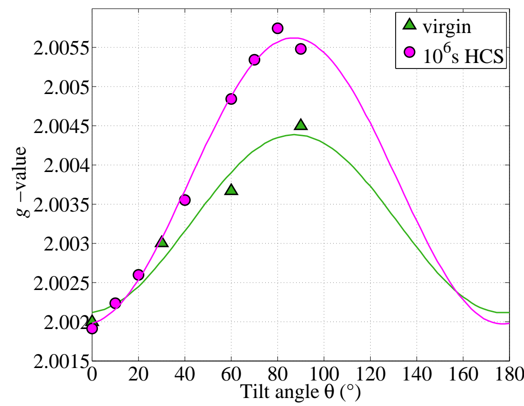

Figure 8.5: Tilt map of the virgin MOSFET and after 10^6 s if HCS. 0° corresponds to B applied in the [11$\bar{2}$0] direction, and 90° to the [0001] direction.

In terms of the measured g-factors it is remarkable that $g_{B\perp c}$ stays constant while $g_{B\parallel c}$ is subject to a significant shift. The former is an indication that a significant part of the newly created defect density contains the same defect present in the virgin device while the latter suggests the creation of a new defect. However, as the defect density is mostly created in the highly damaged drain region disorder or strain could play a role in the observed change of the g-factor. In a recent EDMR study some indications for disorder were found in SiC MOSFETs [199].

The defect present in the device before stress is likely the defect associated to C dangling bonds, as discussed in chapter 7. In order to get a better understanding of the stressed device, the spectra after 10^6 s were recorded with a modulation amplitude of 1 G in order to reduce line broadening. The spectra are shown in Figure 8.6 where they are compared to those of the $N_C V_{Si}$ (see chapter 6), and MOSFETs with an identical geometry annealed with O_2 and N_2O, respectively (see chapter 7). The spectra of the stressed MOSFET contain a narrow central peak with a similar linewidth as the reference spectra. Additionally, there is a broad intensity of side peaks extending over some tens of Gauss left and right of the center.

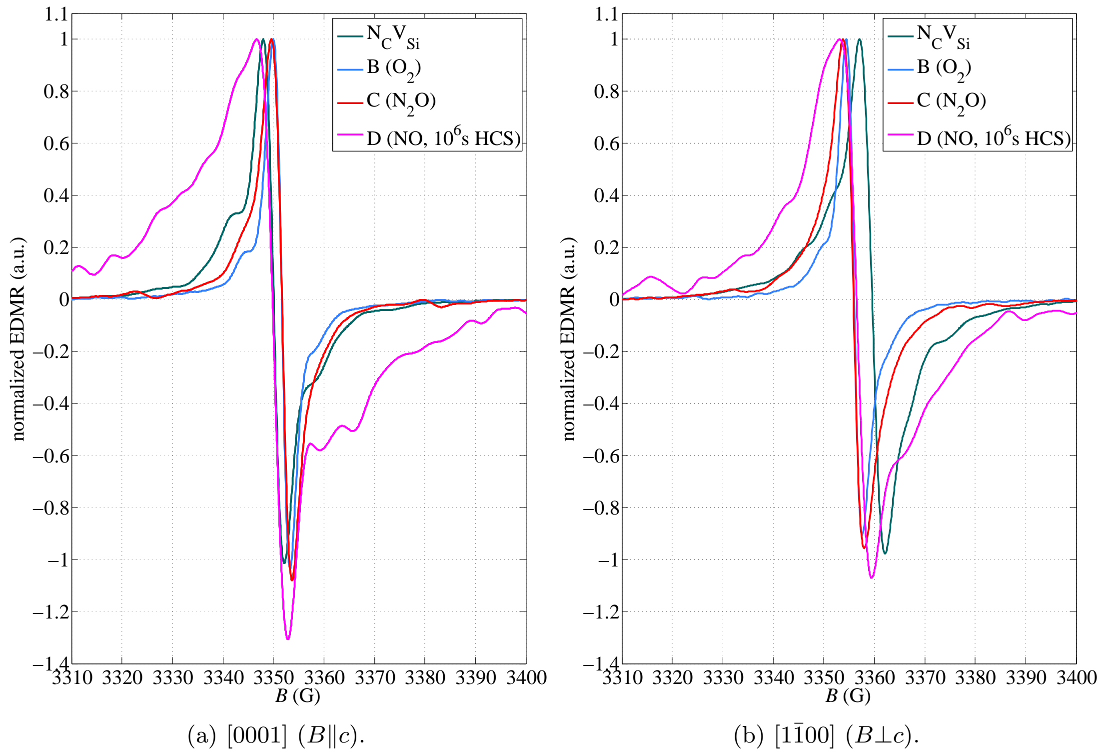

(a) [0001] ($B\parallel c$).

(b) $[1\bar{1}00]$ ($B\perp c$).

Figure 8.6: Comparison of the BAE spectra of the 10^6 s stressed MOSFET with reference spectra from chapters 6 and 7.

The central peak seems to be dominated by the defect associated with C dangling bonds, as it is very close to the reference peaks. It is plausible that defect sites at the interface that were formerly passivated during the NO anneal got depassivated by the hot carriers by impact ionization. This would result in an increased intensity of the initial defect. The shift of $g_{B\parallel c}$ might simply come from the fact that the defects created during HCS are created close to the highly N-implanted drain region. Strain or disorder in that region could be a reason for

the observed shift. However, there might also be some intensity of the $N_C V_{Si}$ present, as the spectrum of the stressed MOSFET is slightly shifted towards the g-factor of this defect. The drain region contains a lot of N_C centers from the n-type doping. The HCS might be capable of damaging the crystal sufficiently to create $N_C V_{Si}$ centers. However, this would mean that Si atoms would have to be removed from their sites which does not seem very likely. Additionally, there should already be a large intensity of $N_C V_{Si}$ present in the heavily N-implanted drain region (see also chapter 6) which is not observed in the BAE measurement of the virgin device.

What is evident is the presence of an additional very broad intensity away from the center line after HCS. None of the defect models established in the prior chapters can explain these side shoulders. A distribution of g-factors resulting from disorder would unlikely be spread over such a wide range of magnetic fields. Therefore, it is more plausible to associate the broad side shoulders to HF peaks (possibly combined with some distribution of g-factors). There is no significant concentration of H expected to be present in the studied device and the Al concentration in the body is orders of magnitudes lower than the N concentration at the drain. Therefore, the most reasonable candidate atom species causing such large intensity HF peaks is N. This would also fit to the model of N-passivated interface defects being depassivated by the HCS, as the N atoms would likely form some other defect complex in the stressed region. However, no specific model for such a defect can be concluded out of the experimental data due to the extremely broad peaks.

8.5 Summary

This study clearly showed how HCS creates defects at the SiC-SiO_2 interface of a MOSFET resulting in strongly degraded electrical parameters. The mobility extracted from the transfer characteristics is decreased over approximately five orders of magnitude after 10^6 s of HCS indicating a severe damage created by the hot carriers. The density of interface defects determined by charge pumping increases by a factor of ≈ 2.2 which is an average value over the whole channel area. The relative signal intensity of the recorded BAE spectra increased by a factor of ≈ 27 which is explained by the creation of a large defect density predominantly in the drain region. The spectra suggest that a significant amount of the created defect density is likely related to the initially smaller intensity of defects observed in the unstressed device and assigned to C dangling bonds. A shift that occurs in the observed g-factor after the stress is explained in terms of strain and/or disorder, as the stress creates defects close to the highly damaged drain region. An additional broad intensity of side peaks is tentatively assigned to HF interactions with N. The mechanism suggested for the degradation due to HCS is a depassivation of defects at the interface that were formerly passivated by the NO anneal.

Chapter 9

TEM investigations of the 4H-SiC-SiO_2 interface

There are several TEM studies in the literature aiming to clarify the interface structure and the processes responsible for the mobility degradation and D_{it} of the SiC-SiO_2 interface of SiC MOSFETs. However, there seems to be a large disagreement in the most important conclusions made in those studies. While some of them applied chemical analysis by EELS and clearly reported an increased C concentration at the interface regions [88, 89, 116], others did not find any C excess [94, 95, 96, 100, 118, 119, 250]. What all studies have in common is that there is a region in which the chemical composition gradually changes from SiC to SiO_2. However, the values reported for the thickness of this region range from 1.5 nm up to 25 nm [89, 120]. Some studies reported on a correlation between this thickness and the mobility [89, 95], while other studies found a contradicting trend [119, 120]. It was speculated whether the disagreement in the literature depends on the specific samples and/or methods used [96]. There is certainly a large variety of oxidation processes and substrates used for the sample manufacturing. Also the preparation of the lamellas as well as the microscopes and detectors used for the TEM and EELS measurements may be different. Therefore, it is doubtful how comparable these studies are to each other and to the MOSFETs described in this thesis.

As the literature is not very satisfying and it is unclear which of the conclusions hold true for the samples studied in this thesis, STEM and EELS measurements were performed on those samples. This chapter summarizes the measurements performed at the SiC-SiO_2 interface of the SiC MOSFETs described in the previous chapters. Two samples with different POAs (O_2 vs. NO) and very different mobilities were compared as they would most likely reveal structural differences responsible for the mobility degradation. The measurements aimed for a thorough acquisition and comparison of experimental data obtainable by STEM and EELS in order to find a final answer to what the major differences are that are responsible for the mobility degradation. The most significant difference that was found by STEM combined with EELS was an increased N concentration in the device that received an anneal in NO. Only insignificant differences were found in the surface morphology and transition layer thickness and no C excess or non-stoichiometric layer was observed. All described measurements were performed at the Austrian Centre for Electron Microscopy and Nanoanalysis (FELMI-ZFE) as part of an ongoing research project [225, 251]. The sample preparation was performed by M. Dienstleder and the STEM and EELS experiments were conducted by C. Gspan.

9.1 Experimental details

The studied samples were fully processed 4H-SiC MOS capacitors formed on a *p*-doped substrate. The oxide was deposited in a CVD process identical to the MOSFETs described in chapter 7. The two samples only differed in terms of the POA: one sample received a short anneal in O_2 while the other received a thorough anneal in NO. As discussed in the previous chapters, these samples differ strongly in terms of their electrical properties as well as their defect concentrations at the interface, which is summarized in table 9.1. Consequently, these samples are ideal for comparing the interface structure and to search for differences in their interface morphology, chemical composition and transition layer thickness.

Table 9.1: Device properties determined by electrical measurements of the studied samples, more details on these devices are found in chapter 7.

Sample	μ_{LF} $\left(\mathrm{cm}^2\mathrm{V}^{-1}\mathrm{s}^{-1}\right)$	D_{it} $\left(\mathrm{cm}^{-2}\mathrm{eV}^{-1}\right)$
w/ O_2	0.2	2.3×10^{12}
w/ NO	17.6	2.9×10^{11}

After chemical removal of the metalization, thin lamellas were cut out of the MOS capacitors using a *FEI NOVA200* focused ion beam (FIB) [225]. The lamellas were prepared so that the viewing direction is the $[1\bar{1}00]$ direction. This direction is parallel to the step bunching caused by the off-axis growth [14]. The lamellas where further thinned by ion polishing and ultimately received a soft polishing using a *Fiscione 1040 NanoMill* ion mill [225]. This tool allows for a very low angle and low energy ($E = 500\,\mathrm{eV}$) polishing and removes contamination and damage caused by the previous ion polishing steps. The lamellas are shown in the STEM images in Figure 9.1. The thinned areas are clearly recognized by the fringes due to sample bending. The sample thickness varies, as the ion polishing steps are not uniformly taking away material from the samples, and was estimated to be $\approx 20 - 50\,\mathrm{nm}$ by a t/λ analysis [252].

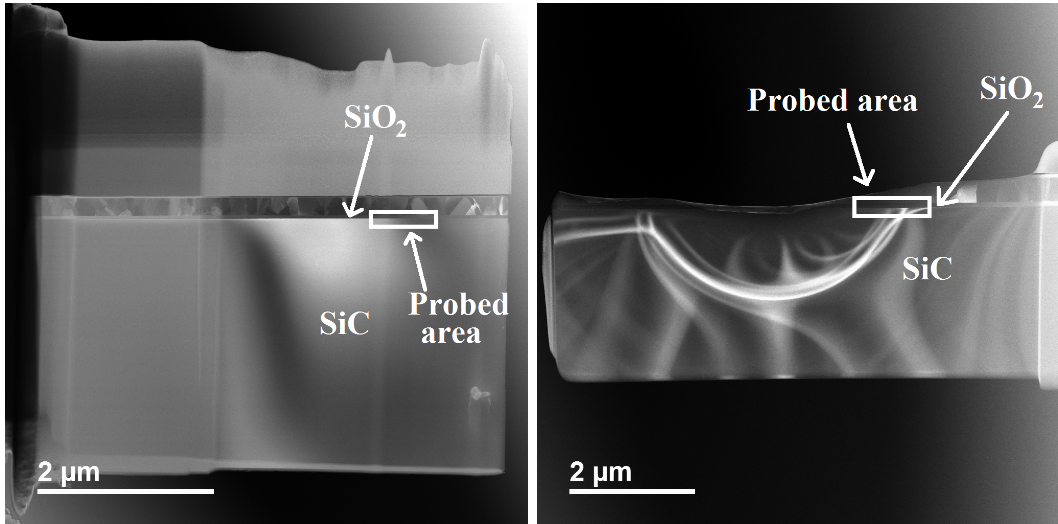

(a) Lamella w/ O_2. (b) Lamella w/ NO.

Figure 9.1: Overview ADF images of the studied lamellas.

All measurements were performed using a *FEI Titan*[3] *G2 60-300* transmission electron microscope with a C_s probe corrector allowing for high resolution STEM imaging [225]. All measurments were conducted using the STEM mode with an acceleration voltage of 300 keV and a spatial resolution of 0.7 Å. The microscope is equipped with different detectors allowing for BF, ADF, and HAADF imaging [225, 226, 227].

EELS was performed using the "Dual EELS" mode which allows for the simultaneous recording of the zero-loss peaks as well as the energy loss region of interest. EELS spectrum images were recorded in predefined 2D windows across the SiC-SiO_2 interface. The energy dispersion of the measurements was 0.25 eV and the pixel size was 0.25 nm. In order to avoid spacial drifts of the sample during long measurements a drift correction was made after the recording of every line of the 2D window.

9.2 Interface morphology

As a first step the interface morphology of the two samples was compared. Figure 9.2 shows high resolution STEM images of the interface region. The interface appears quite sharp in these images and the macrosteps due to the step bunching as well as the bilayer steps that make up the macrosteps are clearly revealed. Therefore, the length and height of the steps could be determined from the STEM images. In order to learn more about the distribution of the step lengths and heights a series of images was recorded for both samples. Figure 9.3 indicates how the length and height of the steps were determined. The length was measured as the distance between the first bilayer step of two neighboring plateaus, where possible. The height was simply measured by counting the number of bilayer steps between two plateaus. The results are shown in the histograms in figure 9.4.

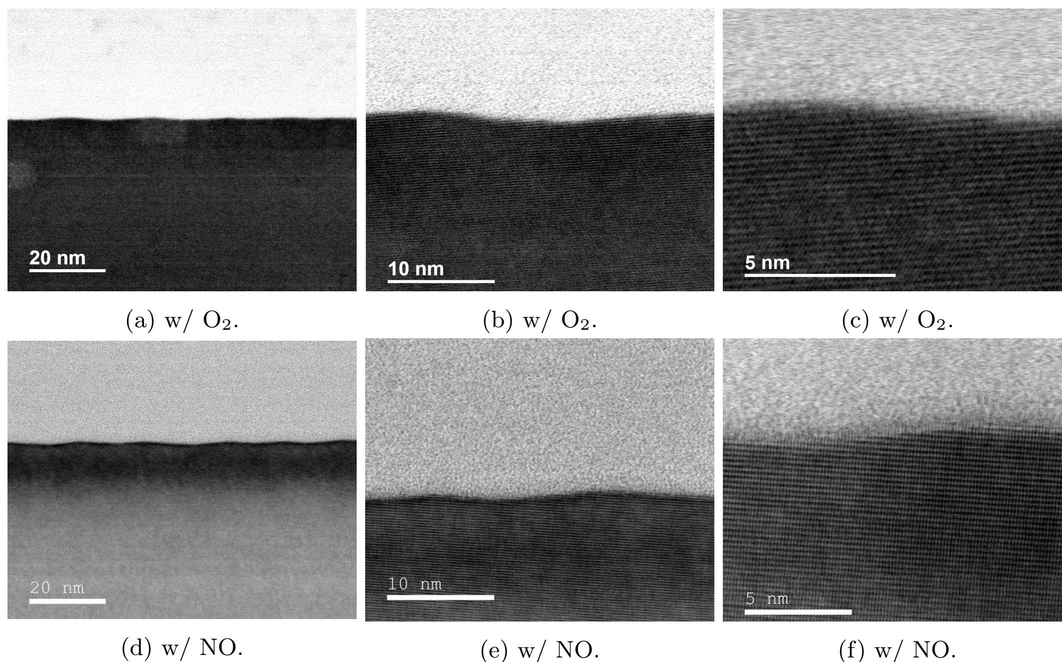

(a) w/ O_2. (b) w/ O_2. (c) w/ O_2.

(d) w/ NO. (e) w/ NO. (f) w/ NO.

Figure 9.2: High resolution BF images of the SiC-SiO_2 interface at different magnifications.

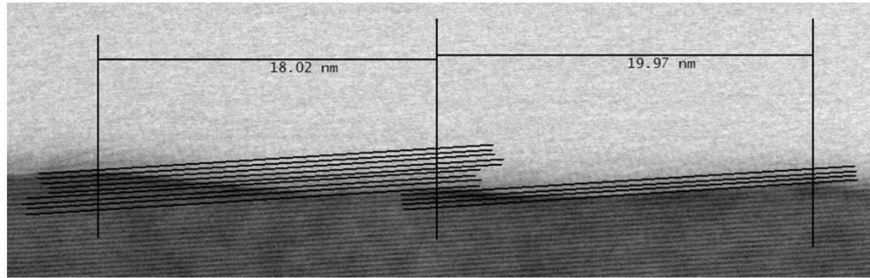

Figure 9.3: Measurement of length and height of a macrostep.

Figure 9.4a compares the length of the steps for the two samples and shows a very broad distribution for both of them. The distributions where fit to Gaussian distributions indicated by the black lines. For the sample with O_2 the mean value of the length distribution is $\approx 20\,\text{nm}$ while it is $\approx 17.5\,\text{nm}$ for the sample with NO. It has to be noted that the measurement has a certain error since it is not always clear where each plateau starts. What is more important than the mean values of the steps lengths is the fact that their distributions are very broad. A Welch's t-test [253] does not reject the hypothesis that the distributions may have the same mean value, as the resulting P-value for the sampled data is $P \approx 23.5\,\%$. For both cases the full width at half maximum of the length distribution is $\approx 10\,\text{nm}$, which indicates a high level of disorder. This can also be interpreted as roughness that may cause scattering [94].

The distributions of the step heights are shown in figure 9.4b. Due to the higher magnification of the images for the measurement of the step heights only 15 individual steps were evaluated for each sample. The histograms are very similar for both samples and clearly show that heights of 4 and 6 bilayer steps (i.e. even numbers) are far more frequently found. This indicates that there is a tendency for two neighboring plateaus to be equivalent in terms of symmetry, i.e. they both are h or they both are k, which has also been reported in the literature [48, 49, 50]. A Welch's t-test for this sample results in $P \approx 48.8\,\%$. Again, the broad distributions indicate non-uniformity, i.e. roughness for both samples.

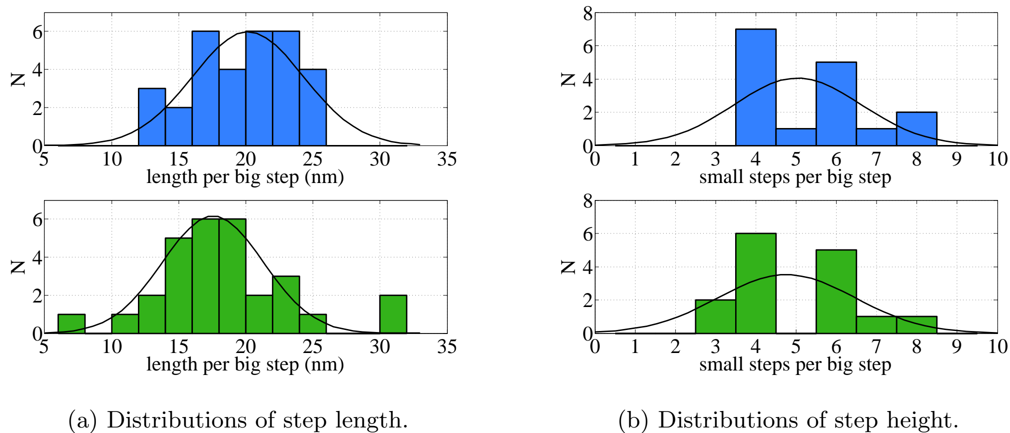

(a) Distributions of step length.

(b) Distributions of step height.

Figure 9.4: Step distributions for O_2- (upper) and NO-annealed sample (lower).

In summary both samples show a very rough and disordered interface indicated by the broad distributions of the step lengths and heights. No clear difference between the two samples in terms of the roughness was found in the described measurements. As a consequence, interface roughness is ruled out as the reason for the significant differences in the electrical properties of the two samples. This means that the reason for the low mobility must be on a smaller scale that cannot be directly found in the high resolution images. In order to learn more about the interface structure chemical information was acquired by EELS, as described in the following.

9.3 EELS characterization of the interface

The EELS measurements aimed to answer three basic questions: What is the interface thickness and are there any differences for the two samples? Is there any C excess at the interface, particularly in the sample with O_2? Is it possible to locate the N at the interface in the sample with NO? For the EELS characterization the samples were investigated at very thin positions on the respective lamella in order to obtain the best results. Figures 9.5a and 9.5b show examples for the 2D windows that were scanned pixel by pixel for each of which a full EELS spectrum was recorded. For every row of the 2D scan a spatial drift correction was performed using the indicated window which contains a prominent feature. Since the interface follows along steps there were two posibilities to align the window for the spectrum images. The interface on plateau follows the high symmetry (0001)-plane which is shown in Figure 9.5a. Between the plateaus it follows a low symmetry $(11\bar{2}l)$-plane as shown in Figure 9.5b. Both cases were studied extensively for both samples and a series of spectrum images was recorded in order to obtain elemental profiles.

The spectrum images that were evaluated in terms of their Z-contrast from the HAADF detectors, the intensities of the C, Si, O, and N ionization edges as well as the chemical shift of the Si-$L_{2,3}$ edge, as suggested by J. Taillon et al. [95]. For each 2D window an averaging of the pixel rows parallel to the interface was conducted in order to reduce the noise and to result with a linescan-like profile perpendicular to the interface. For each sample and interface direction five 2D scans were recorded at different positions and their respective profiles averaged (after aligning them with respect to the 50% intensity position of the O profile) in order to further improve the results. It shall be emphasized at this point that the profiles due to the Si-$L_{2,3}$ chemical shift were not deemed a good measurement of the interface. The problem simply comes from the fact that the position of the edge is defined as the inflection point of the ionization edge which can be found by a numerical differentiation. As the spectra are very noisy, the differentiation amplifies the noise which creates some ambiguity in the evaluation of the position of the edge. Even with extensive smoothing applied to the initial profiles some of them contained jumps and thus were deemed not trustworthy for determining the interface thickness, see also appendix C. Nonetheless, what was found in the measurements taken is that all profiles have a very similar shape and width, with the C and O profiles being the ones that were deemed most reliable for the determination of the interface width, as discussed in section 5.2. Figures 9.5c to 9.5f show the final normalized C and O profiles for each sample and interface direction. The N profiles of the sample with NO were normalized to 0.5 and those of the sample with O_2 were scaled with the same factor.

The results clearly show how the C and O profiles follow the expected trend when scanning across the interface. Note that there is no sign for C excess in these profiles and nor in any profile recorded in this whole study. The interface width was determined by measuring the distance from the points where the profiles reach 98 % of the bulk value. While it was suggested by J. Taillon et al. that the interface thickness should be measured from the points where the

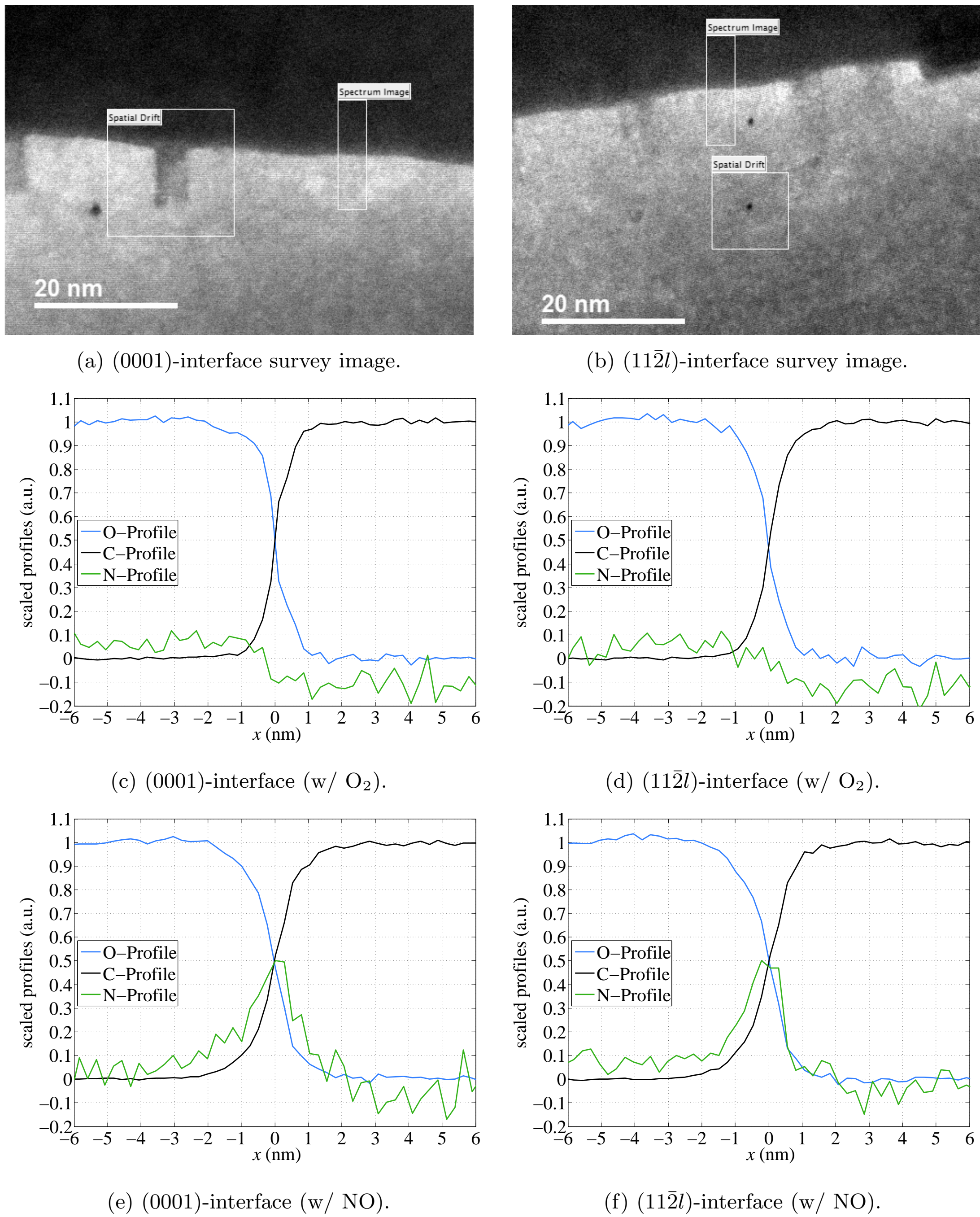

(a) (0001)-interface survey image.

(b) ($11\bar{2}l$)-interface survey image.

(c) (0001)-interface (w/ O_2).

(d) ($11\bar{2}l$)-interface (w/ O_2).

(e) (0001)-interface (w/ NO).

(f) ($11\bar{2}l$)-interface (w/ NO).

Figure 9.5: EELS profiles extracted from equally sized 2D-EELS scans at different orientations of the SiC-SiO_2 interface of the two samples.

Table 9.2: Interface thickness t_{int} determined by the Z-contrast, the O and C intensities, and the chemical shift of the Si-$L_{2,3}$ edge, as indicated by the indices.

Interface	$t_{\text{int},Z}$ (nm)	$t_{\text{int,C}}$ (nm)	$t_{\text{int,O}}$ (nm)	$t_{\text{int,Si}}$ (nm)
w/ O_2 (0001)	4.2(7)	2.7(2)	3.3(3)	2.4(2)
w/ O_2 $(11\bar{2}l)$	4.2(5)	3.2(5)	3.0(2)	2.1(6)
w/ NO (0001)	5.4(5)	3.0(4)	3.7(3)	3.2(4)
w/ NO $(11\bar{2}l)$	4.8(9)	4.2(5)	3.5(4)	3.7(3)

slopes of the profiles vanish [95], it was simply not deemed practical with the noisy data shown in this work. The determined interface widths from the averaged profiles for each sample and orientation are summarized in table 9.2. The indicated errors are the standard deviations from the five individual profiles before averaging. It is strongly emphasized that these errors just give more statistical meaning to the determined values, while they do not include any information on the true experimental errors. As table 9.2 shows, there is little difference between the (0001) and $(11\bar{2}l)$ planes for each sample, while there is a trend for the sample with O_2 having a slightly smaller interface thickness than the sample with NO, especially in the value determined by the Si-$L_{2,3}$ edge. However, due to the noisy data the resulting profiles contained artifacts, especially for the sample with NO. Consequently, the determination of the interface thickness with this method was deemed unreliable, as described in appendix C. The thicknesses obtained with this method should rather be interpreted as an estimate while more credibility can be given to the comparison of the C and O profiles. They are in good agreement, with an experimental interface thickness in the range of $\approx 3-4\,\text{nm}$ for both samples.

The EELS profiles of the sample with NO displayed in Figures 9.5e and 9.5f clearly show an increased N concentration right at the interface. As expected, this feature is absent in the sample with O_2. In order to demonstrate that this feature is not an artifact, all spectroscopic data of the $\approx 1.5\,\text{nm}$ wide interfacial region with increased N content was summed up for both samples to get the best signal-to-noise ratio. The resulting spectra after background subtraction were scaled to equal peak heights of the O edge, which is shown in the upper graph of Figure 9.6. The energy region of the N edge is shown in the lower graph. It is evident that the N peak is hidden within the noise indicating a very small concentration. However, since a significant component of the noise comes from the detection system, both signals contain comparable noise features. Therefore, a subtraction significantly reduces the noise as indicated by the black line. This spectrum clearly reveals the N ionization edge at $E_{loss} \approx 403\,\text{eV}$, as indicated by the red circle. However, while this ultimately proves the presence of N, the concentration is just above the detection limit and no reliable quantification was possible [252].

In order to visualize the results described above with a focus on the interfacial N content, a large EELS spectrum image of $\approx 15\,\text{nm} \times 45\,\text{nm}$ was recorded for each sample with identical experimental settings. The spectrum images were evaluated in terms of their Z-contrast as well as the EELS intensities of O, N, and C. The respective images showing the signal intensities as bright regions are shown in Figure 9.7. The Z-contrast and the O and C profiles reveal the interface with the macrosteps due to the step bunching, which are very similar in both samples. Note that the slight rotation between the interfaces of the two samples simply comes from a differently set angle of the window scanned by the electron beam, which has no effect on the experimental results.

As expected from the results above, the only clear difference between the samples is the increased N content in the sample with NO seen in Figure 9.7f. The N concentration is localized in a $\approx 1.5\,\text{nm}$ wide layer directly at the interface and appears to be evenly distributed over the

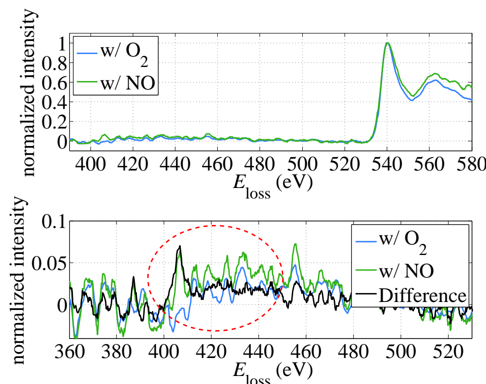

Figure 9.6: Energy loss region of N edge for the two samples. The spectra were normalized with respect to the O edge at $E_{\text{loss}} \approx 535\,\text{eV}$ (upper). Subtracting the spectra clearly reveals the N edge at $E_{\text{loss}} \approx 403\,\text{eV}$ (lower).

macrosteps. This means that N accumulates at both the (0001) and the $(11\bar{2}l)$ interfaces, as also observed in the profiles shown in Figure 9.5.

9.4 Discussion

The surface morphology of both devices shows similar distributions of the macrosteps in terms of their heights and lengths, as discussed in 9.2. The distributions are very broad which can be interpreted as disorder, since narrower distributions would indicate a more periodic interface. It was discussed in the literature that a deviation from periodicity can cause scattering, which degrades the device mobility [94]. If this was the main cause of the mobility reduction both devices studied in this work should have a low mobility, which is not the case. Therefore, it is concluded that the interface morphology and surface roughness due to the step bunching plays a minor role in the mobility degradation of the studied devices.

EELS was extensively applied in order to characterize the interface structure. It is emphasized at this point that none of the numerous EELS scans recorded contained any evidence for C excess at the interface, which is in agreements with many recent studies [94, 95, 96, 100, 118, 119, 250]. Therefore, large C clusters at the interface are discarded as the main mobility limiting factor for the studied devices. However, C excess in the form of small point defects like the carbon interstitial (C_i) defect cannot be ruled out as they may not cause a distinct feature in the obtained profiles.

The interface thickness was determined for both devices using several methods. As discussed, the O and C EELS profiles were given the most credibility resulting in an interface thickness of $\approx 3-4\,\text{nm}$, see table 9.2. Due to the uncertainty of the measurement these values should be interpreted as an estimate, rather than the precise interface thickness. Nonetheless, due to broadening effects of the experiment the values can be interpreted as an upper limit for the true interface thickness [224, 254]. The determined thicknesses are significantly smaller than those reported in several EELS studies [89, 95, 96, 128], while they are in good agreement with some other studies [88, 94, 117]. The study of P. Liu et al. investigated the surface roughness of the SiC-SiO_2 interface and concluded that it is in the order of $\approx 2\,\text{nm}$ [94]. Note that this is not the roughness due to the macrosteps discussed above but rather

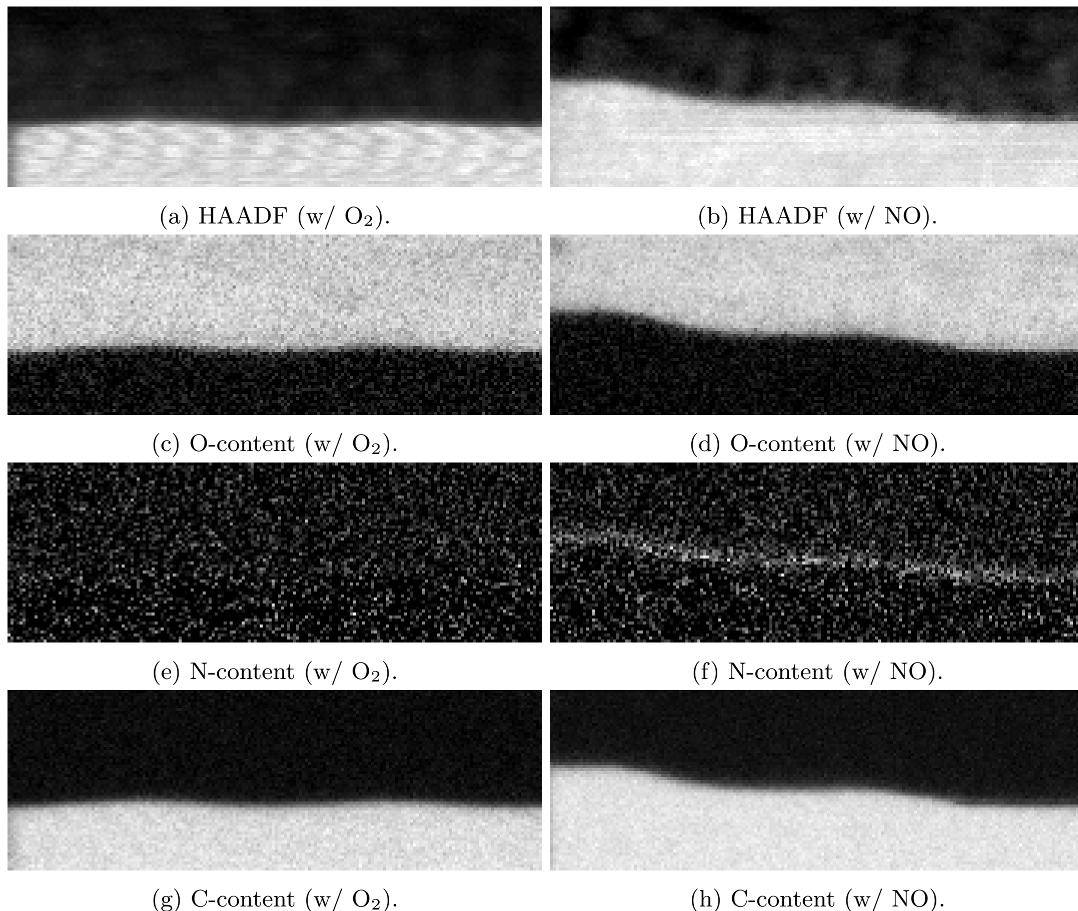

Figure 9.7: Comparison of different extracted data of $\approx 15\,\mathrm{nm} \times 45\,\mathrm{nm}$ 2D-EELS scans of the two samples revealing an increased N-content at the SiC-SiO_2 interface of the sample with NO.

the roughness in the viewing direction. When performing STEM and EELS of an interface with a roughness of 2 nm in the viewing direction, the profiles would appear broadened by this figure, as they are averaged over the roughness. If the roughness of the studied devices had a comparable roughness one could conclude that the interface is practically abrupt and only appears $\approx 3 - 4\,\mathrm{nm}$ wide due to the roughness combined with broadening effects [224, 254]. Confirming this idea is part of an ongoing project applying STEM tomography [251].

Some studies reported on an inverse correlation between the mobility and the interface thickness [89, 95]. This is clearly not the case for the samples studied in the present work. However, the devices in the above-mentioned studies had thermally grown oxides while the samples in this work have a deposited one. There is a tendency for the device with O_2 to have a slightly narrower interface than the device with NO, which would even suggest the opposite trend. The reason for the difference in the interface thickness could be found in the duration of the post-oxidation anneal. The device with O_2 only received a short anneal in O_2 atmosphere after oxide deposition in order to densify the oxide and to assure good physical contact, while it was desired to avoid significant reoxidation. The device with NO was passivated by a long anneal in NO atmosphere aiming for a good passivation of the interface and high channel

mobility. During this process a more pronounced reoxidation may occur than on the other device, which may result in a wider interface.

Another reason could be the formation of a silicon oxynitride (SiO_xN_y) layer, as suggested in the literature [129]. However, as the concentration of N was barely above the detection limit it is doubtful whether such a layer exists, even though it has been suggested that such a layer can be as thin as 1-2 atomic layers [129]. In order to have more insight into the difference between the two devices and the chemical composition of the interface region, more data processing including a chemical component analysis will be performed in an ongoing project [251]. While a thorough quantification of the N concentration was not possible due to the small concentration it is remarkable that a small N peak was found in every recorded spectrum image of the device with NO. The only previous EELS study that reported on a detectable N concentration at the Si-face SiC-SiO_2 interface found an increased N concentration in only about half of the scanned regions [128]. Whether this was due to a non-uniform distribution of the interfacial N or due to the experimental conditions is unknown. However, as observed in Figure 9.7f the device studied in this work appears to have a rather uniform N distribution.

9.5 Summary

The SiC-SiO_2 interface of the studied samples was extensively characterized and compared with STEM and EELS in order to reveal any structural differences that may explain the different channel mobility. Both samples contain a pronounced step-bunching with a broad distribution of lengths and heights of the macrosteps. A broad distribution indicates disorder, which was suggested to cause scattering and reduce the mobility in the literature [94] but is ruled out to be the mobility limiting factor for the devices studied in this thesis.

The elemental profiles acquired by EELS show no C enrichment in agreement with the majority of recent publications [94, 95, 96, 100, 118, 119, 250]. Large C clusters or C interlayers are ruled out as a mobility limiting factor for the studied devices.

The interface thickness was investigated primarily using the elemental EELS profiles. All samples have an experimentally obtained interface thickness of $\approx 3-4\,\text{nm}$. While the sample with O_2 appears to have a slightly narrower interface there is no certainty due to the experimental errors. The determined thickness can be interpreted as an upper limit of the true interface thickness, as surface roughness within the lamellas paired with broadening effects widen the profiles. It is suggested that the true interface thickness could even be abrupt. However, to verify this claim the microscopic surface roughness is going to be determined in an ongoing project [251].

The most prominent difference between the two studied devices is an increased N concentration in the sample with NO in an $\approx 1.5\,\text{nm}$ thick layer directly at the interface. The enrichment appears to be evenly distributed over the interface with no preference for either the (0001) or $(11\bar{2}l)$ interface. A reliable quantification of the concentration was not possible due to the extremely low signal, which was just above the detection limit. Nonetheless, all the spectrum images recorded for the sample with NO contained a distinct N peak at the interface, which is a novelty for EELS at the Si-face of the SiC-SiO_2 interface [128].

The measurements strongly suggest that the reason for the mobility degradation is found on an atomic scale and can not directly be observed in the STEM and EELS measurements. The most plausible explanation are point defects directly at the SiC-SiO_2 interface which are passivated by the N atoms, which underlines the relevance of the experiments described in the previous chapters.

Chapter 10

Conclusions and outlook

This work aimed to find the microscopic origin for the limited performance and reliability of SiC devices. Point defects play an important role in this degradation and their identification by EDMR was the central goal of this work. Numerous state-of-the-art SiC power devices where characterized and compared by electrical measurements, EDMR, TEM, and EELS.

While this project was set with a focus on the study of defects at the SiC-SiO_2 interface of SiC MOSFETs, one major achievement was the identification of an unknown bulk defect observed by EDMR in N-implanted SiC *pn*-junctions [6, 7]. This defect was identified to be the $N_CV_{Si}{}^0$ by comparing the experimental spectra to theoretical calculations, as discussed in chapter 6. Extensive DFT simulations of candidate defects performed by J. Cottom at UCL London were used to generate tables of accurate HF splitting constants, as listed in appendix A. From these tables simulated spectra were created using the program described in appendix B that could ultimately single out the $N_CV_{Si}{}^0$ defect as the one observed by EDMR. The formation of the N_CV_{Si} instead of the desired N_C donors is suggested as the reason for the saturation of the doping concentration at high N implantation doses [51].

The study of defects at the SiC-SiO_2 interface of SiC MOSFETs was primarily performed on a set of MOSFETs with different post-oxidation treatment (O_2, N_2O, and NO) but otherwise identical processing and geometry, as discussed in chapter 7. The devices had a state-of-the-art deposited gate oxide and were extensively characterized with electrical measurements revealing different channel mobilities, defect concentrations and threshold voltages. Using the BAE technique it was shown that the same EDMR spectrum with different relative intensity was dominant in all devices. This suggested that the same defect is present in all measured devices and that the passivation treatment has a strong influence on its relative intensity. C dangling bonds at the interface were suggested as a model for this defect, by using the simulation program described in appendix B. In order to confirm this model, theoretical calculations following the same methodology as for the bulk N_CV_{Si} are currently being performed by J. Cottom at UCL London with promising preliminary results [240].

The study on MOSFETs also revealed a second defect present in devices treated with N_2O. While this defect could not be identified due to its low intensity and the overlapping spectrum of the C dangling bond-like defect, it could be shown that the spectrum disappears at temperatures above $\approx 130\,^\circ C$. The defect was shown to likely consist of three lines, suggesting a N related defect. In order to get further insight into this defect, measurements at cryogenic temperatures have been conducted by R. Meszaros [217].

Depassivation effects by HCS were investigated on a SiC MOSFET by subsequently stressing the device and measuring its defect concentration, channel mobility, threshold voltage, and

EDMR spectrum, as discussed in chapter 8. The device received a modern state-of-the-art post-oxidation treatment in NO atmosphere, resulting in a high initial channel mobility. It was shown that the HCS strongly degrades the electrical performance of the device while at the same time the relative intensity of the EDMR response increases. The EDMR results suggest that a significant part of the intensity created by the stress is contained of the same defect as in the unstressed device. The mechanism suggested for the degradation is a depassivation of the (C dangling bond) defects that were initially passivated by the NO anneal.

As a final step in this project the SiC-SiO_2 interface was further characterized with TEM and EELS, as discussed in chapter 9. Due to contradicting literature on TEM of the SiC-SiO_2 interface it was important to put the devices measured by EDMR in this work into perspective. The study was based on comparing the interfaces of two MOSFETs with equal processing, despite the atmosphere of the post-oxidation anneal (O_2 and NO). The devices have dramatically different channel mobilities and defect concentrations and any microscopic differences of their interfaces were expected to be observable by TEM and EELS. The devices were compared in terms of their interface morphology and interface thickness showing no significant differences. The TEM observations seem to confirm the assumption made in the interpretation of the C dangling bonds present at the SiC-SiO_2 interface, namely a more or less abrupt interface in all devices with the defects being located directly at the interface. The only remarkable difference observed by EELS was an increased N concentration directly at the interface of the device treated with NO. This concentration was just above the detection limit and suggests that the passivation of point defects at the interface is the dominant mechanism for the increased performance and reliability of SiC MOSFETs subject to a post-oxidation treatment in NO.

In summary, this work established new insights into the microscopic processes responsible for the limited device performance and reliability of SiC power devices. While a direct link between the degraded mobility of SiC MOSFETs with the observed defects was not achieved, some correlations between device mobility, defect concentration, and EDMR intensity were found. The dominant defect spectra could be interpreted based on theoretical defect models. However, all observed defects are likely recombination centers deep in the bandgap, rather than shallow defects, as recombination is more efficient for deep level defects. Therefore, an identification of the high defect concentration of shallow defects close to the conduction band [68] was not obtained in this work.

Appendix A

Calculated hyperfine parameters for different N-containing defects in 4H-SiC

This appendix lists the HF parameters that have been calculated by J. Cottom at University College London and that have been used in order to identify the $N_C V_{Si}$ defect in N-implanted SiC *pn*-junctions (see chapter 6). The same data is found in the supplementary online material of [6].

Table A.1: HF data of different paramagnetic $N_C V_{Si}$ charge states for an initial comparison. The splitting constants a_k (in Gauss) of the atomic sites k are shown. For the neutral charge state (0) a low spin state (doublet) and a high spin state (quartet) exists.

	0 (doublet)	0 (quartet)	-1 (triplet)	-2 (doublet)
a_{N}	0.7	0.8	1.0	0.8
a_{C1}	38.4	44.6	45.7	6.8
a_{C2}	37.9	14.2	45.1	11.6
a_{C3}	29.0	39.5	45.1	48.0
a_{Si1}	11.5	11.8	7.6	0.9
a_{Si2}	11.0	12.7	7.6	0.5
a_{Si3}	11.0	11.6	9.3	1.2
a_{Si4}	9.8	4.4	7.9	0.8
a_{Si5}	10.0	5.0	7.2	1.8
a_{Si6}	9.8	2.8	9.0	1.9
a_{Si7}	10.8	11.9	8.0	11.1
a_{Si8}	10.7	12.5	7.2	10.9
a_{Si9}	10.4	12.1	9.0	10.9
a_{C5}	0.3	0.4	0.5	0.6
a_{C6}	0.4	0.7	0.5	0.3
a_{C7}	0.3	1.0	0.5	0.1
a_{C8}	0.6	0.6	0.6	0.1
a_{C9}	0.4	0.9	0.6	0.1
a_{C10}	0.5	0.3	0.5	0.6
a_{C11}	6.5	7.5	5.4	6.7

	0 (doublet)	0 (quartet)	-1 (triplet)	-2 (doublet)
a_{C12}	6.7	5.9	5.6	1.2
a_{C13}	5.8	6.8	4.8	6.7
a_{C14}	0.5	0.9	0.3	0.3
a_{C15}	5.5	3.2	5.8	0.1
a_{C16}	6.2	8.0	5.6	0.2
a_{C17}	5.5	0.9	4.8	1.3
a_{C18}	0.0	0.3	0.3	0.2
a_{C19}	0.0	1.2	0.3	0.5
a_{C20}	5.5	5.4	4.0	5.6
a_{C21}	0.0	0.8	0.1	0.3
a_{C22}	5.1	2.6	4.0	0.6
a_{C23}	0.0	0.6	0.2	0.5
a_{C24}	5.8	5.8	4.4	0.4

Table A.2: HF data of inequivalent sites of the $N_C V_{Si}{}^0$. The first letter indicates whether the V_{Si} is in an h or k site and the second letter indicates the same thing for the N_C.

	hh	hk_1	hk_2	hk_3	kk	kh_1	kh_2	kh_3
a_N	0.7	0.1	0.1	0.1	0.1	0.0	0.0	0.5
a_{C1}	39.8	14.2	13.9	17.4	3.2	18.7	3.2	32.7
a_{C2}	35.1	1.7	38.0	40.9	11.0	39.8	40.0	36.4
a_{C3}	41.0	39.3	2.7	5.0	40.2	3.4	13.7	19.5
a_{Si1}	0.2	0.3	0.0	0.1	0.1	4.4	2.7	9.2
a_{Si2}	0.4	0.2	0.2	0.2	0.1	3.8	2.3	9.3
a_{Si3}	0.5	0.1	0.1	0.0	0.1	4.6	2.0	8.6
a_{Si4}	11.2	2.0	2.8	3.8	0.2	11.0	0.0	11.8
a_{Si5}	10.5	2.5	2.4	3.8	0.2	11.2	0.0	11.8
a_{Si6}	11.1	2.5	2.1	4.0	0.6	10.3	0.5	10.9
a_{Si7}	9.9	0.1	10.7	10.5	1.9	0.3	11.5	7.9
a_{Si8}	10.2	0.9	10.8	11.3	1.9	0.0	11.6	8.3
a_{Si9}	9.8	0.4	10.5	10.4	2.2	0.1	11.2	7.8
a_{Si10}	11.1	11.0	0.2	1.9	11.7	1.9	4.4	0.2
a_{Si11}	10.5	11.3	0.1	2.6	11.4	2.4	4.5	0.0
a_{Si12}	10.7	10.9	0.1	2.2	11.6	2.1	4.5	0.0

Appendix B

A program for generating EDMR spectra from calculated HF data

The program used for generating the simulated spectra shown in chapters 6 and 7 is presented in this section. The program was written in the MATLAB code [220]. For the simulations presented in this work the program was slightly altered for each defect simulation in order to optimize the speed and accuracy of the simulation. This section only shows the code for the example of one simulation of the $N_C V_{Si}$ as shown in Figure 4.4. The data used for this particular simulation can be found in table A.1. The program consists basically of three parts, as follows.

First, the data is input in terms of the HF splitting constants, the possible states of the m_I values of the different atoms involved, and their probabilities. There is also a probability threshold defined which impacts the accuracy of the resulting simulation. The threshold is chosen so that a speedy simulation can be performed while still considering the vast majority of the total intensity to be considered.

Second, the data is processed in order to generate the positions of the lines and their respective probabilities by finding all combinations of m_I values for all interacting atoms. This part is divided into several smaller parts due to the enormous computational problem, see section 4.6.2. For the individual parts all necessary calculations are performed and data that is below the predefined probability threshold is discarded. Following the same process the subparts and finally all parts are joined to create the final set of line positions and probabilities.

Third, the spectrum is generated by adding a line profile to every calculated position. The intensity for each line is the calculated probability and the linewidth is the one defined in the beginning. Note that for this particular example the N splitting was added after this step, since three lines of equal intensity and linewidth are expected and no filtering is necessary. The resulting data is then normalized and saved.

This program is a simple tool to create accurate spectra from calculated HF data. It does not include any fitting functions or the like which is why the linewidth has to be matched to an experimental spectrum through multiple runs of the program. No consideration of the g-factor is given and only one type of defect can be simulated at a time. For different defects, the program has to be adapted, especially in terms of the second part where the problem is divided into smaller pieces. When simulating a spectrum made up of different defects the spectra have to be generated individually and later added to a complete spectrum.

```
% Data input

problim = 1e-6;      % Probability threshold

pC = 0.01109;      % Probability for I = 1/2 C atom
pS = 0.04685;      % Probability for I = 1/2 Si atom

Wl = 3.6;      % Lorentzian linewidth
Wg = 3.9;      % Gaussian linewidth

MIC = [-.5, 0, .5];      % m_I states of C
MIS = [-.5, 0, .5];      % m_I states of Si
pc = [pC/2, 1-pC, pC/2];      % Probabilities of m_I for C
ps = [pS/2, 1-pS, pS/2];      % Probabilities of m_I for Si

% HF constant of N atom
N0 = 0.70;

% HF constants of 1st shell (C)
C11 = 39.84;
C12 = 35.14;
C13 = 40.99;

% HF constants of 2nd shell (Si)
S21 = 11.22;
S22 = 10.46;
S23 = 11.05;
S24 = 9.94;
S25 = 10.17;
S26 = 9.78;
S27 = 11.09;
S28 = 10.46;
S29 = 10.86;

% HF constants of 3rd shell (C)
C31 = 6.00;
C32 = 5.54;
C33 = 4.05;
C34 = 4.11;
C35 = 4.01;
C36 = 6.08;
C37 = 6.73;
C38 = 5.10;
C39 = 0.45;
C310 = 5.45;
C311 = 6.24;
C312 = 5.51;
C313 = 5.48;
C314 = 5.12;
C315 = 5.77;

% Calculate HF interactions of 1st shell

% Line positions
c11 = MIC*C11;
c12 = MIC*C12;
c13 = MIC*C13;

A1 = combvec(c11,c12,c13);      % Array of all combinations of HF splittings
A1 = sum(A1,1);      % Resulting line positions
nt(1) = numel(A1);      % Number of lines before filtering
```

```
PC1 = combvec(pc,pc,pc);      % Array of all combinations of probabilities
c1p = prod(PC1,1);      % Resulting probabilities
c1help = c1p > problim;      % Index for combinations above threshold

P1 = c1p(c1help);      % Getting rid of subthreshold data
A1 = A1(c1help);      % Getting rid of subthreshold data
pp(1) = sum(P1);      % Fraction of considered intensity
nn(1) = numel(A1);      % Remaining number of lines

% Calculate HF interactions of 2nd shell

% Line positions
s21 = MIS*S21;
s22 = MIS*S22;
s23 = MIS*S23;
s24 = MIS*S24;
s25 = MIS*S25;
s26 = MIS*S26;
s27 = MIS*S27;
s28 = MIS*S28;
s29 = MIS*S29;

A2 = combvec(s21,s22,s23,s24,s25,s26,s27,s28,s29);      % Array of all combinations of HF splittings
A2 = sum(A2,1);      % Resulting line positions
nt(2) = numel(A2);      % Number of lines before filtering

PS2 = combvec(ps,ps,ps,ps,ps,ps,ps,ps,ps);      % Array of all combinations of probabilities
s2p = prod(PS2,1);      % Resulting probabilities
s2help = s2p > problim;      % Index for combinations above threshold

P2 = s2p(s2help);      % Getting rid of subthreshold data
A2 = A2(s2help);      % Getting rid of subthreshold data
pp(2) = sum(P2);      % Fraction of considered intensity
nn(2) = numel(A2);      % Remaining number of lines

% Combining 1st and 2nd shell

A12 = combvec(A1,A2);      % Array of all combinations of HF splittings
a12 = sum(A12,1);      % Resulting line positions
nt(3) = numel(a12);      % Number of lines before filtering

P12 = combvec(P1,P2);      % Array of all combinations of probabilities
p12 = prod(P12,1);      % Resulting probabilities
p12help = p12 > problim;      % Index for combinations above threshold

P12 = p12(p12help);      % Getting rid of subthreshold data
A12 = a12(p12help);      % Getting rid of subthreshold data

pp(3) = sum(P12);      % Fraction of considered intensity
nn(3) = numel(A12);      % Remaining number of lines

% Calculate HF interactions of 3rd shell (split into 2 parts due to memory/speed)

% Part 1

% Line positions
c31 = MIC*C31;
c32 = MIC*C32;
c33 = MIC*C33;
c34 = MIC*C34;
c35 = MIC*C35;
c36 = MIC*C36;
```

```
c37 = MIC*C37;
c38 = MIC*C38;

A3a = combvec(c31,c32,c33,c34,c35,c36,c37,c38);      % Array of all combinations of HF splittings
A3a = sum(A3a,1);      % Resulting line positions
nt(4) = numel(A3a);      % Number of lines before filtering

PC3a = combvec(pc,pc,pc,pc,pc,pc,pc,pc);% Array of all combinations of probabilities
c3ap = prod(PC3a,1);% Resulting probabilities
c3ahelp = c3ap > problim;      % Index for combinations above threshold

P3a = c3ap(c3ahelp);      % Getting rid of subthreshold data
A3a = A3a(c3ahelp);      % Getting rid of subthreshold data
pp(4) = sum(P3a);      % Fraction of considered intensity
nn(4) = numel(A3a);      % Remaining number of lines

% Part 2

% Line positions
c39 = MIC*C39;
c310 = MIC*C310;
c311 = MIC*C311;
c312 = MIC*C312;
c313 = MIC*C313;
c314 = MIC*C314;
c315 = MIC*C315;

A3b = combvec(c39,c310,c311,c312,c313,c314,c315);      % Array of all combinations of HF splittings
A3b = sum(A3b,1);      % Resulting line positions
nt(5) = numel(A3b);      % Number of lines before filtering

PC3b = combvec(pc,pc,pc,pc,pc,pc,pc);      % Array of all combinations of probabilities
c3bp = prod(PC3b,1);      % Resulting probabilities
c3bhelp = c3bp > problim;      % Index for combinations above threshold

P3b = c3bp(c3bhelp);      % Getting rid of subthreshold data
A3b = A3b(c3bhelp);      % Getting rid of subthreshold data
pp(5) = sum(P3b);      % Fraction of considered intensity
nn(5) = numel(A3b);      % Remaining number of lines

% Combining part 1 and 2

A3 = combvec(A3a,A3b);      % Array of all combinations of HF splittings
a3 = sum(A3,1);      % Resulting line positions
nt(6) = numel(a3);      % Number of lines before filtering

P3 = combvec(P3a,P3b);      % Array of all combinations of probabilities
p3 = prod(P3,1);      % Resulting probabilities
p3help = p3 > problim;      % Index for combinations above threshold

A3 = a3(p3help);      % Getting rid of subthreshold data
P3 = p3(p3help);      % Getting rid of subthreshold data
pp(6) = sum(P3);      % Fraction of considered intensity
nn(6) = numel(A3);      % Remaining number of lines

% Combining everything

A123 = combvec(A12,A3);      % Array of all combinations of HF splittings
a123 = sum(A123,1);      % Resulting line positions

P123 = combvec(P12,P3);      % Array of all combinations of probabilities
p123 = prod(P123,1);      % Resulting probabilities
```

```
p123help = p123 > problim;        % Index for combinations above threshold

A123 = a123(p123help);        % Getting rid of subthreshold data
P123 = p123(p123help);        % Getting rid of subthreshold data
pp(7) = sum(P123);        % Fraction of considered intensity
nn(7) = numel(A123);        % Remaining number of lines
nt(7) = prod(nt([1,2,4,5]));        % Total number of lines

% Creating the spectra

x = linspace(-80,80,801);        % Magnetic field vector of appropriate size
yg = zeros(size(x));        % Intensity vector for Gaussian simulation
yl = zeros(size(x));        % Intensity vector for Lorentzian simulation

for k = 1:numel(A123)        % Loop for adding every line to the intensity vectors

yg = yg+gaussline(x,A123(k),P123(k),Wg);        % Adds derivative Gaussian line to yg
yl = yl+lorline(x,A123(k),P123(k),Wl);        % Adds derivative Lorentzian line to yl

end        % End of loop

% Adding the splitting of the N atom
x1 = x-N0;        % Line for I = −1
x2 = x+N0;        % Line for I = 1

yg1 = spline(x1,yg,x);        % Splining
yg2 = spline(x2,yg,x);        % Splining
yl1 = spline(x1,yl,x);        % Splining
yl2 = spline(x2,yl,x);        % Splining

yg = yg1+yg2+yg;        % Summing
yl = yl1+yl2+yl;        % Summing

yg = yg/max(yg);        % Normalizing
yl = yl/max(yl);        % Normalizing

T = nt(7)*3        % Output total number of lines
N = nn(end)*3        % Output number of lines simulated
P = pp(7)        % Output simulated probability

YL = [x',yl'];        % Prepare data for saving
save(['LorentzianSimulation.txt'],'YL','-ASCII')        % Save data

YG = [x',yg'];        % Prepare data for saving
save(['GaussianSimulation.txt'],'YG','-ASCII')        % Save data
```

Appendix C

Problems with determining the $SiC\text{-}SiO_2$ interface thickness from the $Si\text{-}L_{2,3}$ EELS edge

As discussed in section 5.2, the interface thickness of the $SiC\text{-}SiO_2$ interface can be determined by different profiles obtained by TEM and EELS. J. Taillon et al. suggested that the chemical shift of the $Si\text{-}L_{2,3}$ EELS edge is the most reliable method [95]. However, as discussed in the following, this method was deemed unreliable for a meaningful comparison of the data shown in chapter 9.

Figure C.1a shows a series of consecutive EELS spectra taken from a linescan across the interface. The background has been subtracted and the $Si\text{-}L_{2,3}$ ionization edge is clearly seen. However, there are basically two issues with the data that cause problems in the further processing. The first one is that the data contains a significant amount of noise and second one is that there is a distinct bump on the ionization edge at $E_{\text{loss}} \approx 106\,\text{eV}$. Both cause problems with the determination of the edge position, which is defined as the inflection point of the edge, i.e. the point of the steepest slope which can be found by a numerical differentiation.

The derivative spectra are shown in Figure C.1b. What is immediately observable is that the noise in the initial curves is amplified by the numerical differentiation and that the curves contain two maxima, i.e. two inflection points. The former problem can be minimized by applying extensive smoothing to the initial curve which dramatically reduces the noise after the differentiation, as observed in the black curves. However, due to the bump in the initial curves there are still two maxima in the differentiated curves. It is not clear which of them should be considered as the position of the ionization edge. What adds to the problem is that their magnitude is almost identical. In some of the spectra shown the maximum at $\approx 105\,\text{eV}$ is bigger and in some of them the one at $\approx 107\,\text{eV}$. As a result, the resulting profiles contains jumps that can be seen in the red curve in Figure C.1c. Even in a "good" spectrum as indicated by the green line in the same graph there are some jumps.

Evidently, these artifacts observed blur the true interface thickness and no reliable interpretation can be made. While improving the numerical determination of the inflection point can be optimized and "bad" spectra can be left out, the interface thicknesses obtained with this method cannot be given too much credibility. Additionally, the problems shown mostly affected the sample annealed with NO which makes a meaningful comparison of the interface thickness obtained for the two samples by the chemical shift method impossible.

In order to compare the two samples the more reproducible O and C profiles were used in chapter 9. In an ongoing project more data processing is conducted aiming for a compositional analysis [251]. In this approach the EELS spectra obtained for the two bulk sides are used to reproduce the spectra obtained at the interface by a linear combination. This method can give a more meaningful measurement of the interface thickness and reveal the presence of an additional phase directly at the interface.

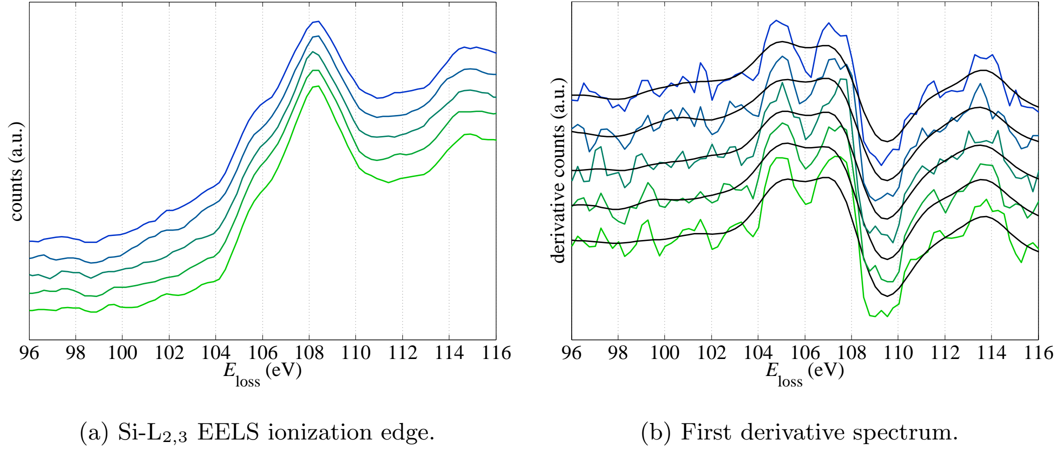

(a) Si-$L_{2,3}$ EELS ionization edge.

(b) First derivative spectrum.

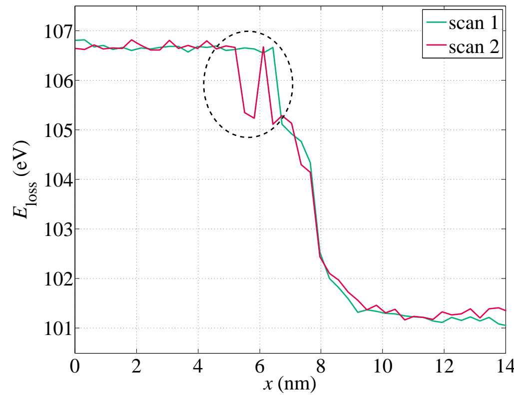

(c) Comparison of the complete resulting profile (red) with a "good" one (green).

Figure C.1: A series of spectra selected from a linescan (a) and their numerical derivatives (b), note that the black lines are the derivatives after smoothing the initial spectra. The selected series of spectra is indicated by the circle in the resulting profile (c).

Appendix D

Temperature dependent resistance of a poly-heater

The poly-heater structure used in the experiments described in section 7.5.3 was used to increase the temperature of the studied device. As the resistance of the poly-heater is temperature dependent, measuring the resistance can be used to determine the temperature. Figure D.1 shows a calibration curve of which was determined using a thermal chuck. The temperature of the thermal chuck was set to well defined temperature values while the resistance of the poly-heater was measured with a needle probing station. This curve was used for the measurements in 7.5.3. A voltage was applied to the poly-heater and the resistance was monitored. The voltage was increased until the resistance corresponding to the desired temperature was reached.

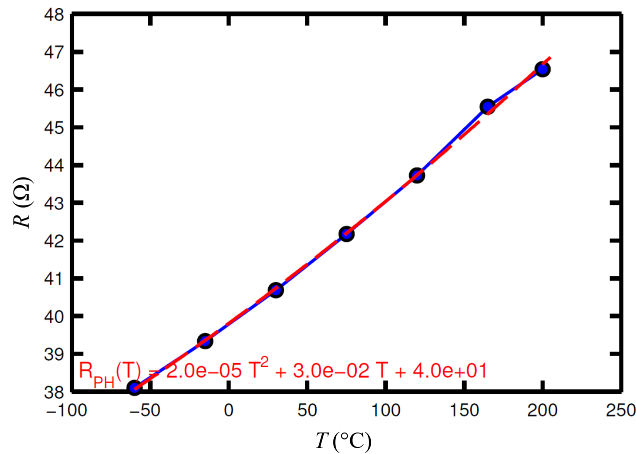

Figure D.1: Temperature dependent resistance of a poly-heater structure, courtesy of G. Pobegen [255].

References

[1] G. Gruber. “Characterization of point defects in semiconductors using electrically detected magnetic resonance.” MA thesis. Graz University of Technology, 2012.

[2] G. Gruber et al. “Interface defects in SiC power MOSFETs - An electrically detected magnetic resonance study based on spin dependent recombination.” In: *AIP Conference Proceedings* 1583 (2014), pp. 165–168.

[3] G. Gruber et al. “Electrically detected magnetic resonance study of defects created by hot carrier stress at the SiC/SiO_2 interface of a SiC *n*-channel metal-oxide-semiconductor field-effect transistor.” In: *Applied Physics Letters* 105 (2014), p. 043506.

[4] G. Pobegen et al. “Impact of hot carrier degradation and positive bias temperature stress on lateral 4H-SiC nMOSFETs.” In: *Materials Science Forum* 778-780 (2014), pp. 959–962.

[5] G. Gruber et al. “Influence of oxide processing on the defects at the SiC-SiO2 interface measured by electrically detected magnetic resonance.” In: *Materials Science Forum* 858 (2016), pp. 643–646.

[6] J. Cottom et al. “Recombination centers in 4H-SiC investigated by electrically detected magnetic resonance and *ab initio* modeling.” In: *Journal of Applied Physics* 119 (2016), p. 181507.

[7] T. Aichinger et al. “A nitrogen-related deep level defect in ion implanted 4H-SiC pn junctions - A spin dependent recombination study.” In: *Applied Physics Letters* 100 (2012), p. 112113.

[8] J.A. Lely. “Darstellung von Einkristallen von Silicium Carbid und Beherrschung von Art und Menge der eingebauten Verunreinigungen.” In: *Berichte der Deutschen Keramischen Gesellschaft* 32 (1955), pp. 229–231.

[9] Y.M. Tairov and V.F. Tsvetkov. “Investigation of growth processes of ingots of silicon carbide single crystals.” In: *Journal of Crystal Growth* 43 (1978), pp. 209–212.

[10] N. Kuroda et al. “Step-controlled VPE growth of SiC single crystals at low temperatures.” In: *Extended abstracts of the 19th conference on Solid State Devices and Materials* (1987), pp. 227–230.

[11] D. Nakamura et al. “Ultrahigh-quality silicon carbide single crystals.” In: *Nature* 430 (2004), pp. 1009–1012.

[12] S. Nishizawa. “Development of SiC Crystal Growth in the Past, Present and Future.” In: *European Materials Research Society Spring Meeting, Lille*. 2014.

[13] J.W. Palmour. “Introduction to SiC Materials and Technology.” In: *International Conference on Silicon Carbide and Related Materials, Giardini-Naxos*. 2015.

[14] Cree, Inc. (USA). *www.cree.com.*

[15] Infineon Technologies AG (Germany). *www.infineon.com.*

[16] Wolfspeed, A Cree Company (USA). *www.wolfspeed.com.*

[17] R. Cheung, ed. *Silicon Carbide Microelectromechanical Systems for Harsh Environments.* Imperial College Press, 2006.

[18] H.M. Otte and A.G. Crocker. "Crystallographic Formulae for Hexagonal Lattices." In: *Physica Status Solidi B* 9 (1965), pp. 441–450.

[19] F. Bechstedt et al. "Polytypism and Properties of Silicon Carbide." In: *Physica Status Solidi B* 202 (1997), pp. 35–62.

[20] H.E. Nilsson and M. Hjelm. "Monte Carlo simulation of electron transport in 2H-SiC using a three valley analytical conduction band model." In: *Journal of Applied Physics* 86 (1999), pp. 6230–6233.

[21] C. Persson and U. Lindefelt. "Relativistic band structure calculation of cubic and hexagonal SiC polytypes." In: *Journal of Applied Physics* 82 (1997), pp. 5496–5508.

[22] T. Kimoto and J.A. Cooper, eds. *Fundamentals of Silicon Carbide Technology.* John Wiley and Sons Singapore, 2014.

[23] W.Y. Ching et al. "The Electronic Structure and Spectroscopic Properties of 3C, 2H, 4H, 6H, 15R and 21R Polymorphs of SiC." In: *Materials Science & Engineering A* 422 (2006), pp. 147–156.

[24] M.B.J. Wijesundara and R.G. Azevedo. *Silicon Carbide Microsystems for Harsh Environments.* Springer New York, 2011.

[25] A.V. Krukau et al. "Influence of the exchange screening parameter on the performance of screened hybrid functionals." In: *The Journal of Chemical Physics* 125 (2006), p. 224106.

[26] O.T. Hofmann. *Graz University of Technology, private communication.*

[27] W.C. Lien et al. "4H-SiC N-Channel JFET for Operation in High-Temperature Environments." In: *IEEE Journal of the Electron Devices Society* 2 (2014), pp. 164–167.

[28] S.Q. Shao et al. "4H-Silicon Carbide p-n Diode for High-Temperature (600 °C)." In: *Materials Science Forum* 821-823 (2015), pp. 636–639.

[29] E.V. Brunt et al. "22 kV, 1 cm^2, 4H-SiC n-IGBTs with improved conductivity modulation." In: *Proceedings of the 26th International Symposium on Power Semiconductor Devices & IC's.* 2014, pp. 358–361.

[30] S. Sriram et al. "4H-SiC MESFET's with 42 GHz f_{max}." In: *IEEE Electron Device Letters* 17 (1996), pp. 369–371.

[31] C.M. Zetterling and M. Östling. *Process Technology for Silicon Carbide Devices.* Ed. by C.M. Zetterling. INSPEC, 2002.

[32] M.N. Yoder. "Wide Bandgap Semiconductor Materials and Devices." In: *IEEE Transactions on Electron Devices* 43 (1996), pp. 1633–1636.

[33] J.L. Hudgins et al. "An Assessment of Wide Bandgap Semiconductor for Power Devices." In: *IEEE Transactions on Power Electronics* 18 (2003), pp. 907–914.

[34] J. Czochralski. "Ein neues Verfahren zur Messung der Kristallisationsgeschwindigheit der Metalle." In: *Zeitschrift für physikalische Chemie* 92 (1918), pp. 219–221.

[35] G.K. Teal and E. Buehler. "Growth of Silicon Single Crystals and of Single Crystal Silicion PN Junctions." In: *Physical Review* 87 (1952), p. 190.

[36] T. Sudarshan. "SiC Power Materials - Devices and Applications." In: ed. by Z.C. Feng. Springer-Verlag Berlin Heidelberg, 2004. Chap. Materials Science and Engineering of Bulk Silicon Carbides, pp. 1–61.

[37] T. Ujihara. "Introduction of SiC Solution Growth in Comparison with other Methods." In: *International Conference on Silicon Carbide and Related Materials, Giardini-Naxos*. 2015.

[38] N. Hoshino et al. "High-speed, high-quality crystal growth of 4H-SiC by high-temperature gas source method." In: *Applied Physics Express* 7 (2014), p. 065502.

[39] B.M. Epelbaum, O. Filip, and A. Winnacker. "Bulk and epitaxial growth of micropipe-free silicon carbide on basal and rhombohedral plane seeds." In: *Physica Status Solidi B: Basic Solid State Physics* 245 (2008), pp. 1257–1271.

[40] S.G. Müller et al. "The status of SiC bulk growth from an industrial point of view." In: *Journal of Crystal Growth* 211 (2000), pp. 325–332.

[41] K. Kamei et al. "Solution growth of single crystal 6H, 4H-SiC using Si-Ti-C melt." In: *Journal of Crystal Growth* 311 (2009), pp. 855–858.

[42] Y. Yamamoto et al. "Low-dislocation-density 4H-SiC crystal growth utilizing dislocation conversion during solution method." In: *Applied Physics Express* 7 (2014), p. 065501.

[43] T. Kimoto and H. Matsunami. "Silicon Carbide: Materials, Processing and Devices." In: ed. by Z.C. Feng and J.H. Zhao. Vol. 20. Taylor & Francis Books, Inc, 2004. Chap. Epitaxial Growth of High-Quality Silicon Carbide: Fundamentals and Recent Progress, pp. 1–40.

[44] B. Kallinger et al. "Step-controlled homoepitaxial growth of 4H-SiC on vicinal substrates." In: *Journal of Crystal Growth* 381 (2013), pp. 127–133.

[45] B. Kallinger et al. "Dislocation Conversion and Propagation during Homoepitaxial Growth of 4H-SiC." In: *Materials Science Forum* 645-648 (2010), pp. 299–302.

[46] A.J. Steckl et al. "Atomic probe microscopy of 3C SiC films grown on 6H SiC substrates." In: *Applied Physics Letters* 62 (1993), pp. 2545–2547.

[47] M.A. Kulakov et al. "Scanning tunneling microscopy on the 6H SiC(0001) surface." In: *Surface Science* 315 (1994), pp. 248–254.

[48] T. Kimoto, A. Itoh, and H. Matsunami. "Step bunching in chemical vapor deposition of 6H- and 4H-SiC on vicinal SiC(0001) faces." In: *Applied Physics Letters* 66 (1995), pp. 3645–3647.

[49] T. Kimoto et al. "Step bunching mechanism in chemical vapor deposition of 6H- and 4H-SiC {0001}." In: *Journal of Applied Physics* 81 (1997), pp. 3494–3500.

[50] T. Kimoto et al. "Surface Morphological Structures of 4H-, 6H- and 15R-SiC(0001) Epitaxial Layers Grown by Chemical Vapor Deposition." In: *Japanese Journal of Applied Physics* 40 (2001), pp. 3315–3319.

[51] M.V. Rao. "Silicon Carbide: Materials, Processing and Devices." In: ed. by Z.C. Feng and J.H. Zhao. Vol. 20. Taylor & Francis Books, Inc, 2004. Chap. Ion-Implantation in SiC, pp. 165–201.

[52] S. Seshadri, G.W. Eldridge, and A.K. Agarwal. "Comparison of the annealing behavior of high-dose nitrogen-, aluminum-, and boron-implanted 4H-SiC." In: *Applied Physics Letters* 72 (1988), pp. 2026–2028.

[53] M.A. Capano et al. “Ionization energies and electron mobilities in phosphorus- and nitrogen-implanted 4H-silicon carbide.” In: *Journal of Applied Physics* 87 (2000), pp. 8773–8777.

[54] J.B. Tucker et al. “Material and n-p junction characteristics of As- and Sb-implanted SiC.” In: *Diamond and Related Materials* 9 (2000), pp. 1887–1896.

[55] O.J. Marsh and H.L. Dunlap. “Ion-implanted junctions and conducting layers in SiC.” In: *Radiation Effects* 6 (1970), pp. 301–311.

[56] K. Szász et al. “Theoretical and electron paramagnetic resonance studies of hyperfine interaction in nitrogen doped 4H and 6H SiC.” In: *Journal of Applied Physics* 115 (2014), p. 073705.

[57] I.G. Ivanov, A. Henry, and E. Janzén. “Ionization energies of phosphorus and nitrogen donors and aluminum acceptors in 4H silicon carbide from the donor-acceptor pair emission.” In: *Physical Review B* 71 (2005), p. 241201.

[58] H.H. Woodbury and G.W. Ludwig. “Electron Spin Resonance Studies in SiC.” In: *Physical Review* 124 (1961), pp. 1083–1089.

[59] S. Greulich-Weber. “EPR and ENDOR Investigations of Shallow Impurities in SiC Polytypes.” In: *Physica Status Solidi A* 162 (1997), pp. 95–151.

[60] E.N. Kalabukhova et al. “EPR, ESE and Pulsed ENDOR Study of Nitrogen Related Center in 4H-SiC Wafers Grown by Different Technologies.” In: *Materials Science Forum* 556-557 (2007), pp. 355–358.

[61] D.V. Savchenko, B.D. Shanina, and E.N. Kalabukhova. “Properties and Applications of Silicon Carbide.” In: ed. by R. Gerhardt. Intech Open, 2011. Chap. Identification and Kinetic Properties of the Photosensitive Impurities and Defects in High-Purity Semi-Insulating Silicon Carbide.

[62] Y. Hirano and T. Inada. “Nitrogen implantation in (100)-β-SiC layers grown on Si substrate.” In: *Journal of Applied Physics* 77 (1995), pp. 1020–1028.

[63] A. Nakao et al. “XPS characterization of nitrogen implanted silicon carbide.” In: *Nuclear Instruments and Methods in Physics Research Section B* 65 (1992), pp. 352–356.

[64] D. Aberg et al. “Nitrogen deactivation by implantation-induced defects in 4H-SiC epitaxial layers.” In: *Applied Physics Letters* 78 (2001), pp. 2908–2910.

[65] Y. Negoro, T. Kimoto, and H. Matsunami. “Carrier compensation near tail region in aluminum- or boron-implanted 4H-SiC (0001).” In: *Journal of Applied Physics* 98 (2005), p. 043709.

[66] D. Panknin et al. “Correlation of electrical and microstructural properties after high dose aluminium implantation into 6H-SiC.” In: *Materials Science & Engineering B* 61-62 (1999), pp. 363–367.

[67] G. Pensl et al. “Alternative techniques to reduce interface traps in n-type 4H-SiC MOS capacitors.” In: *Physica Status Solidi B* 245 (2008), pp. 1378–1389.

[68] V.V. Afanasev et al. “Intrinsic SiC/SiO_2 Interface States.” In: *Physica Status Solidi A* 162 (1997), pp. 321–337.

[69] K. Ueno, R. Asai, and T. Tsuji. “4H-SiC MOSFETs Utilizing the H_2 Surface Cleaning Technique.” In: *IEEE Electron Device Letters* 19 (1998), pp. 244–246.

[70] J. Rozen et al. “Scaling Between Channel Mobility and Interface State Density in SiC MOSFETs.” In: *IEEE Transactions on Electron Devices* 58 (2011), pp. 3808–3811.

[71] S. Dhar et al. "Defects in Microelectronic Materials and Devices." In: ed. by D.M. Fleetwood, S.T. Pantelides, and R.D. Schrimpf. Taylor & Francis Group, 2008. Chap. Silicon Dioxide-Silicon Carbide Interfaces: Current Status and Recent Advances, pp. 575–614.

[72] G. Rescher, G. Pobegen, and T. Grasser. "Threshold voltage instabilities of present SiC-power MOSFETs under positive bias temperature stress." In: *Materials Science Forum* 858 (2016), pp. 481–484.

[73] F. Roccaforte, P. Fiorenza, and F. Giannazzo. "Impact of the Morphological and Electrical Properties of SiO_2/4H-SiC Interface on the Behavior of 4H-SiC MOSFETs." In: *ECS Journal of solid State Science and Technology* 2 (2013), N3006–N3011.

[74] S. Potbhare et al. "Numerical and experimental characterization of 4H-silicon carbide lateral metal-oxide-semiconductor field-effect transistor." In: *Journal of applied Physics* 100 (2006), p. 044515.

[75] A. Salinaro et al. "Charge Pumping Measurements on Differently Passivated Lateral 4H-SiC MOSFETs." In: *IEEE Transactions on Electron Devices* 62 (2015), pp. 155–163.

[76] S.M. Sze and K.K. Ng. *Physics of Semiconductor Devices.* 3rd ed. John Wiley & Sons, 2007.

[77] D.K. Schroder. *Semiconductor Material and Device Characterization.* 3rd ed. Wiley Interscience, 2008.

[78] E.H. Nicollian and J.R. Brews. *MOS (Metal Oxide Semiconductor) Physics and Technology.* Wiley-Interscience, 1982.

[79] J. Pernot et al. "Electrical transport in n-type 4H silicon carbide." In: *Journal of Applied Physics* 90 (2001), pp. 1869–1878.

[80] S. Takagi et al. "On the Universality of Inversion Layer Mobility in Si MOSFET's: Part I-Effects of Substrate Impurity Concentration." In: *IEEE Transactions on Electron Devices* 41 (1994), pp. 2357–2362.

[81] S.K. Powell et al. "Physics-based numerical modeling and characterization of 6H-silicon-carbide metal–oxide–semiconductor field-effect transistors." In: *Journal of Applied Physics* 92 (2002), pp. 4053–4061.

[82] G. Ghibaudo. "New method for the extraction of MOSFET parameters." In: *Electronics Letters* 24 (1988), pp. 543–545.

[83] S. Dhar et al. "Inversion layer carrier concentration and mobility in 4H–SiC metal-oxide-semiconductor field-effect transistors." In: *Journal of Applied Physics* 108 (2010), p. 054509.

[84] J. Rozen. "Electronic Properties and Reliability of the SiC-SiO_2 Interface." PhD thesis. Vanderbilt University, 2008.

[85] T. Ono and S. Saito. "First-principles study on the effect of SiO_2 layers during oxidation of 4H-SiC." In: *Applied Physics Letters* 106 (2015), p. 081601.

[86] M. Bassler, G. Pensl, and V. Afanasev. ""Carbon cluster model" for electronic states at SiC/SiO_2 interfaces." In: *Diamond and Related Materials* 6 (1997), pp. 1472–1475.

[87] G.G. Jernigan, R.E. Stahlbush, and N.S. Saks. "Effect of oxidation and reoxidation on the oxide-substrate interface of 4H- and 6H-SiC." In: *Applied Physics Letters* 77 (2000), pp. 1437–1439.

[88] T. Zheleva et al. “Transition layers at the SiO_2/SiC interface.” In: *Applied Physics Letters* 93 (2008), p. 022108.

[89] T.L. Biggerstaff et al. “Relationship between 4H-SiC/SiO_2 transition layer thickness and mobility.” In: *Applied Physics Letters* 95 (2009), p. 032108.

[90] S. Dhar et al. “Effect of nitric oxide annealing on the interface trap density near the conduction bandedge of 4H-SiC at the oxide/$(11\bar{2}0)$ 4H-SiC interface.” In: *Applied Physics Letters* 84 (2004), pp. 1498–1500.

[91] J.M. Knaup et al. “Theoretical study of the mechanism of dry oxidation of 4H-SiC.” In: *Physical Review B* 71 (2005), p. 235321.

[92] J.M. Knaup et al. “Defects in SiO_2 as the possible origin of near interface traps in the SiC/SiO_2 system: A systematic theoretical study.” In: *Physical Review B* 72 (2005), p. 115323.

[93] I. Iskandarova et al. “The role of neutral point defects in carrier mobility degradation in bulk 4H-SiC and at 4H-SiC/SiO_2 interface: First-principles investigation using Green’s functions.” In: *Journal of Applied Physics* 117 (2015), p. 175703.

[94] P. Liu et al. “Roughness of the SiC/SiO_2 vicinal interface and atomic structure of the transition layers.” In: *Journal of Vacuum Science & Technology A* 32 (2014), p. 060603.

[95] J.A. Taillon et al. “Systematic structural and chemical characterization of the transition layer at the interface of NO-annealed 4H-SiC/SiO_2 metal-oxide-semiconductor field-effect transistors.” In: *Journal of Applied Physics* 113 (2013), p. 044517.

[96] T. Hatakeyama et al. “Microscopic Examination of SiO_2/4H-SiC Interfaces.” In: *Materials Science Forum* 679-680 (2011), pp. 330–333.

[97] A.C. Jones and M.L. Hitchman, eds. *Chemial Vapour Deposition: Precursors, Processes and Applications*. Royal Society of Chemistry, 2009.

[98] T. Kimoto et al. “Improved Dielectric and Interface Properties of 4H-SiC MOS Structures Processed by Oxide Deposition and N_2O Annealing.” In: *Materials Science Forum* 527-529 (2006), pp. 987–990.

[99] Y. Wang et al. “The Effect of Gate Oxide Processes on the Performance of 4H-SiC MOSFETs and Gate-Controlled Diodes.” In: *IEEE Transactions on Electron Devices* 55 (2008), pp. 2046–2053.

[100] A. Salinaro. “Characterization and Development of the 4H-SiC/SiO_2 Interface for Power MOSFET Applications.” PhD thesis. Friedrich-Alexander-Universität Erlangen-Nürnberg, 2015.

[101] R. Schörner et al. “Significantly Improved Performance of MOSFET’s on Silicon Carbide Using the 15R-SiC Polytype.” In: *IEEE Electron Device Letters* 20 (1999), pp. 241–244.

[102] J.A. Cooper Jr. et al. “Status and Prospects for SiC Power MOSFETs.” In: *IEEE Transactions on Electron Devices* 49 (2002), pp. 658–664.

[103] P. Déak et al. “The mechanism of defect creation and passivation at the SiC/SiO_2 interface.” In: *Journal of Physics D* 40 (2007), pp. 6242–6253.

[104] V.V. Afanasev and A. Stesmans. “Photon-stimulated tunnelling of electrons in SiO_2: evidence for a defect-assisted process.” In: *Journal of Physics: Condensed Matter* 9 (1997), pp. L55–L60.

[105] A.M. El-Sayed et al. “Nature of intrinsic and extrinsic electron trapping in SiO_2.” In: *Physical Review B* 89 (2014), p. 125201.

[106] W. Shockley and Jr. W.T. Read. “Statistics of the Recombination of Holes and Electrons.” In: *Physical Review* 87 (1952), pp. 835–842.

[107] R.N. Hall. “Electron-Hole Recombination in Germanium.” In: *Physical Review* 87 (1952), p. 387.

[108] P.M. Lenahan and J.F. Conley Jr. “What can electron paramagnetic resonance tell us about the Si/SiO_2 system?” In: *Journal of Vacuum Science & Technology B* 16 (1998), pp. 2134–2153.

[109] P. Déak et al. “A Cause for SiC/SiO_2 Interface States: the Site Selection of Oxygen in SiC.” In: *Materials Science Forum* 433-436 (2003), pp. 535–538.

[110] J.L. Cantin et al. “Identification of the Carbon Dangling Bond Center at the 4H-SiC/SiO2 Interface by an EPR Study in Oxidized Porous SiC.” In: *Physical Review Letters* 92 (2004), p. 015502.

[111] D.J. Meyer, P.M. Lenahan, and A.J. Lelis. “Observation of trapping defects in 4H-silicon carbid metal-oxide-semiconductor field-effect transistors by spin-dependent recombination.” In: *Applied Physics Letters* 86 (2005), p. 023503.

[112] J. Isoya et al. “ESR Characterization of SiC Bulk Crystals and SiO_2/SiC Interface.” In: *Materials Science Forum* 389-393 (2002), pp. 1025–1028.

[113] P.J. Macfarlane and M.E. Zvanut. “Characterization of paramagnetic derfect centers in three polytypes of dry heat treated, oxidized SiC.” In: *Journal of Applied Physics* 88 (2000), pp. 4122–4127.

[114] T. Hosoi et al. “Investigation of Surface and Interface Morphology of Thermally Grown SiO_2 Dielectrics on 4H-SiC(0001) Substrates.” In: *Materials Science Forum* 679-680 (2011), pp. 342–345.

[115] P. Fiorenza et al. “Influence of the surface morphology on the channel mobility of lateral implanted 4H-SiC(0001) metal-oxide-semiconductor field-effect transistors.” In: *Journal of Applied Physics* 112 (2012), p. 084501.

[116] K.C. Chang et al. “High-carbon concentrations at the silicon dioxide-silicon carbide interface identified by electron energy loss spectroscopy.” In: *Applied Physics Letters* 77 (2000), pp. 2186–2188.

[117] C. Strenger et al. “Comparative Study of Electrical and Microstructural Properties of 4H-SiC MOSFETs.” In: *Materials Science Forum* 717-720 (2012), pp. 437–440.

[118] J.H. Dycus et al. “Structure and chemistry of passivated SiC/SiO_2 interfaces.” In: *Applied Physics Letters* 108 (2016), p. 201607.

[119] H. Shiomi et al. “Electrical and physical characterizations of the effects of oxynitridation and wet oxidation at the interface of SiO_2/4H-SiC(0001) and (000$\bar{1}$).” In: *Japanese Journal of Applied Physics* 55 (2016), 04ER19.

[120] J. Taillon et al. “Characterization of the Oxide-Seminconductor Interface in 4*H*-SiC/SiO_2 Structures using TEM and XPS.” In: *Microscopy and Microanalysis* 21 (2015), pp. 1537–1538.

[121] G.Y. Chung et al. “Effect of nitric oxide annealing on the interface trap densities near the band edges in the 4H polytype of silicon carbide.” In: *Applied Physics Letters* 76 (2000), pp. 1713–1715.

[122] P. Jamet, S. Dimitrijev, and P. Tanner. “Effects of nitridation in gate oxides grown on 4H-SiC.” In: *Journal of Applied Physics* 90 (2001), pp. 5058–5063.

[123] G. Liu et al. "Enhanced Inversion Mobility on 4H-SiC ($11\bar{2}0$) Using Phosphorus and Nitrogen Interface Passivation." In: *IEEE Electron Device Letters* 34 (2013), pp. 181–183.

[124] T. Umeda et al. "Behavior of nitrogen atoms in SiC-SiO_2 interfaces studied by electrically detected magnetic resonance." In: *Applied Physics Letters* 99 (2011), p. 142105.

[125] P. Jamet and S. Dimitrijev. "Physical properties of N_2O and NO-nitrided gate oxides grown on 4H SiC." In: *Applied Physics Letters* 79 (2001), pp. 323–325.

[126] Y. Xu et al. "Atomic state and characterization of nitrogen at the SiC/SiO_2 interface." In: *Journal of Applied Physics* 115 (2014), p. 033502.

[127] R. Kosugi, T. Umeda, and Y. Sakuma. "Fixed nitrogen atoms in the SiO_2/SiC interface region and their direct relationship to interface trap density." In: *Applied Physics Letters* 99 (2011), p. 182111.

[128] K.C. Chang et al. "High-resolution elemental profiles of the silicon dioxide/4H-silicon carbide interface." In: *Journal of Applied Physics* 97 (2005), p. 104920.

[129] J. Rozen et al. "Density of interface states, electron traps, and hole traps as a function of the nitrogen density in SiO_2 on SiC." In: *Journal of Applied Physics* 105 (2009), p. 124506.

[130] H. Yoshioka, T. Nakamura, and T. Kimoto. "Generation of very fast states by nitridation of the SiO_2/SiC interface." In: *Journal of Applied Physics* 112 (2012), p. 024520.

[131] G. Rescher, G. Pobegen, and T. Aichinger. "Impact of Nitric Oxide Post Oxidation Anneal on the Bias Temperature Instability and the On-Resistance of 4H-SiC nMOSFETs." In: *Materials Science Forum* 821-823 (2015), pp. 709–712.

[132] P. Fiorenza et al. "Comparative study of gate oxide in 4H-SiC lateral MOSFETs subjected to post-deposition-annealing in N_2O and $POCl_3$." In: *Applied Physics A* 115 (2014), pp. 333–339.

[133] R. Morishita et al. "Effect of $POCl_3$ Annealing on Reliability of Thermal Oxides Grown on 4H-SiC." In: *Matrerials Science Forum* 717-720 (2012), pp. 739–742.

[134] J.A. Weil, J.R. Bolton, and E. Wertz. *Electron Paramagnetic Resonance - Elementary Theory and Practical Applications.* John Wiley & Sons, 1994.

[135] H. Itoh et al. "Intrinsic Defects in Cubic Silicon Carbide." In: *Physica Status Solidi A* 162 (1997), pp. 173–198.

[136] T. Wimbauer et al. "Negatively charged Si vacancy in 4H SiC: A comparison between theory and experiment." In: *Physical Review B* 56 (1997), pp. 7384–7388.

[137] M. Hundshausen et al. "Characterization of defects in silicon carbide by Raman spectroscopy." In: *Physica Status Solidi B* 245 (2008), pp. 1356–1368.

[138] M. Bockstedte et al. "Identification of intrinsic defects in SiC: Towards an understanding of defect aggregates by combining theoretical and experimental approaches." In: *Physica Status Solidi B* 245 (2008), pp. 1281–1297.

[139] T. Umeda et al. "EPR identification of two types of carbon vacancies in 4H-SiC." In: *Physical Review B* 69 (2004), p. 121201.

[140] EPR in Semiconductors - Spin-Hamiltonian parameter database for defects in semiconductors. *http://www.kc.tsukuba.ac.jp/div-media/epr/tutorials/database.php.*

[141] J. Isoya et al. "EPR identification of intrinsic defects in SiC." In: *Physica Status Solidi B* 245 (2008), pp. 1298–1314.

[142] E. Janzén et al. “Defects in Microelectronic Materials and Devices.” In: ed. by D.M. Fleetwood, S.T. Pantelides, and R.D. Schrimpf. Taylor & Francis Group, 2008. Chap. Defects in SiC, pp. 615–670.

[143] J.R. Weber et al. “Defects in SiC for quantum computing.” In: *Journal of Applied Physics* 109 (2011), p. 102417.

[144] W.F. Koehl et al. “Room temperature coherent control of defect spin qubits in silicon carbide.” In: *Nature* 479 (2011), pp. 84–87.

[145] L. Gordon, A. Janotti, and C.G. van de Walle. “Defects as qubits in 3C- and 4H-SiC.” In: *Physical Review B* 92 (2015), p. 045208.

[146] M. Widmann et al. “Coherent control of single spins in silicon carbide at room temperature.” In: *Nature Materials* 14 (2015), pp. 164–168.

[147] H.J. von Bardeleben et al. “Identification and magneto-optical properties of the NV center in 4H-SiC.” In: *Physical Review B* 92 (2015), p. 064104.

[148] N.T. Son et al. “Divacancy in SiC.” In: *Physical Review Letters* 96 (2006), p. 055501.

[149] P.G. Baranov et al. “Identification of the carbon antisite in SiC: EPR of ^{13}C enriched crystals.” In: *Physical Review B* 77 (2008), p. 085120.

[150] U. Gerstmann et al. “$Si_C C_{Si}$ antisite pairs in SiC identified as paramagnetic defects with strongly anisotropic orbital quenching.” In: *Physical Review B* 81 (2010), p. 195208.

[151] T. Umeda et al. “Identification of the Carbon Antisite-Vacancy Pair in 4H-SiC.” In: *Physical Review Letters* 96 (2006), p. 145501.

[152] N.T. Son et al. “Defects and carrier compensation in semi-insulating 4H-SiC substrates.” In: *Physical Review B* 75 (2007), p. 155204.

[153] L. Torpo et al. “Comprehensive *ab initio* study of properties of monovacancies and antisites in 4H-SiC.” In: *Journal of Physics: Condensed Matter* 13 (2011), pp. 6203–6231.

[154] T. Umeda et al. “EPR and theoretical studies of positively charged carbon vacancy in 4H-SiC.” In: *Physical Review B* 70 (2004), p. 235212.

[155] T. Umeda et al. “EPR and theoretical studies of negatively charged carbon vacancy in 4H-SiC.” In: *Physical Review B* 71 (2005), p. 193202.

[156] N.T. Son, P.N. Hai, and E. Janzén. “Carbon vacancy-related defect in 4H and 6H SiC.” In: *Physical Review B* 63 (2001), p. 201201.

[157] N.T. Son, P.N. Hai, and E. Janzén. “Silicon Antisite in SiC.” In: *Physical Review Letters* 87 (2001), p. 045502.

[158] X.T. Trinh et al. “Negative-U carbon vacancy in 4H-SiC: Assessment of charge correction schemes and identification of the negative carbon vacancy at the quasicubic site.” In: *Physical Review B* 88 (2013), p. 235209.

[159] N.T. Son et al. “Negative-U System of Carbon Vacancy in 4H-SiC.” In: *Physical Review Letters* 109 (2012), p. 187603.

[160] X.T. Trinh et al. “Identification of the Negative Carbon Vacancy at Quasi-Cubic Site in 4H-SiC by EPR and Theoretical Calculations.” In: *Materials Science Forum* 778-780 (2014), pp. 285–288.

[161] K. Kawahara et al. “Quantitative comparison between $Z_{1/2}$ center and carbon vacancy in 4H-SiC.” In: *Journal of Applied Physics* 115 (2014), p. 143705.

[162] E. Sörman et al. "Silicon vacancy related defect in 4H and 6H SiC." In: *Physical Review B* 61 (2000), pp. 2613–2620.

[163] N. Mizuoshi et al. "Continuous-wave and pulsed EPR study of the negatively charged silicon vacancy with S=3/2 and C3v symmetry in n-type 4H-SiC." In: *Physical Review B* 66 (2002), p. 235202.

[164] N. Mizuoshi et al. "Spin multiplicity and charge state of a silicon vacancy (TV2a) in 4H-SiC determined by pulsed ENDOR." In: *Physical Review B* 72 (2005), p. 235208.

[165] P.G. Baranov et al. "Silicon vacancy in SiC as a promising quantum system for single-defect and single-photon spectroscopy." In: *Physical Review B* 83 (2011), p. 125203.

[166] V.A. Soltamov et al. "Room Temperature Coherent Spin Alignment of Silicon Vacancies in 4H- and 6H-SiC." In: *Physical Review Letters* 108 (2012), p. 226402.

[167] E. Rauls et al. "Metastability of the Neutral Silicon Vacancy in 4H-SiC." In: *Physica Status Solidi B* 217 (2000), R1–R3.

[168] T. Umeda et al. "Electron Paramagnetic Resonance Study of Carbon Antisite-Vacancy Pair in *p*-type 4H-SiC." In: *Materials Science Forum* 556-557 (2007), pp. 453–456.

[169] T. Umeda et al. "Identification of positively charged carbon antisite-vacancy pairs in 4H-SiC." In: *Physical Review B* 75 (2007), p. 245202.

[170] L. Torpo, T.E.M. Staab, and R.M. Nieminen. "Divacancy in 3C- and 4H-SiC: An extremely stable defect." In: *Physical Review B* 65 (2002), p. 085202.

[171] V.S. Vainer and V.A. Il'in. "Electron spin resonance of exchange-coupled vacancy pairs in hexagonal silicon carbide." In: *Soviet Physics, Solid State* 23 (1981), pp. 2126–2133.

[172] O.V. Zwier et al. "All-optical coherent population trapping with defect spin ensembles in silicon carbide." In: *Scientific Reports* 5 (2015), p. 10931.

[173] U. Gerstmann et al. "Formation and annealing of nitrogen-related complexes in SiC." In: *Physical Review B* 67 (2003), p. 205202.

[174] M. Bockstedte, M. Mattausch, and O. Pankratov. "The solubility and defect equilibrium of the n-type dopants nitrogen and phosphorus in 4H-SiC: a theoretical study." In: *Materials Science Forum* 457-460 (2004), pp. 715–718.

[175] U. Gerstmann et al. "Nitrogen Donor Aggregation in 4H-SiC: *g*-Tensor Calculations." In: *Materials Science Forum* 556-557 (2007), pp. 391–394.

[176] B.R. Tuttle et al. "Theory of hyperfine active nitrogen complexes observed in 4H-SiC diodes." In: *Journal of Applied Physics* 114 (2013), p. 113712.

[177] M.E. Zvanut and J. van Tol. "Nitrogen-related point defect in 4H and 6H SiC." In: *Physica B* 401-402 (2007), pp. 73–76.

[178] D.V. Savchenko et al. "Spin-coupling in Heavily Nitrogen-doped 4H-SiC." In: *Materials Science Forum* 615-617 (2009), pp. 343–346.

[179] V.S. Vainer and V.A. Il'in. "ESR of close nitrogen-vacancy pairs in n-type 6-H SiC." In: *Soviet Physics, Solid State* 23 (1981), p. 1432.

[180] M.V. Muzafarova et al. "Identification of the triplet state N-V defect in neutron irradiated silicon carbide by Electron Paramagnetic Resonance." In: *Materials Science Forum* 527-529 (2006), pp. 555–558.

[181] I.V. Ilyin et al. "Electron paramagnetic resonance studies of multi-defect clusters in neutron irradiated silicon carbide." In: *Semiconductor Science and Technology* 22 (2007), pp. 270–278.

[182] E. Kalabukhova et al. "EPR study of the nitrogen containing defect center created in self-assembled 6H SiC nanostructure." In: *Materials Science Forum* 740-742 (2013), pp. 389–392.

[183] Y. Nishi. "Study of Silicon-Silicon Dioxide Structure by Electron Spin Resonance I." In: *Japanese Journal of Applied Physics* 10 (1971), pp. 52–62.

[184] E. Cartier, J.H. Stathis, and D.A. Buchanan. "Passivation and depassivation of silicon dangling bonds at the Si/SiO2 interface by atomic hydrogen." In: *Applied Physics Letters* 63 (1993), pp. 1510–1512.

[185] T. Umeda et al. "SiC MOS Interface States: Similarity and Dissimilarity from Silicon." In: *ECS Transactions* 50 (2013), pp. 305–311.

[186] J.L. Cantin et al. "Hydrogen passivation of carbon Pb like centers at the 3C- and 4H-SiC/SiO2 interface in oxidized porous SiC." In: *Applied Physics Letters* 88 (2006), p. 092108.

[187] H.J. von Bardeleben et al. "Microscopic Structure and Electrical Activity of 4H-SiC/SiO_2 Interface Defects : an EPR study of oxidized porous SiC." In: *Materials Science Forum* 457-460 (2004), pp. 1457–1462.

[188] T. Umeda et al. "Electrically detected ESR study of interface defects in 4H-SiC metal-oxide-semiconductor field effect transistor." In: *Materials Science Forum* 679-680 (2011), pp. 370–373.

[189] M.A. Anders, P.M. Lenahan, and A.J. Lelis. "Are dangling bond centers important interface traps in 4H-SiC metal oxide semiconductor field effect transistors?" In: *Applied Physics Letters* 109 (2016), p. 142106.

[190] D.J. Meyer et al. "Structure of 6H silicon carbide-silicon dioxide interface trapping defects." In: *Applied Physics Letters* 84 (2004), p. 3406.

[191] M.S. Dautrich, P.M. Lenahan, and A.J. Lelis. "Identification of trapping defects in 4H-silicon carbide metal-insulatorsemiconductor field-effect transistors by electrically detected magnetic resonance." In: *Applied Physics Letters* 89 (2006), p. 223502.

[192] B.C. Bittel et al. "Spin dependent charge pumping in SiC metal-oxide-semiconductor field-effect-transistors." In: *Applied Physics L* 99 (2011), p. 083504.

[193] C.J. Cochrane, P.M. Lenahan, and A.J. Lelis. "An electrically detected magnetic resonance study of performance limiting defects in SiC metal oxide semiconductor field effect transistors." In: *Journal of Applied Physics* 109 (2011), p. 014506.

[194] C.J. Cochrane, P.M. Lenahan, and A.J. Lelis. "Identification of a silicon vacancy as an important defect in 4H SiC metal oxide semiconducting field effect transistor using spin dependent recombination." In: *Applied Physics Letters* 100 (2012), p. 023509.

[195] C.J. Cochrane. "Development of new atomic scale defect identification schemes in micro/nanoelectronics incorporating digital signal processing methods for investigating zero/low field spin dependent transport and passage effects in electrically defected magnetic resonance." PhD thesis. Pennsylvania State University, 2013.

[196] C.J. Cochrane, P.M. Lenahan, and A.J. Lelis. "The effect of nitric oxide anneals on silicon vacancies at and very near the interface of 4H SiC metal oxide semiconducting field effect transistors using electrically detected magnetic resonance." In: *Applied Physics Letters* 102 (2013), p. 193507.

[197] T. Aichinger and P.M. Lenahan. “Giant amplification of spin dependent recombination at heterojunctions through a gate controlled bipolar effect.” In: *Applied Physics Letters* 101 (2012), p. 083504.

[198] M.A. Anders, P.M. Lenahan, and A.J. Lelis. “Negative bias instability in 4H-SiC MOSFETS: Evidence for structural changes in the SiC.” In: *2015 IEEE International Reliability Physics Symposium* (2015), 3E.4.1–3E.4.5.

[199] M.A. Anders et al. “Relationship Between the 4H-SiC/SiO_2 Interface Structure and Electronic Properties Explored by Electrically Detected Magnetic Resonance.” In: *IEEE Transactions on Electron Devices* 62 (2015), pp. 301–308.

[200] E. Zavoisky. “Paramagnetic relaxation of liquid solutions for perpendicular fields.” In: *Journal of Physics* 9 (1945), pp. 211–216.

[201] E. Zavoisky. “Spin-magnetic resonance in paramagnetics.” In: *Journal of Physics USSR* 9 (1945), pp. 211–245.

[202] A. Lund, M. Shiotani, and S. Shimada. *Priciples and applications of ESR spectroscopy.* Springer, 2011.

[203] M. Stutzmann, M.S. Brandt, and M.W. Bayerl. “Spin-dependent processes in amorphous and microcrystalline silicon: a survey.” In: *Journal of Non-Crystalline Solids* 266-269 (2000), pp. 1–22.

[204] J.J. Davies. “Optically-detected magnetic resonance and its applications.” In: *Contemporary Physics* 17 (1976), pp. 275–294.

[205] D.J. Lépine. “Spin-Dependent Recombination on Silicon Surface.” In: *Physical Rev. B* 6 (1972), pp. 436–441.

[206] D. Kaplan, I. Solomon, and N.F. Mott. “Explanation of the Large Spin-Dependent Recombination Effect in Semiconductors.” In: *Le Journal de Physique - Lettres* 39 (1978), pp. 51–54.

[207] J.P. Poole. *Electron Spin Resonance - A Comprehensive Treatise on Experimental Techniques.* Dover Publications, 1996.

[208] G.D. Watkins. “EPR and ENDOR Studies of Defects in Semiconductors.” In: *Semiconductors and Semimetals* 51 (1998), pp. 1–43.

[209] S.Y. Lee et al. “Modulation frequency dependence of continuous-wave optically/electrically detected magnetic resonance.” In: *Physical Review B* 86 (2012), p. 115204.

[210] M.A. Jupina and P.M. Lenahan. “A spin dependent recombination study of radiation induced defects at and near the Si/SiO_2 interface.” In: *IEEE Transactions on Nuclear Science* 36 (1989), pp. 1800–1807.

[211] M. Fanciulli et al. “Defects at the high-k/semiconductor interfaces investigated by spin dependent spectroscopies.” In: *Defects in High-k Gate Dielectric Stacks: Nano-Electronic Semiconductor Devices* 220 (2006), pp. 263–276.

[212] B. Stich, S. Greulich-Weber, and J.M. Spaeth. “Electrical detection of electron paramagnetic resonance: New possibilities for the study of point defects.” In: *Journal of Applied Physics* 77 (1995), pp. 1546–1553.

[213] F. Hoehne et al. “Spin-Dependent Recombination between Phosphorus Donors in Silicon and Si/SiO_2 Interface States Investigated with Pulsed Electrically Detected Electron Double Resonance.” In: *Physical Review Letters* 104 (2010), p. 046402.

[214] J.S. Brugler and P.G.A. Jespers. "Charge pumping in MOS devices." In: *IEEE Transactions on Electron Devices* 16 (1969), pp. 297–302.

[215] G. Groesenenken et al. "A Reliable Approach for Charge-Pumping Measurements in MOS Transistors." In: *IEEE Transactions on Electron Devices* 31 (1984), pp. 42–53.

[216] G. Gruber et al. "An Extended EDMR Setup for SiC Defect Characterization." In: *Materials Science Forum* 740-742 (2013), pp. 365–368.

[217] R. Meszaros. "Cryogenic Electrically Detected Magnetic Resonance of the SiC-SiO_2 Interface." MA thesis. Graz University of Technology, 2016.

[218] C. Elliot et al. "National Instruments LabVIEW: A Programming Environment for Laboratory Automation and Measurement." In: *Journal of Laboratory Automation* 12 (2007), pp. 17–24.

[219] J. Krzystek et al. "DPPH as a Standard for High-Field EPR." In: *Journal of Magnetic Resonance* 125 (1997), pp. 207–211.

[220] MathWorks, Inc., USA. *www.mathworks.com.*

[221] T. Umeda et al. "C-face interface defects in 4H-SiC MOSFETs studied by electrically detected magnetic resonance." In: *Materials Science Forum* 778-780 (2014), pp. 414–417.

[222] T. Aichinger, P.M. Lenahan, and D. Peters. "Interface defects and negative bias temperature instabilities in 4H-SiC PMOSFETs - a combined DCIV/SDR study." In: *Materials Science Forum* 740-742 (2013), pp. 529–532.

[223] F. Jensen. "The Basis Set Convergence of Spin-Spin Coupling Constants Calculated by Density Functional Methods." In: *Journal of Chemical Theory and Computation* 2 (2006), pp. 1360–1369.

[224] D.B. Williams and C.B. Carter. *Transmission Electron Microscopy - A Textbook for Materials Science*. Springer, 2009.

[225] Austrian Centre for Electron Microscopy and Nanoanalysis, FELMI-ZFE (Austria). *www.felmi-zfe.at.*

[226] FEI Company (USA). *www.fei.com.*

[227] Gatan, Inc. (USA). *www.gatan.com.*

[228] Gatan EELS Atlas. *www.eels.info/atlas.*

[229] G. Pensl et al. "Implantation-induced dedefect in silicon carbide." In: *Physica B* 340-342 (2003), pp. 121–127.

[230] J. Cottom et al. "Identifying Performance Limiting Defects in Silicon Carbide pn-junctions: A Theoretical Study." In: *Materials Science Forum* 858 (2016), pp. 257–260.

[231] J. Cottom et al. "A theoretical study of the passivation of the $N_C V_{Si}$ defect within N-implanted pn-junctions." In: (2016). manuscript in preparation.

[232] I.V. Ilyin et al. "Electron paramagnetic resonance studies of multi-defect clusters in neutron irradiated silicon carbide." In: *Semiconductor Science and Technology* 22 (2007), pp. 270–278.

[233] C.J. Cochrane, P.M. Lenahan, and A.J. Lelis. "Direct observation of lifetime killing defects in 4 H SiC epitaxial layers through spin dependent recombination in bipolar junction transistors." In: *Applied Physics Letters* 105 (2009), p. 064502.

[234] C.J. Cochrane, P.M. Lenahan, and A.J. Lelis. "Zero-field detection of spin dependent recombination with direct observation of electron nuclear hyperfine interactions in the absence of an oscillating electromagnetic field." In: *Journal of Applied Physics* 112 (2012), p. 123714.

[235] J. VandeVondele et al. "Quickstep: Fast and accurate density functional calculations using a mixed Gaussian and plane waves approach." In: *Computer Physics Communications* 167 (2005), pp. 103–128.

[236] J.P. Perdew, K. Burke, and M. Ernzerhof. "Generalized Gradient Approximation Made Simple." In: *Physical Review Letters* 77 (1996), pp. 3865–3868.

[237] K. Hummer, J. Harl, and G. Kresse. "Heyd-Scuseria-Ernzerhof hybrid functional for calculating the lattice dynamics of semiconductors." In: *Physical Review B* 80 (2009), p. 115205.

[238] B.C. Bittel. "Study of defect structure and electrical transport in back end of line dielectrics and SiC MOSFETs." PhD thesis. Pennsylvania State University, 2012.

[239] V.V. Afanasev and A. Stesmans. "Hole traps in oxide layers thermally grown on SiC." In: *Applied Physics Letters* 69 (1996), pp. 2252–2254.

[240] J. Cottom. *UCL London, private communication.*

[241] T. Aichinger et al. "In Situ Poly Heater - A Reliable Tool for Performing Fast and Defined Temperature Switches on Chip." In: *IEEE Transactions on Device and Materials Reliability* 10 (2010), pp. 3–8.

[242] T.H. Ning, C.M. Osburn, and H.N. Yu. "Emission probability of hot electrons from silicon into silicon dioxide." In: *Journal of Applied Physics* 48 (1977), pp. 286–293.

[243] T.H. Ning. "Hot-electron emission from silicon into silicon dioxide." In: *Solid-State Electronics* 21 (1978), pp. 273–282.

[244] M.G. Ancona, N.S. Saks, and D. McCarthy. "Lateral distribution of hot-carrier-induced interface traps in MOSFETs." In: *IEEE Transactions on Electron Devices* 35 (1988), pp. 2221–2228.

[245] T. Aichinger and M. Nelhiebel. "Advanced Energetic and Lateral Sensitive Charge Pumping Profiling Methods for MOSFET Device Characterization - Analytical Discussion and Case Studies." In: *IEEE Transactions on Device and Materials Reliability* 8 (2008), pp. 509–518.

[246] Vienna University of Technology. *http://www.iue.tuwien.ac.at/index.php?id=205.*

[247] A. Dorda. *Graz University of Technology, private communication.*

[248] E. Bano et al. "Hot carrier-induced photon emission in 6H and 4H-SiC MOSFETs." In: *Solid-State Electronics* 44 (2000), pp. 63–69.

[249] L. Yu et al. "Channel Hot-Carrier Effect of 4H-SiC MOSFET." In: *Materials Science Forum* 615-617 (2009), pp. 813–816.

[250] E. Pippel et al. "Interfaces between 4H-SiC and Si O 2 : Microstructure, nanochemistry, and near-interface traps." In: *Journal of Applied Physics* 97 (2005), p. 034302.

[251] Austrian Research Promotion Agency FFG. *Project 850220.*

[252] C. Gspan. *Austrian Centre for Electron Microscopy and Nanoanalysis, FELMI-ZFE, private communication.*

[253] B.L. Welch. "The Generalization of Student′s Problem when Several Different Population Variances are Involved." In: *Biometrika* 34 (1947), pp. 28–35.

[254] C.F. Egerton. "Limits to the spatial, energy and momentum resolution of electron energy-loss spectroscopy." In: *Ultramicroscopy* 107 (2007), pp. 575–586.

[255] G. Pobegen. *KAI GmbH, private communication.*

List of Figures

1.1 A close-packed hexagonal bilayer in position A (gray circles) viewed from the [0001] direction. The next bilayer can be placed on position B (solid circles) or C (dotted circles). 4
1.2 Stacking sequences and inequivalent lattice sites (h and k) of some of the most simple SiC polytypes viewed from the [11$\bar{2}$0] direction. 5
1.3 Band structures of different SiC polytypes calculated by HSE06 [25], courtesy of O.T. Hofmann [26]. 5
1.4 Schematic of a crucible for SiC crystal growth from seeded sublimation. 7
1.5 Cross sectional side view of a simple hot wall reactor. 7
1.6 Schematic of the basic principle of polytype control by step-controlled epitaxy [43]. 8
1.7 Schematic of crystal growth on an off-axis cut wafer. 9
1.8 Schematic of a SiC *n*-channel MOSFET: a) biased in the linear region, b) biased at the transition from the nonlinear to the saturation region. 11
1.9 D_{it} as a function of the energy above the valence band for different *n*- and *p*-MOS capacitors on different SiC polytypes determined by admittance spectroscopy (full symbols) and DLTS (open symbols). The conduction bands for the respective polytypes are marked by dotted lines. The Figure was taken from [68], with permission. 15

2.1 The spin-pair model suggests that an electron (green arrow) and a hole (red arrow) should be regarded in terms of their total spin S prior to recombination [206]. For $S = 1$ (triplet) recombination is forbidden, while for $S = 0$ (singlet) it is allowed. 29

3.1 Recorded transfer characteristics and fitting function to determine μ_{LF} and V_{th}. 33
3.2 Charge pumping on a SiC *n*-channel MOSFET. 34

4.1 Schematic of the experimental setup used for EDMR and EPR. 36
4.2 Biasing schemes for SDR measurements on *n*-channel MOSFETs. 38
4.3 Biasing scheme for BAE measurements. 39
4.4 Simulated EDMR curves considering different fractions of the total relative intensity (see also table 4.2) and different line profiles. The upper graphs show the full spectra which were normalized with respect to the peak-to-peak height and the lower graphs show a magnified view. 42

5.1 Signals created by the interaction of an incident high-energy electron beam with a thin specimen [224]. 43

5.2 Comparison of STEM images of the SiC-SiO_2 interface recorded with different detectors. 44
5.3 EELS spectrum of the SiC-SiO_2 interface with the labeled ionization edges of the present atom species [228]. 45
5.4 Si-$L_{2,3}$ EELS ionization edge for different positions on a linescan across the SiC-SiO_2 interface. The spectra are vertically shifted for better visibility. . . . 46
5.5 Normalized profiles of the SiC-SiO_2 interface obtained by STEM and EELS. . . 46

6.1 Normalized SDR spectra of a N-implanted *pn*-junction with B applied in different directions. 53
6.2 Formation energy of the $N_C C_{Si}$, $N_C V_{Si}$, and $N_{Si} V_C$ defects dependent on the Fermi energy with respect to the valence band edge. Reproduced from [6], with the permission of AIP Publishing. 55
6.3 Unpaired electron density (yellow) for different candidate defect models. Si atoms are blue, C are brown, N is white. Reproduced from [6], with the permission of AIP Publishing. 56
6.4 Experimental spectrum compared to simulations created with the values from Table 6.1. Reproduced from [6], with the permission of AIP Publishing. 57
6.5 Weighted simulated spectra of the $N_C V_{Si}$ at different sites calculated with pcj-1 (a) and gauged with pcj-2 and 3 (b). The sums of the curves are compared to the normalized experimental spectrum in (c), and (d) respectively. Reproduced from [6], with the permission of AIP Publishing. 58

7.1 Electrical measurements on the differently processed MOSFETs. 63
7.2 Determination of the relative device current change under resonance and its dependence on V_g. 64
7.3 Tilt maps of the different MOSFETs. 65
7.4 Normalized spectra of different MOSFETs at different microwave power levels with B applied in different crystalline directions, modified from [5]. 67
7.5 Comparison of the HF structure of the SiC-SiO_2 interface observed in different MOSFETs (a) and a comparison of an experimental curve with the simulations of two models for the V_{Si} [191, 193, 194] (b). 68
7.6 Normalized experimental and simulated BAE spectra of a O_2 annealed MOSFET (upper), 4× magnified (middle), and 20× magnified (lower). 71
7.7 Schematic of different examples P_{bC} centers at the Si-face SiC-SiO_2 interface: (1) interfacial V_{Si}, (2) P_{bC} center due to relaxation, (3) P_{bC} center at a corner, (4) C bond pointing downwards, (5) bulk V_{Si}. 72
7.8 Normalized BAE spectra of sample therm. w/ N_2O at different microwave power levels (left), and 10× magnified (right). 74
7.9 Normalized BAE spectra of an N_2O annealed MOSFET at different gate voltages (left), and 12× magnified (right). 75
7.10 Normalized BAE spectra of an N_2O annealed MOSFET at different temperatures (upper), and 12× magnified (lower). 76
7.11 Normalized experimental BAE curve and simulation of sample dep. w/ N_2O with the magnetic field applied in the [0001] direction (a). Residuals of the spectra recorded at different temperatures and subtracted by the respective simulated curve (b). 77
7.12 Tilt series of an N_2O annealed MOSFET. The spectra are magnified and vertically shifted in order to follow the low-intensity lines. 78

7.13 Angular dependence of the C dangling bond and the unknown doublet defect. . 79

8.1 Simulation of the potential distributions in a Si MOSFET in different biasing regimes. Calculations were performed using the minimos-NT 2.1 device simulator [246], courtesy of A. Dorda [247]. 82
8.2 Comparison of the BAE signals of a virgin device and one that received HCS. For the latter the BAE measurement was once recorded at the drain with carrier injection from the source (pink) and once vice versa (black). 84
8.3 Electrical measurements after different stress steps. 85
8.4 Normalized BAE spectra of an NO-annealed SiC MOSFET after different times of HCS with B applied in different directions (modified from [3]). 86
8.5 Tilt map of the virgin MOSFET and after 10^6 s if HCS. 0° corresponds to B applied in the $[11\bar{2}0]$ direction, and 90° to the [0001] direction. 86
8.6 Comparison of the BAE spectra of the 10^6 s stressed MOSFET with reference spectra from chapters 6 and 7. 87

9.1 Overview ADF images of the studied lamellas. 90
9.2 High resolution BF images of the SiC-SiO_2 interface at different magnifications. 91
9.3 Measurement of length and height of a macrostep. 92
9.4 Step distributions for O_2- (upper) and NO-annealed sample (lower). 92
9.5 EELS profiles extracted from equally sized 2D-EELS scans at different orientations of the SiC-SiO_2 interface of the two samples. 94
9.6 Energy loss region of N edge for the two samples. The spectra were normalized with respect to the O edge at $E_{\mathrm{loss}} \approx 535\,\mathrm{eV}$ (upper). Subtracting the spectra clearly reveals the N edge at $E_{\mathrm{loss}} \approx 403\,\mathrm{eV}$ (lower). 96
9.7 Comparison of different extracted data of $\approx 15\,\mathrm{nm} \times 45\,\mathrm{nm}$ 2D-EELS scans of the two samples revealing an increased N-content at the SiC-SiO_2 interface of the sample with NO. 97

C.1 A series of spectra selected from a linescan (a) and their numerical derivatives (b), note that the black lines are the derivatives after smoothing the initial spectra. The selected series of spectra is indicated by the circle in the resulting profile (c). 110

D.1 Temperature dependent resistance of a poly-heater structure, courtesy of G. Pobegen [255]. 111

List of Tables

1.1 Properties of the most simple SiC polytypes [22, 23]. 4
1.2 Material properties of 4H-SiC compared to other semiconductors [22, 31, 32, 33]. 6

2.1 Natural abundances $\mathcal{N}$ and nuclear spin I of the paramagnetic isotopes of the most important elements present in SiC devices [134]. 26

4.1 Possible $m_{I,i}$ values and their respective probabilities P_i for C, Si, and N [134]. 40
4.2 Influence of the probability threshold on the total simulated intensity, the number of lines, and the included interactions for a simulation of the N_CV_{Si} defect. This table was generated by the program as printed in appendix B. 42

6.1 Calculated HF splitting constants a_k for the N_CV_{Si} and the N_CC_{Si}. The parameters have been averaged over the equivalent atoms of each shell. a_{C1} stands for the nn1 C atoms, a_{Si2} for the nn2 Si atoms, and a_{C3} stands for the nn3 C atoms. 56

7.1 Processing parameters of the studied n-channel MOSFETs. 62
7.2 Device properties determined by electrical measurements of the studied n-channel MOSFETs. 63
7.3 Principal g-factors determined by fitting according to equation (29). 66

8.1 Experimental parameters determined for the measured MOSFET after different stress times [3]. 84

9.1 Device properties determined by electrical measurements of the studied samples, more details on these devices are found in chapter 7. 90
9.2 Interface thickness t_{int} determined by the Z-contrast, the O and C intensities, and the chemical shift of the Si-$L_{2,3}$ edge, as indicated by the indices. 95

A.1 HF data of different paramagnetic N_CV_{Si} charge states for an initial comparison. The splitting constants a_k (in Gauss) of the atomic sites k are shown. For the neutral charge state (0) a low spin state (doublet) and a high spin state (quartet) exists. 101
A.2 HF data of inequivalent sites of the $N_CV_{Si}{}^0$. The first letter indicates whether the V_{Si} is in an h or k site and the second letter indicates the same thing for the N_C. 102

Acronyms

2H hexagonal crystal with a bilayer periodicity of 2.

3C cubic crystal.

4H hexagonal crystal with a bilayer periodicity of 4.

6H hexagonal crystal with a bilayer periodicity of 6.

ADC analog-to-digital converter.

ADF annular dark field.

Al aluminum.

Al_{Si} substitutional aluminum at the silicon site.

As arsenic.

B boron.

BAE bipolar amplification effect.

Be beryllium.

BF bright field.

Bi bismuth.

C carbon.

C_3H_8 propane.

C_i carbon interstitial.

C_{Si} carbon antisite.

$C_{Si}V_C$ C_{Si} coupled to a V_C.

CO carbon monoxide.

CO_2 carbon dioxide.

CVD chemical vapor deposition.

DAC digital-to-analog converter.

DFT density functional theory.

DLTS deep level transient spectroscopy.

DMOSFET double-diffused MOSFET.

DPPH 2,2-diphenyl-1-picrylhydrazyl.

EDMR electrically detected magnetic resonance.

EDS energy-dispersive x-ray spectroscopy.

EELS electron energy loss spectroscopy.

ELNES energy-loss near-edge structure.

EPR electron paramagnetic resonance.

FIB focused ion beam.

Ga gallium.

GaAs gallium arsenide.

GaN gallium nitride.

GAPW Gaussian augmented-plane wave.

H hydrogen.

h hexagonal.

H_2 dihydrogen.

HAADF high-angle annular dark field.

HCS hot carrier stress.

HF hyperfine.

IGBT insulated-gate bipolar transistor.

JFET junction gate field-effect transistor.

k cubic.

LED light-emitting diode.

MESFET metal-semiconductor field effect transistor.

MOS metal-oxide-semiconductor.

MOSFET metal-oxide-semiconductor field effect transistor.

N nitrogen.

N_2O nitrous oxide.

N_C substitutional nitrogen at the carbon site.

$N_C C_{Si}$ N_C coupled to a C_{Si}.

$N_C N_{Si}$ N_C coupled to a N_{Si}.

$N_C V_{Si}$ N_C coupled to a V_{Si}.

N_i nitrogen interstitial.

N_{Si} substitutional nitrogen at the silicon site.

$N_{Si} V_C$ N_{Si} coupled to a V_C.

N_x N_C donor pair defect.

Ni nickel.

NITs near-interface traps.

NMR nuclear magnetic resonance.

nn1 nearest neighbor.

nn2 second nearest neighbor.

nn3 third nearest neighbor.

NO nitric oxide.

NV nitrogen vacancy.

O oxygen.

O_2 diatomic oxygen.

ODMR optically detected magnetic resonance.

P phosphorus.

P_b silicon dangling bond.

P_{bC} carbon dangling bond.

PBTS positive bias temperature stress.

PL photoluminescence.

POA post-oxidation anneal.

$POCl_3$ phosphoryl chloride.

PVT physical vapor transport.

Sb antimony.

SDR spin dependent recombination.

Si silicon.

Si$(OC_2H_5)_4$ tetraethyl orthosilicate.

Si$_C$ silicon antisite.

Si$_C$$C_{Si}$ antisite pair.

SiC silicon carbide.

SiH$_4$ silane.

SIMS secondary ion mass spectroscopy.

SiO$_2$ silicon dioxide.

SiO$_x$$N_y$ silicon oxynitride.

STEM scanning transmission electron microscopy.

T$_{V2a}$ reconstructed V_{Si}.

TEM transmission electron microscopy.

V$_C$ carbon vacancy.

V$_C$$V_{Si}$ divacancy.

V$_{Si}$ silicon vacancy.

V$_{Si}$ $(N_C)_4$ fully N-passivated V_{Si}.

XPS x-ray photoelectron spectroscopy.

Symbols

Symbol	Description	Unit
A_g	Gate area	cm^2
A_iso	Isotropic HF coupling constant	eV
A_k	HF coupling constant of the k-th atom	eV
B	Applied magnetic field	G
B_0	Resonance field without HF interaction	G
B_mod	Modulation field	G
B_res	Resonance magnetic field	G
C_ox	Oxide capacitance	$\mathrm{F\,cm^{-2}}$
C_s	Spherical aberration	nm
D	Electron dipole-dipole coupling parameter	eV
D_it	Density of interface traps	$\mathrm{cm^{-2}\,eV^{-1}}$
E	Energy	eV
E_F	Fermi energy	eV
E_V	Energy of the valence band	eV
E_bulk	Total energy of a defect-free supercell	eV
E_form	Formation energy	eV
E_i	Intrinsic Fermi energy	eV
E_loss	Electron energy loss	eV
I	Nuclear spin	
I_bulk	Bulk contribution to the current	A
I_cp	Charge pumping current	A
I_d	Drain current	A
L	Channel length	μm
N	Number of considered atoms	
N_a	Acceptor density	$\mathrm{cm^{-3}}$
N_d	Donor density	$\mathrm{cm^{-3}}$
P	Probability	
P_i	Probability	
P_{i_k}	Probability	
P_mw	Microwave power	W
P_th	Probability threshold	
Q_i	Inversion charge density	$\mathrm{C\,cm^{-2}}$
S	Electron spin	
S_i	Spin of electron i	
T	Temperature	$^\circ$C
V_d	Drain voltage	V

Symbol	Description	Unit
V_{f}	Diode forward voltage	V
V_{fb}	Flatband voltage	V
V_{g}	Gate voltage	V
V_{high}	High voltage	V
V_{low}	Base voltage	V
V_{sb}	Source-to-body voltage	V
V_{th}	Threshold voltage	V
W	Channel width	μm
Z	Atomic number	
$\mathcal{H}$	Hamiltonian	eV
$\mathcal{H}_{\mathrm{HF}}$	HF interaction Hamiltonian	eV
$\mathcal{H}_{\mathrm{LS}}$	Spin-orbit coupling Hamiltonian	eV
$\mathcal{H}_{\mathrm{Z,N}}$	Nuclear Zeeman interaction Hamiltonian	eV
$\mathcal{H}_{\mathrm{Z,e}}$	Electron Zeeman interaction Hamiltonian	eV
$\mathcal{H}_{\mathrm{dd}}$	Electron dipole-dipole interaction Hamiltonian	eV
$\mathcal{H}_{\mathrm{ee}}$	Electron-electron interaction Hamiltonian	eV
$\mathcal{H}_{\mathrm{ex}}$	Electron exchange interaction Hamiltonian	eV
$\mathcal{L}$	Lorentzian profile	
$\mathcal{N}$	Natural abundance	
$\mathcal{P}$	Total probability	
ΔE	Energy difference	eV
ΔE_{cp}	Charge pumping energy window	eV
ΔI	Current change	A
ΔI_0	Current change of the unstressed device	A
ΔV_{th}	Threshold voltage shift	V
a	$[11\bar{2}0]$ direction	Å
a_k	HF splitting constant of the k-th nucleus	G
c	Symmetry axis of a hexagonal crystal, [0001] direction	Å
f_{cp}	Charge pumping frequency	kHz
f_{mod}	Modulation frequency	Hz
f_{mw}	Microwave frequency	GHz
g	g-factor	
$g_{B\parallel c}$	g-factor with B parallel to c	
$g_{B\perp c}$	g-factor with B perpendicular to c	
g_{N}	Nuclear g-factor	
g_{e}	g-factor of the free electron, $g_e = 2.00232$	
g_{m}	Transconductance	Ω^{-1}
g_{xx}	x-component of diagonalized g-matrix	
g_{yy}	y-component of diagonalized g-matrix	
g_{zz}	z-component of diagonalized g-matrix	
$g_{\parallel}$	g-factor in symmetry direction	
$g_{\perp}$	g-factor perpendicular to the symmetry direction	
h	Planck's constant, $h = 6.62607 \cdot 10^{-34}\,\mathrm{J\,s}$	
i	Index	
i_k	Index	
j	Index	
k	Index	
k_{B}	Boltzmann constant, $k_{\mathrm{B}} = 8.617 \cdot 10^{-5}\mathrm{eV/K}$	

Symbol	**Description**	**Unit**
l	Index	
m_I	Magnetic nuclear spin quantum number	
$m_{I,i}$	Magnetic nuclear spin quantum number	
$m_{I,k}$	Magnetic nuclear spin quantum number of the k-th nucleus	
m_{I,k,i_k}	Magnetic nuclear spin quantum number of the k-th nucleus when in state i_k	
m_S	Magnetic spin quantum number	
n	Electron concentration	cm^{-3}
n_i	Intrinsic carrier density	cm^{-3}
n_s	Number of atoms of species s	
p	Hole concentration	cm^{-3}
q	Charge state	
q_e	Elementary charge, $q_\mathrm{e} = 1.602 \cdot 10^{-19}\mathrm{C}$	
r	Distance between an electron and a nucleus	Å
r_i	Coordinate of electron i	Å
r_j	Coordinate of electron j	Å
s	Index	
t_fall	Charge pumping fall time	ns
t_high	Time at high voltage	ns
t_int	Interface thickness	nm
t_low	Time at low voltage	ns
t_ox	Oxide thickness	nm
t_rise	Charge pumping rise time	ns
x	Laboratory axis	μm
y	Laboratory axis	μm
z	Laboratory axis	μm
$\mathbf{A}$	HF parameter matrix	eV
$\mathbf{A}_k$	HF parameter matrix for the k-th nucleus	eV
$\mathbf{B}$	Magnetic field vector	G
$\mathbf{D}$	Electron quadrupole parameter matrix	eV
$\mathbf{I}$	Nuclear spin operator	
$\mathbf{I}_k$	Nuclear spin operator for the k-th nucleus	
$\mathbf{L}$	Orbital angular momentum operator	
$\mathbf{S}$	Electron spin operator	
$\mathbf{T}$	Anisotropic HF coupling parameter matrix	eV
$\mathbf{g}$	g-matrix	
$\mathbf{gg}$	$\mathbf{g} \cdot \mathbf{g}^\mathrm{T}$	
$(\mathbf{gg})_{ij}$	Matrix elements of the matrix $\mathbf{gg}$	
$\mathbb{1}_3$	3×3 unity matrix	
Γ	Line broadening parameter	G
Ψ_b	Bulk potential	V
ϵ_SiC	Permittivity of SiC	$\mathrm{F\,cm}^{-1}$
λ	Spin-orbit coupling parameter	eV
μ_0	Vacuum permeability, $\mu_0 = 4\pi \cdot 10^{-7}\,\mathrm{N\,A}^{-2}$	
μ_B	Bohr magneton, $\mu_\mathrm{B} = 9.24701 \cdot 10^{-24}\mathrm{J\,T}^{-1}$	
μ_FE	Field effect mobility	$\mathrm{cm}^2\,\mathrm{V}^{-1}\,\mathrm{s}^{-1}$
μ_LF	Low field mobility	$\mathrm{cm}^2\,\mathrm{V}^{-1}\,\mathrm{s}^{-1}$

Symbol	Description	Unit
μ_N	Nuclear magneton, $\mu_\mathrm{B} = 5.05078 \cdot 10^{-27}\mathrm{J\,T^{-1}}$	
μ_eff	Effective mobility	$\mathrm{cm^2\,V^{-1}\,s^{-1}}$
μ_i	Mobility for a scattering mechanism i	$\mathrm{cm^2\,V^{-1}\,s^{-1}}$
μ_n	Mobility of electrons	$\mathrm{cm^2\,V^{-1}\,s^{-1}}$
μ_s	Chemical potential of species s	eV
μ_tot	Total mobility	$\mathrm{cm^2V^{-1}s^{-1}}$
ν	Photon frequency	GHz
ψ_e	Electron wave function	$\mathrm{m^{-3/2}}$
ρ	Areal density	$\mathrm{kg\,m^{-2}}$
θ	Angle	$^\circ$
$\boldsymbol{\mu}_I$	Nuclear spin magnetic moment vector	$\mathrm{J\,T^{-1}}$
$\boldsymbol{\mu}_L$	Electron orbital magnetic moment vector	$\mathrm{J\,T^{-1}}$
$\boldsymbol{\mu}_S$	Electron spin magnetic moment vector	$\mathrm{J\,T^{-1}}$
$\boldsymbol{\mu}_\mathrm{e}$	Electron spin magnetic moment vector	$\mathrm{J\,T^{-1}}$

Equipment

Agilent B1500A Parameter analyzer.

Drusch RMN2 NMR magnetometer.

EA-PS 3032-10B Power supply.

FEI NOVA200 Focused ion beam.

FEI Titan^3 G2 60-300 Transmission electron microscope.

Fiscione 1040 NanoMill Ion mill.

HP 8348A Microwave amplifier.

HP 8672A Synthesizer.

Jäger ADwin Pro II Eight channel ADC-DAC.

Keithley 2636A Sourcemeter.

Stanford Research SR570 Current amplifier.

Stanford Research SR830 Lock-in amplifier.

TTi QPX1200 Power supply.

Varian E9 EPR spectrometer.